INTELLIGENT DETECTION OF BOLT LOOSENESS USING STRUCTURAL HEALTH MONITORING METHODS AND PERCUSSION APPROACH

by
Furui Wang

A Dissertation submitted to the Department of Mechanical Engineering,
Cullen College of Engineering
in partial fulfillment of the requirements for the degree of

DOCTOR OF PHILOSOPHY

in Mechanical Engineering

Chair of Committee: Dr. Gangbing Song

Committee Member: Dr. Franchek Matthew

Committee Member: Dr. Karolos Grigoriadis

Committee Member: Dr. Zheng Chen

Committee Member: Dr. Yi-Lung Mo

University of Houston
December 2020

DEDICATION/EPIGRAPH

To my parents, who always give me unlimited support.

ACKNOWLEDGMENTS

First, I would like to appreciate my advisor, Dr. Gangbing Song, for his support, guidance, and help during my Ph.D. program. Using his academic attitude and insight, Dr. Song sets a good example for me and helps me to achieve success in my academic career. Overall, I am unable to obtain the doctorate without Dr. Song's direction.

Then, I would like to express my gratitude to Dr. Franchek Matthew, Dr. Karolos Grigoriadis, Dr. Zheng Chen, and Dr. Yi-Lung Mo, for their encouragement and suggestions in the past three years. Additionally, their courses improve my knowledge reserve and academic competence effectively.

All my colleagues in Smart Materials and Structures Laboratory deserve my appreciation, particularly Dr. Siu Chun Michael Ho. His patient instruction improves my English and writing skills, thus enabling the successful accomplishment of this dissertation. Moreover, Dr. Ho's kindness and enthusiasm are important for me to learn.

Furthermore, I would like to thank the China Scholarship Council (CSC, Grant No. 201706060203). With this financial support, I can concentrate on my Ph.D. program without worrying about livelihood.

Finally, I would like to dedicate all my achievements to my parents. They always have no reservation to support me in overcoming countless difficulties during the challenging period of my life.

ABSTRACT

Bolted joints have been widely used to connect different components across multiple engineering fields, while the bolt looseness detection is an urgent issue to be solved. Recently, several piezo-enabled structural health monitoring (SHM) methods have been utilized to detect bolt looseness, including the active sensing method, electromechanical impedance (EMI) method, and the vibro-acoustic modulation (VAM) method. However, current approaches mostly focus on single-bolt looseness detection, and there is still a lack theoretical investigation to explore the principle of these methods.

In this dissertation, several in-depth studies to advance the development of research in the bolt looseness detection are presented. First, a numerical model, a semi-analytical model, and an analytical model of the active sensing method for single-bolt looseness detection is proposed. Then, several new entropy-based indices are developed to replace the current index, i.e., signal energy. Via these entropy-based indices and machine learning (ML) technique, the detection of multi-bolt looseness is achieved for the first time. Second, a model to describe the relationship between bolt preload and EMI signal is theoretically developed, providing a better understanding of the EMI method. Third, in terms of the VAM method, swept sine waves as inputs are employed to improve practicability, and a new entropy-based index is developed to enable the VAM method to detect multi-bolt looseness.

Moreover, considering that the above methods depend on permanent contact between transducers and structures, a new percussion-based approach is proposed. By tapping the bolted joint and analyzing the percussion-induced sound signals, the bolt

looseness can be detected without contact-type sensors. First, an analytical model to research the mechanism of the percussion-based approach for bolt looseness detection is proposed. Then, by using deep learning (DL) based techniques to process and classify the percussion-induced sound signals under different bolt preloads, two practical percussion-based approaches to detect bolt looseness detection were developed.

In summary, several in-depth investigations of SHM methods and a new percussion-based approach for bolt looseness detection have been conducted in this dissertation. It is believed that these methods have great potential for future industrial applications.

TABLE OF CONTENTS

LIST OF TABLES

LIST OF FIGURES

CHAPTER 1. INTRODUCTION

1.1 Motivation and objectives

Across multiple fields of engineering (e.g., mechanical engineering and civil engineering), the bolted connection that is a type of prevailing fastener, has been widely used to hold different components together. Compared to its counterparts such as the welding joint and pin connection, the bolted connection is preferred due to its low-cost and ease-in-reuse (i.e., implementation of screwing off and assembling). However, the bolted connection is prone to decrease of even loss of preload due to several issues (e.g., improper installation, mechanical vibration, and chemical corrosion) as the service time increases, which may lead to severe catastrophes. For instance, since bolts that held stretcher bars were loose, the West Anglia Great Northern northbound train derailed outside the Potters Bar station. On July 10, 2006, the Big Dig ceiling collapse occurred in Boston's Font Point Channel, killing one person. The accident investigation indicated that several anchor bolts suffered creep failure and looseness and thus led to the collapse of ceiling structures. On August 20, 2011, insufficient torque of screws allowed a line replacement unit (LRU) to vibrate and damage during flight, thus inducing a Global Hawk (Northrop Grumman EQ-4) crash in Afghanistan. On August 2012, a blast happened at the Amuay refinery in Venezuela, and Rafael Ramirez, who was then Venezuela's Minister of Energy, claimed that the explosion was caused by bolt-loosening-induced gas leakage. A Vestas wind turbine collapsed in Sweden on December 24, 2015, and the survey report stated that fatigue of bolted joints in the first flange of the tower structure was to blame. Notably, the looseness of pre-tension is the reason for the bolt fatigue. Therefore, to avoid the personal injury and property loss caused by these catastrophes, it is needed to develop promising methods to detect bolt looseness with satisfactory performance.

Previous investigations [1, 2] have demonstrated that the bolt looseness is mainly affected by three issues: plastic deformation at the thread, creep/stress relaxation, and slip between the contact surfaces. In other words, a bolted joint will suffer a complex and time-dependent looseness procedure, rather than an immediate loosening. First, creep/stress relaxation will occur as the service time increases, and plastic deformation will happen at the thread due to external influences such as vibration. Subsequently, these two issues (i.e., plastic deformation and creep/stress relaxation) can deteriorate the bolt preload slightly, thus reducing the friction force at the contact interface. Once the friction force is less than a certain value, there will be two types of relative motions that result in complete looseness, including (1) motion between nut and bolt, and (2) motion between two contact surfaces. Generally, current nondestructive testing (NDT) techniques may be incapable of achieving continuous surveillance of the bolted connection. Therefore, the objective of this dissertation is to employ several structural health monitoring (SHM) methods and the percussion-based approach to detect bolt looseness effectively and to improve the potential for real industrial applications.

1.2 Organization and contributions

The following shows the brief organization of the dissertation with an emphasis on its technical contributions:

Chapter 2 provides a brief introduction of SHM methods, and a detailed review of state-of-the-art techniques for bolt looseness detection is performed. This literature review reveals the current research trend and find several ignored issues, which are essential to be solved for future study of bolt looseness detection.

Chapter 3 focuses on the active sensing method, which employs a pair of Lead Zirconate Titanite (PZT) transducers that are bonded on the surface of the bolted joint to emit and receive stress wave signals. Then the looseness can be monitored by analyzing the change of received signals. The main contribution of this chapter is the development of a quantitative relationship (including numerical, semi-analytical, and analytical modeling, respectively) between the bolt preload and the stress wave signal by using the fractal contact theory. This relationship reveals a better understanding of the working mechanism of the active sensing method.

Chapter 4 intends to solve another problem, i.e., the current active sensing method only depends on signal energy to estimate the integrity of the bolted connection, which is unreliable in some cases. Thus, the concept of entropy to develop several new entropy-based indices for the active sensing method is creatively introduced to enhance the performance significantly. Particularly, the entropy-based indices achieve multi-bolt looseness detection with good performance, which is another main contribution of this chapter.

Chapter 5 researches the piezo-enabled electromechanical impedance (EMI) method, which is a popular approach to bolt looseness detection. However, most of the current investigations only employ the EMI method to detect bolt looseness experimentally without any theoretical analyses. Therefore, the main contribution of this chapter is the development of an analytical model to describe the relationship between bolt preload and EMI method. Overall, bolt looseness will cause stiffness degradation of connection, thus inducing the frequency shift of EMI signals. In other words, the principle of the EMI method for bolt looseness detection is that the EMI signal can characterize the change of structural stiffness. Notably, based on the fractal contact theory, the roughness of the contact interface is taken into consideration in this chapter, which improves the accuracy of the modeling.

To overcome the deficiency of the active sensing method and the EMI method for bolt looseness detection, the vibro-acoustic modulation (VAM) method has been utilized recently. Generally, the VAM method employs two types of input (a low-frequency vibration and a high-frequency ultrasonic wave) to excite the bolted connection, and the looseness status can be estimated by quantifying the sideband of received signals. However, the previous investigation has demonstrated that the performance of the VAM method depends on the prudent selection of the frequency of inputs significantly. It is worth noting that this demand is always impractical in real industrial applications. Thus, Chapter 6 presents a new VAM method that applies swept sine waves for both low-frequency and high-frequency inputs, which is the main contribution. Via this implementation, the practicability of the VAM method is dramatically improved, and several new entropy-based indices are proposed to replace the sideband, which is another main contribution. Finally, the newly proposed VAM method is experimentally demonstrated to detect multi-bolt looseness.

It is worth noting that the above three techniques all depend on permanent contact between transducers and bolted connections. Therefore, in Chapter 7, the main contribution is that a new percussion-based approach is developed to detect bolt looseness without contact-type sensors. Overall, the percussion approach means that the detection of bolt looseness can be realized by analyzing the percussion-induced sound signals. First, an analytical model is developed to research the influence of percussion (i.e., tapping) on sound signals under different bolt preload. Then, the Mel-frequency cepstrum coefficients (MFCC) and DL techniques are used to extract features from sound signals and achieve the bolt looseness identification. Particularly, the percussion is implemented automatically based on a robotic arm, which can improve the practical potential for future industrial applications. Finally, another percussion-based approach is developed, and no hand-crafted features (e.g., MFCC) are needed. Combining the concept of the convolutional neural network (CNN) and memory-augmented neural network (MANN) results in a new DL-based classifier, which is called one-dimensional memory-augmented convolutional neural network (1D-MACNN). Via this 1D-MACNN, the feature extraction and classification of the percussion-induced sound signals can be implemented to achieve the detection of bolt looseness.

Finally, Chapter 8 concludes the whole dissertation. Furthermore, some recommendations for future work are provided to guide future research.

CHAPTER 2. STRUCTURAL HEALTH MONITORING METHODS AND THEIR APPLICATION ON BOLT LOOSENESS DETECTION

2.1 Introduction of structural health monitoring

As we know, modern societies heavily depend on multiple mechanical and civil systems, including aircraft, rotating machinery, bridges, buildings, and offshore oil platforms, etc. However, in light of inevitable aging and degradation resulting from working surroundings, these structures are nearing the end of their design lifetime. Considering the difficulties in replacing the infrastructures mentioned above economically, there is an urgent need to develop various damage detection methods to ensure the safe operation when the design service life is extended. Additionally, current circumstances such as clusters of earthquakes and unpredicted blast loadings demand us to give a quick condition screening in newly built systems at the earliest time. In other words, we should provide real-time diagnosis of structural performance and prevent possible structural failures. Recently, the common damage detection methods consist of the nondestructive test and evaluation (NDT&E) [3], the health and usage monitoring system (HUMS) [4], the statistical process control (SPC) [5], the damage prognosis (DP) [6], and the condition monitoring (CM) [7], etc.

Among the above methods, SHM is the most popular technique. The term SHM generally refers to damage identification and service life forecast across multiple structures in aerospace, civil and mechanical engineering infrastructures. By knowing the real-time structural integrity and correspondingly changing the work organization of maintenance services, the SHM can allow maintenance teams to use the structure and avoid catastrophic failures optimally. Additionally, a lot of handling and transportation operations take place during the intermediate phase between the end of the manufacturing process and the beginning of the functioning period, which is called the pre-usage period. These uncertainty issues may occur and threaten structural reliability. Thus, the development of SHM can further improve the structural design and operational procedure of the structure from a broader systematical perspective, which seems to be a strong motivation for SHM. For instance, aerospace companies are investigating SHM to detect damage such as control surfaces hidden by heat shields, which has life-safe significance. Benefited from the constant maintenance costs and reliability, the SHM has another strong motivation, namely, economic reason. As an example, the semiconductor manufacturer adopts SHM to avoid unpremeditated downtime that costs millions of dollars per hour by minimizing redundant machinery.

Since the ends of the 1980s, the concept of smart materials and structures (SMS) has attracted more and more attention in academia and industry, particularly in the fields of aerospace and civil engineering. Starting from the use of the homogeneous materials supplied by their natural properties, SMS develops to multi-materials (e.g., composite materials) types allowing to create structures with specified purposes, including shape control, vibrations control, and health control. Recently, the SMS has been integrated with SHM systems to achieve three functionalities: (1) fabricating sensors and actuators based on new sensitive materials, (2) miniaturizing and embedding sensors and actuators into the host structures without degradation, (3) conceiving data reduction and diagnostic index for SHM. It is worth noting that sensors, which can be embedded into the components during the manufacturing process, denote an essential topic in SHM. By applying sensors to detect a range of physical parameters including refractive index, visco-elastic properties, and conductivity, etc., several techniques allow us to achieve on-line monitoring, such as electromechanical impedance (EMI) method [8], acousto-ultrasonics approach [9], and optical technology (i.e., based on fiber-optic sensors [10]). Furthermore, such different sensors can be mixed to realize a multi-detection [11], which is a fascinating topic.

Generally, SHM has two functions: diagnosis and prognosis (i.e., the evolution of damage and residual lifetime prediction), as described in Fig. 2-1. First, several sensors with the same type are applied to monitor corresponding physical phenomena related to the damage closely and generate signals that will be sent to a storage sub-system. Subsequently, signals from different kinds of sensors that can be multiplexed as a network are merged into a monitoring sub-system (e.g., computer) to perform a diagnosis. As the service life of various structures increases, a determination of the state of the materials, parts, and full assembly constituting the whole structures is necessary to ensure the structural status remains in a specified domain according to design requirements. The above-mentioned periodically measurements of physical phenomena help to extract the damage-sensitive features, and the health status can be determined according to statistical analysis. Furthermore, it is possible to achieve the usage monitoring function by detecting environmental conditions based on other groups of sensors. Thanks to the long timespan of monitoring, the full history database of the structure can be obtained, in parallel with the usage monitoring method to provide a prognosis (i.e., residual life). At last, the structural health management, such as repair and maintenance operations can be developed accordingly. Partially, the SHM may be called as an improved approach of NDT&E, if just considering its first function (namely, the diagnosis). However, the SHM is much more since it involves several aspects, including the integration of sensors based on smart materials, data acquisition and transmission, and advanced algorithms for signal processing.

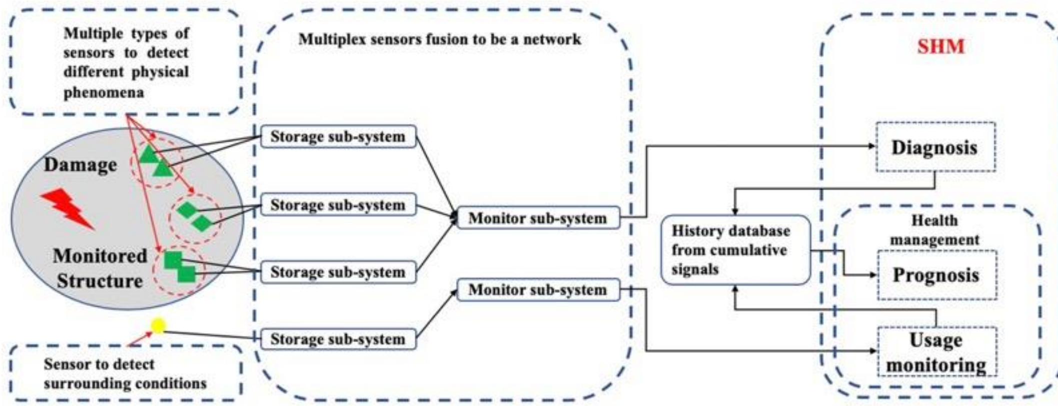

Fig. 2-1 Principle of an SHM system

Analogous to NDT&E as mentioned above, the SHM can be active or passive, as shown in Fig. 2-2. Equipped with sensors, the structural state and its interaction with the surrounding environment can be evolved with corresponding physical parameters. The monitoring method that just depends on sensors can be called as the "passive SHM"; for instance, the acoustic emission techniques [12]. On the contrary, if there is the use of actuators to perturb the structures and then monitor the response through sensors, the action is regarded as the "active SHM" in such a case, such as the active sensing method [13]. In this sort of situation, the actuator (namely, piezoelectric patch) generates ultrasonic waves, and another piezoelectric patch worked as the sensor is used to receive signals as a possible damage index allowing detection. Differing from the traditional NDT&E that excites the structure with an external device, the same transducer can work as both actuator and sensor (e.g., EMI method), which allows flexible and simple monitoring system.

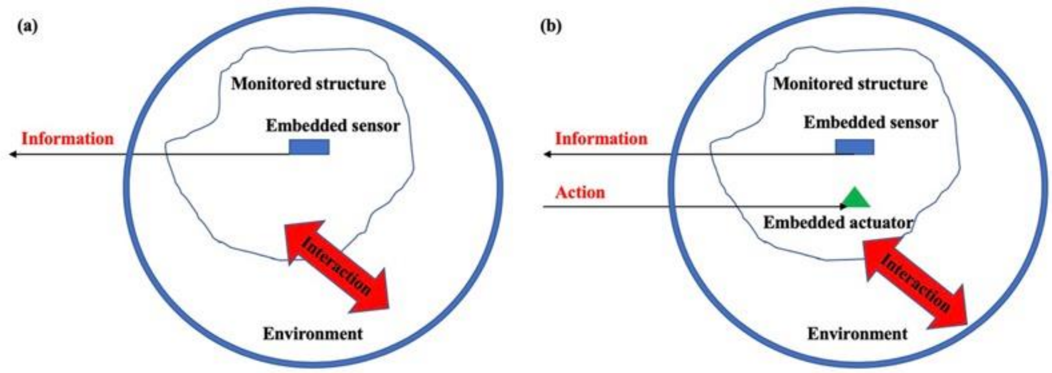

Fig. 2-2 (a) Passive SHM and (b) active SHM

In conclusion, the safety of the aging structures across multiple industries is a significant issue, and the SHM methods, which is an interesting tool, can provide opportunities to guide structural design and prolong service life through damage detection. On the other hand, to reduce the repair and maintenances cost, it is essentially desirable to answer the health state of the structure in a timely manner. Generally, the damage assessment can be divided into four levels, as given in Fig. 2-3. The level I (detection) just tells us the message that if the damage exists in the monitored structures, while the level II (localization) can describe the position of the damage. At level III (extent of damage), the structural damage can be quantified (i.e., damage size, mass loss, and stiffness degradation, etc.), which requires a parametric model to extract characteristics features. Finally, as the most sophisticated part, the level IV (prognosis of remaining life) can give the evolution of damage and thus predict the residual work life of the structures through the combination of the global structural model and local fracture pattern. In the past decades, many researchers have contributed to the development of SHM by coming up with various methods, and these methods will be introduced in the following subchapters.

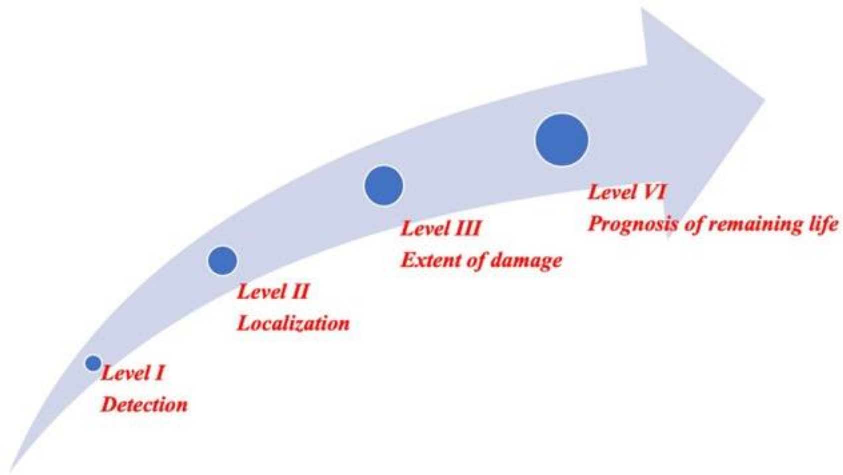

Fig. 2-3 Four levels in SHM

2.2 A review of methods for bolt looseness detection

As discussed in Chapter 1, there is a need to ensure sufficient bolt preload and detect bolt looseness since the inadequate axial force of bolted connections can induce structural damage [14]. Traditional methods for measuring preload and detecting bolt looseness include direct tension indicator [15], strain gauges [16], and torque control [17]. Generally, the direct tension indicator employs a specific washer with protruding features, and the gap between features and bolt (or nut) can be used to indicate bolt axial force. Though the direct tension indicator is straightforward to use, it should be noticed that it cannot detect bolt loosening and depends on specifically designed washers, which causes an increase in costs. By designing washer-like strain gauges, one can measure the preload of bolted joints with acceptable accuracy, while these washers are comparatively expensive and impractical for some cases. On the other hand, one can directly bond strain gauges on bolted joints to reduce costs, but the accuracy will be deteriorated. This is because the surface strain is marginal (i.e., slightly change) when the bolt is loose. In real industries, the most popular approach to detect bolt looseness is the torque wrench. By using torque-meters, operators can measure the torque of bolt connections directly with low-cost; however, a previous investigation [17] has demonstrated that only 10%-15% of the applied torque is used to provide axial preload (remaining is wasted due to friction). In other words, accurate bolt looseness detection via the torque control technique cannot be ensured. To circumvent deficiencies of the above methods, researchers have utilized several SHM methods to achieve better performance of bolt looseness detection. Generally, in terms of detection of bolt loosening, SHM methods employ various physical parameters to indicate changes of axial preload, and more details are introduced in the following subsections.

2.2.1 EMI method

The EMI method is one of the most popular ways to detect bolt looseness, and it mainly depends on an impedance analyzer and a PZT transducer. By bonding a PZT transducer on the surface of structures and applying an electric voltage difference, one can estimate the electromechanical response of via an impedance analyzer. The principle behind this method is that the impedance of a system is stable with the same condition, and various structural damages (e.g., looseness, crack, and corrosion) can affect dynamic features, which can be reflected by impedance values. Therefore, several investigations [18, 19, 20, 21, 22, 23, 24] have been carried out to detect bolt looseness in multiple structures. Moreover, the EMI method has been integrated with ultrasonic waves [25, 26] to detect bolt looseness with better performance, and a wireless-based EMI method [27] has attracted much attention. The main advantage of the EMI method is a high sensitivity, and it is capable of online monitoring of bolt looseness. However, the EMI method is suitable for local damage identification (i.e., it required a large number of sensors for multi-bolt connections), and it is significantly affected by ambient temperatures [28]. Moreover, some theoretical analyses of the EMI method have been performed [19, 29, 30, 31] (including one-dimensional (1D), two-dimensional (2D), and three-dimensional (3D) models), while no EMI-based modeling of bolt looseness detection has been developed. The author will bridge this gap in Chapter 5 of this dissertation.

2.2.2 Vibration-based method

The vibration-based method is another technique that can be used to detect bolt looseness. It is well known that the bolt looseness can induce stiffness deterioration of the whole structures, and thus bolt looseness can be monitored by analyzing characteristics of vibration signals in the time domain, frequency domain, and time-frequency domain [32, 33, 34, 35, 36, 37, 38, 39, 40, 41]. Generally, to excite structures with different sizes and conditions, one can use hammers or vibrators, and the vibration signals can be captured via piezoelectric accelerometers or laser vibrometers. Moreover, due to the excitation ways (hammers or vibrators), the vibration-based method is unsuitable for online monitoring. On the other hand, some scholars have researched the principle [42, 43] and efficiency [44, 45] of the vibration-based method. Compared to the EMI method, the vibration-based method is more cost-efficient and easier to implement. However, the vibration-based method belongs to a global damage detection method, which is insensitive to local damage such as bolt looseness.

2.2.3 Ultrasonic-based method

The ultrasonic-based method, which attracts extensive favorability across multiple industries, has been used to detect bolt looseness by employing linear phenomena (energy dissipation and reflection) and nonlinear phenomena (scattering and modulation) of ultrasound waves as indices. Generally, it can be divided into three categories: the active sensing method, the acoustoelastic effect-based approach, and the harmonic-based method.

(1) The active sensing method calculates the energy dissipation of ultrasonic waves during the propagation across bolted interface to estimate the bolt looseness. Previous investigations [46, 47, 48] have experimentally demonstrated that more signal energy will dissipate under lower preload of the bolted connection. Overall, the active sensing method is low-cost and can be used to implement online monitoring of bolt looseness. However, several issues are imperative to be solved: first, an analytical model of the active sensing method should be developed to enable us to have a better understanding of the mechanism; second, the current active sensing method encounters the problem of saturation. In other words, the signal energy is influenced by bolt preload slightly when the applied torque is larger than a certain value; finally, the active sensing method is only utilized to detect single-bolt looseness recently. To overcome the above three issues, the author conducts several innovative investigations correspondingly in Chapters 3 and 4.

(2) The velocity and frequency of ultrasonic waves are directly affected by preload when the waves propagate across the bolt bar [49, 50, 51], which is the principle of the acoustoelastic effect-based method. In other words, one can detect bolt looseness via travel time and mechanical resonance frequency. To detect bolt looseness by measuring travel time, one always employs the time-of-flight (TOF) method [52, 53, 54]: an ultrasonic transducer is placed on one side of the bolt to emit pulse-echo

waves, and the flight time can be measured. Then, one can calculate the elongation of the bolt bar via the velocity of ultrasonic waves to detect bolt preload, since elongation is approximately proportional to preload. The TOF method is easy-to-understand, and its operation is simple. However, it requires specific equipment that has a very high sampling rate, thus resulting in high cost. Additionally, the accuracy of the TOF method is not high since the only linear property is considered. On the other hand, researchers [55] have claimed that the resonance frequency of ultrasonic waves is a function of wave velocity and bolt length, and these two issues are affected by preload. Therefore, one can detect bolt looseness by monitoring the changes in the resonance frequency of ultrasonic waves.

(3) Different from the active sensing method and acoustoelastic effect-based method, the harmonics-based method depends on nonlinear phenomena of ultrasonic waves. Overall, there are two main harmonics-based methods, including the second-harmonic method [56, 57, 58, 59, 60] and the vibro-acoustic modulation (VAM) method [61]. For the second-harmonic method, only single input (ultrasound) is used, while two inputs (both vibration and ultrasound) are employed in the VAM method. When an ultrasonic wave hits the loose bolt, a second-order harmonic will appear in the frequency spectrum of the signal, which can be explained via the theory of contact acoustic nonlinearity (CAN). On the other hand, for the VAM method, the bolt looseness will cause modulation of a combination signal of vibration and ultrasound. Particularly, this modulation can be represented in the frequency area (i.e., sideband), and an index that quantifies the sideband can be used to estimate the bolt looseness. Though the VAM method has more accuracy than

other ultrasonic-based methods, several issues need to be addressed. First, both low-frequency vibration and high-frequency ultrasound are single-frequency inputs, and careful selection of frequency values is required to ensure the performance of the VAM method. Moreover, the current index for sideband is unsuitable for multi-bolt looseness. In Chapter 6, the author will develop several new concepts to solve these two problems.

2.2.4 Other methods

In addition to the above three kinds of methods, several other approaches have been proposed to detect bolt looseness, including the acoustic moment method [62], vision-based method [63], and radio wave-based method [64]. However, these methods are still in the primary stage of research, and they need more investigations in future work.

CHAPTER 3. BOLT LOOSENESS DETECTION VIA ACTIVE SENSING METHOD

3.1 Introduction of active sensing method

As shown in Fig. 3-1, the machined surface is rough (i.e., surface asperity) if observed from a micro perspective. Therefore, the interface of the bolted connection is not ideally contacted. In other words, the true contact area of the bolted interface is smaller than the nominal contact area since only tips of surface asperities constitute the actual contact. Notably, the previous investigation [65] has demonstrated that the contact area is proportional to the square root of contact pressure, and larger bolt preload will increase the true contact area, thus reducing energy dissipation at the interface. That is to say, one can estimate the change of preload by quantifying the energy dissipation of signals when they propagate across the interface.

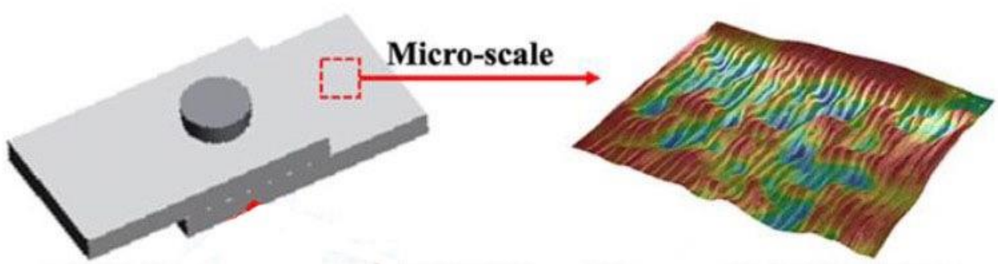

Fig. 3-1 Illustration of the machined surface

To obtain the above energy dissipation, one always employs the active sensing method that bonds a pair of PZT transducers on the surface of the bolted connection (as depicted in Fig. 3-2). Specifically, PZT 1 that works as an actuator can generate ultrasonic waves, and PZT 2 can be used to receive these waves that propagate across the bolted interface. Subsequently, by calculating the energy difference of signals that are emitted by PZT 1 and captured by PZT 2, one can obtain the energy dissipation. Since the energy dissipation is proportional to the true contact area [66], one can develop the relationship between bolt preload and the energy dissipation to achieve bolt looseness detection. Overall, larger bolt preload (torque) will lead to a larger true contact area, thus generating less energy dissipation. In other words, PZT 2 will receive more energy.

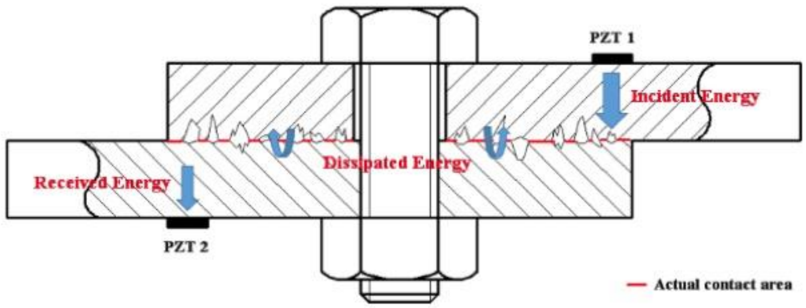

Fig. 3-2 Schematic diagram of the active sensing method

Though the principle of the active sensing method is straightforward, there is still no quantitative modeling so far. Therefore, in the following subchapter, the author will construct several quantitative models (including numerical model, semi-analytical model, and analytical model) based on the fractal contact theory to enable us to have a better understanding of the active sensing method.

3.2 Introduction of the fractal contact theory

The introduction of the active sensing method reveals that the core issue of modeling the active sensing method is how to quantify the relationship between the bolt preload and the true contact area. Traditional methods that can be used to address this issue mainly depend on statistics of asperities and classical contact mechanics. For instance, the Greenwood-Williamson (G-W) model [67] of the interface, developed by Greenwood and Williamson in 1966, was carried out through elastic contact modeling of the rough surface by assuming that the tips of asperities were spherical and their height conformed to the Gaussian distribution. Based on the G-W model, several researchers (Whitehouse and Archard [68], Chang et al. [69], and Zhao et al. [70]) have developed many different modeling considering the shape and distribution of asperities to investigate the contact of the rough surface. In Chang's research [69], which is called the CEB modeling, the deformation of the sphere (i.e., asperity) was still regarded as the elastic Hertz contact, and volume conservation was assumed. Also, other researchers [71, 72, 73] have improved the CEB modeling by mathematical methods. However, the interactions between the asperities were ignored in their studies. Thus, Jeng and Peng [74] investigated the effects of asperity interactions, and the significant influence of asperity interactions was found. Additionally, the finite element analysis (FEA) has been widely used to study the contact problem. Kucharski et al. [75] and Liu et al. [76] proposed FEA models to study the elastic-plastic contacts of rough surfaces, respectively. Using the FEA, Kogut and Etsion [77, 78] analyzed the elastic-plastic adhesion problem of spherical and the elastic-plastic contact problem of a sphere and a rigid flat. In addition, the elastic-plastic adhesion contact of non-Gaussian rough surfaces was investigated by Sahoo and Ali [79].

However, the above-mentioned investigations are all based on statistics, which are subject to the resolution ratio of measuring instrument and sampling length. In other words, the computed results obtained from these modeling show uncertainties. Overall, the fractal contact theory is the combination of the fractal theory and classical contact mechanics. Fractal is a ubiquitous phenomenon in nature, which means that similar patterns will appear with smaller scales (i.e., self-similarity) [80]. In other words, the profile of machined surfaces (e.g., bolted interface) can be globally described via its fractal property, which enables the certainty and uniqueness of the result. In 1991, based on the Weierstrass-Mandelbrot (W-M) function [81, 82], Majumdar and Bhushan [83, 84] developed the M-B elastic-plastic contact model, which opened the door to research the fractal contact theory. Then, in 1994, Wang and Komvopoulos [85, 86] improved the M-B elastic-plastic contact model and lead the research for the next two decades [87, 88, 89, 90, 91, 92, 93, 94, 95].

In this Chapter, inspired by the above investigation, the author will apply the fractal contact theory to describe the distribution of surface asperities and their deformation under axial pressure (bolt preload).

3.3 Numerical modeling of the active sensing method

Based on the fractal contact theory, the author first constructs a numerical model that takes the interfacial roughness into consideration to simulate the active sensing method for bolt looseness detection. The W-M function [81, 82] helps to generate a two-dimensional (2D) surface profile $z(x)$ with fractal characteristics as,

$$z(x) = G^{(D-1)} \sum_{n=n_{\min}}^{\infty} \frac{\cos 2\pi\gamma^n x}{\gamma^{(2-D)n}} \quad (1 < D < 2), \tag{3-1}$$

where γ is always set to 1.5, and it can be utilized to measure the phase differences between different modes of the fractal. Moreover, D and G are the fractal dimension and fractal roughness parameters of the surface profile, respectively. Then, a new truncated W-M function was proposed by Komvopoulos and Yan [96] as

$$z(x) = L\left(\frac{G}{L}\right)^{(D-1)} \sum_{n=0}^{n_{\max}} \frac{\cos\left(2\pi\gamma^n x/L\right)}{\gamma^{(2-D)n}} \quad (1 < D < 2), \tag{3-2}$$

where L_0 is the smallest characteristic length, $n_{max} \approx \ln(L/L_0)/\ln\gamma$, and L is the surface profiler's sampling length.

However, the above function can only be applied to produce 2D surface topography arbitrarily, and Yan and Komvopoulos [97] extended the above truncated W-M function from 2D to 3D as

$$z(x,y) = L\left(\frac{G}{L}\right)^{(D-2)}\left(\frac{\ln\gamma}{M}\right)^{1/2}\sum_{m=1}^{M}\sum_{n=0}^{n_{max}}\gamma^{(D-3)n}\psi$$

$$\psi = \left\{\cos\phi_{m,n} - \cos\left[\frac{2\pi\gamma^n\left(x^2+y^2\right)^{1/2}}{L}\cos\left(\tan^{-1}\left(\frac{y}{x}\right)-\frac{\pi m}{M}\right)+\phi_{m,n}\right]\right\}, \quad (3\text{-}3)$$

$$(2 < D < 3)$$

where $n_{max} = \mathrm{int}[\ln(L/L_s)/\log\gamma]$ is the upper limit of n, n is the spatial frequency index, L_s denotes the cut-off length, M is the total number of the superposed ridges that construct the surface, and $\phi_{m,n} \in [0, 2\pi]$ is the randomized phase angle. As shown in Fig. 3-3 [98], a sample of the W-M surface can be generated by using MATLAB, and the detailed parameters are D =2.4, G =6.36×10^{-13} m, L =1×10^{-5} m, L_s =5×10^{-9} m, γ =1.5, M =10. Moreover, the generated surface can be imported into the Pro/E to construct its 3D solid modeling, which can be used for numerical analyses.

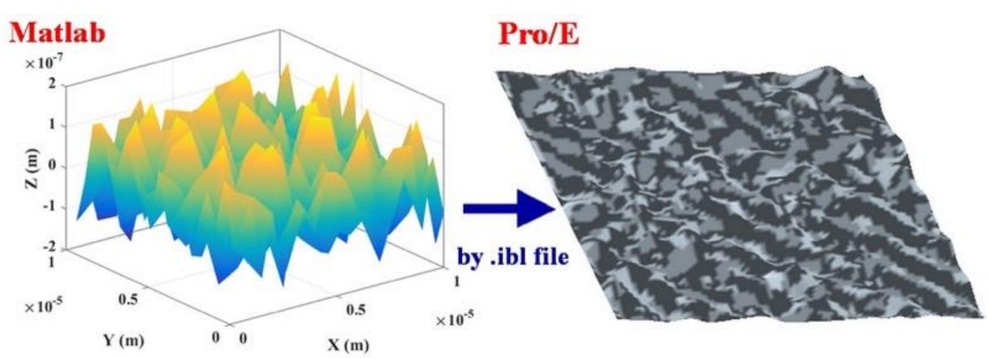

Fig. 3-3 A sample W-M surface and its geometry of 3D solid modeling

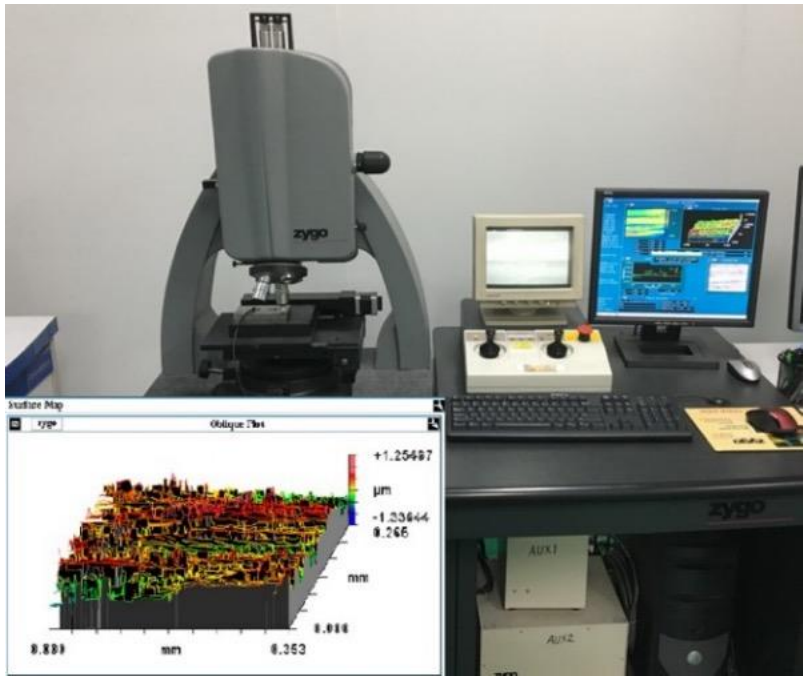

Fig. 3-4 The Zygo surface profiler

Via a 3D surface profiler (Zygo, NewView 5022, USA), which is shown in Fig. 3-4 [98], the fractal roughness G and the fractal dimension D were measured as 2.4 and 6.4×10^{-13}m, respectively. After measuring the G and D, the author generated the rough interface of a bolted connection and the corresponding 3D solid model via the procedure introduced earlier. Then, to mimic the active sensing method, the autor establihsed a finite element model (as depicted in Fig. 3-5 [98]) by using a commercial software Abaqus-CAE 14.0. Overall, the fabricated model consists of two steel plates (size: 100mm×60mm×10mm), a pair of bolt and nut (M12), and two PZT transducers (size: 10mm×10mm×1mm). The elements of C3D8 and C3D8E are assigned to the steel plate/bolt/nut and the PZT patches, respectively. Moreover, the properties of the steel plates, bolt, nut, PZT patches, and the contact characteristics are given in Table 3-1 [98]. Notably, the predefined PZT device in ABAQUS is used to model the mechanical and electrical properties of PZT patches.

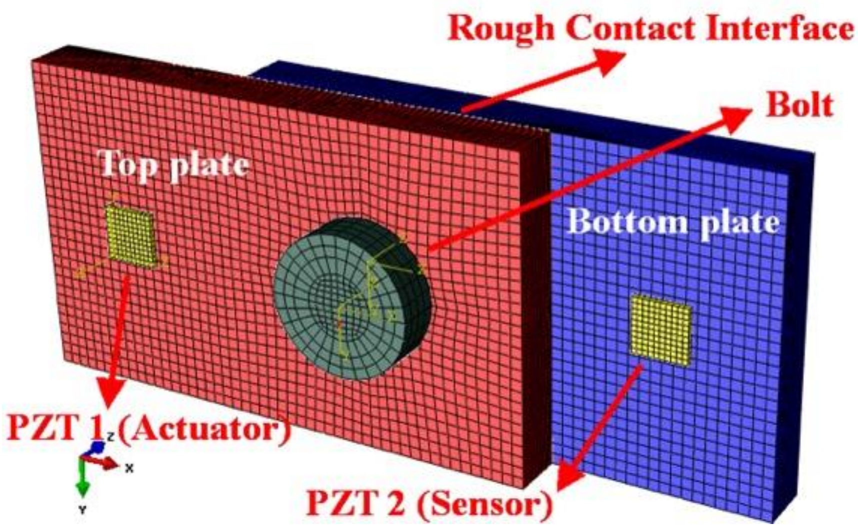

Fig. 3-5 Numerical modeling of bolted joint with two PZT patches

Table 3-1 Material and contact properties

Material	Properties	Value
Steel (bolt/nut/plate)	Young modulus	209 GPa
	Poisson ratio	0.3
	Density	7860 kg m^{-3}
	Yield stress	240 MPa
PZT	Young modulus	46 GPa
	Poisson ratio	7450 kg m^{-3}
	Piezoelectric coefficient $d_{31}, d_{32} / d_{33} / d_{15}$	-186 pC N^{-1}/720 pC N^{-1}/ 660 pC N^{-1}
	Dielectric coefficient $\varepsilon_{11}, \varepsilon_{22} / \varepsilon_{33}$	15.05 nF m^{-1}/13.01 nF m^{-1}
Interface	Coefficient of static friction μ_s	0.3
	Coefficient of static friction μ_k	0.3

Fig. 3-5 shows that two PZT patches are bonded on the surfaces of the bolted connection. Moreover, to mimic the bolt loading procedure and the propagation of ultrasonic waves at the bolted interface, the author will carry out a two-step analysis, including the quasi-static analysis and time-dependent dynamic implicit analysis. In the quasi-static analysis, both normal and tangential contact is taken into consideration by using the coulomb frictional model, which is predefined in the ABAQUS. Then, the total preload of 70 kN is applied to the bolt gradually, with the increments of 10 kN. As depicted in Fig. 3-6 [98], the contact area is not distributed uniformly, which can be attributed to the existence of surface roughness (asperities).

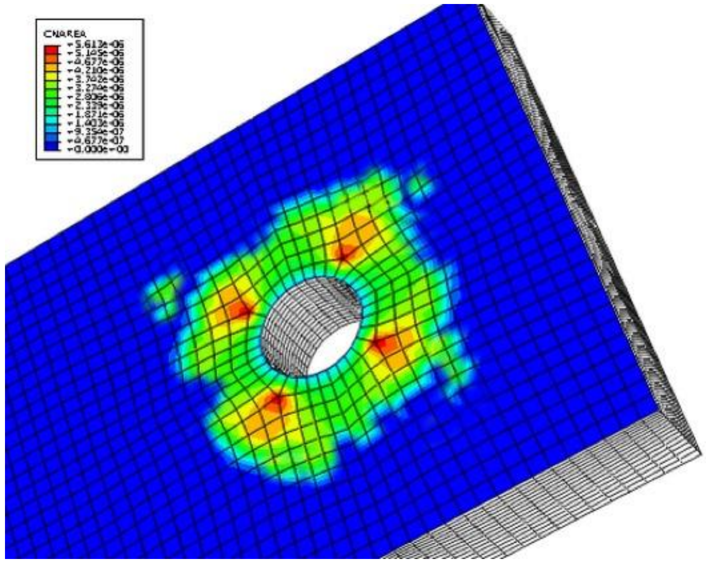

Fig. 3-6 Contact simulation at the bolted interface (preload: 30 kN)

Subsequently, the coupled electro-mechanical model predefined in ABAQUS is used to simulate the active sensing method (the emission, propagation, and reception of ultrasonic waves) in the time-dependent dynamic implicit analysis. The period and step of this dynamic implicit analysis are set to 0.02 second and 1×10^{-6} second, respectively. Notably, the tie constraint in ABAQUS is utilized to satisfy the perfect bonding condition of PZT patches. The mesh is generated by considering the center frequency of the Gaussian pulse and the ultrasonic wave speed. A Gaussian pulse with the kHz center frequency of 100 kHz and amplitude of 10V is used to stimulate the PZT 1, thus emitting ultrasonic waves. Then, PZT 2 can capture these ultrasonic waves after they propagate across the interface.

Then, to verify the effectiveness of the proposed numerical modeling, the author performs an experiment whose setup is shown in Fig. 3-7 [98]. Overall, the experimental apparatus includes the bolted joint, a computer, an NI-DAQ system (NI USB 6366), a torque wrench, and two PZT patches. The size of specimens (bolted joint and PZT patches) and excitation signal (i.e., the Gaussian pulse) are the same as them in the numerical model to ensure consistency. Eight distinctive preloads (from 0 kN to 70 kN with an interval of 10 kN) are applied to the bolted joint via the torque wrench. Each preload corresponds to an output, the ultrasonic wave signal.

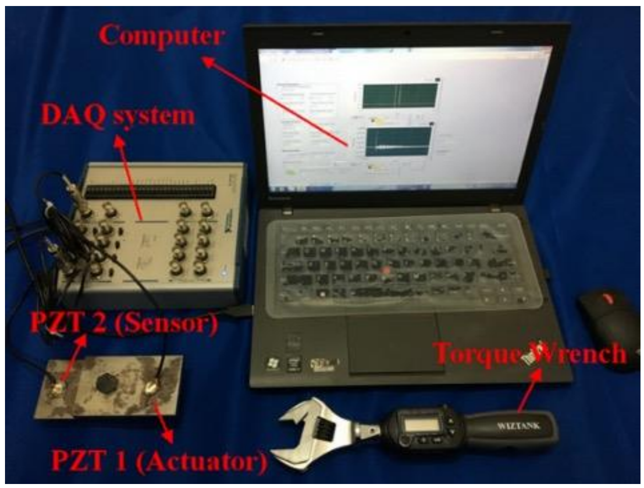

Fig. 3-7 Experimental setup

Finally, the numerical and experimental relationship between signal amplitude (obtained via PZT 2) and the applied preload is illustrated in Fig. 3-8 [98], and the author provides another previous investigation [99] to demonstrate the superiority of the proposed numerical model. It is clear that a larger preload leads to a larger signal amplitude, thus enabling the bolt looseness detection. On the other hand, this tendency is gradually saturated. This phenomenon conforms to a previous investigation [100], which claims that the true contact area is prone to saturation (i.e., plastic deformation) when overlarge torque is applied. Additionally, the proposed model has better performance than the previous investigation results [99].

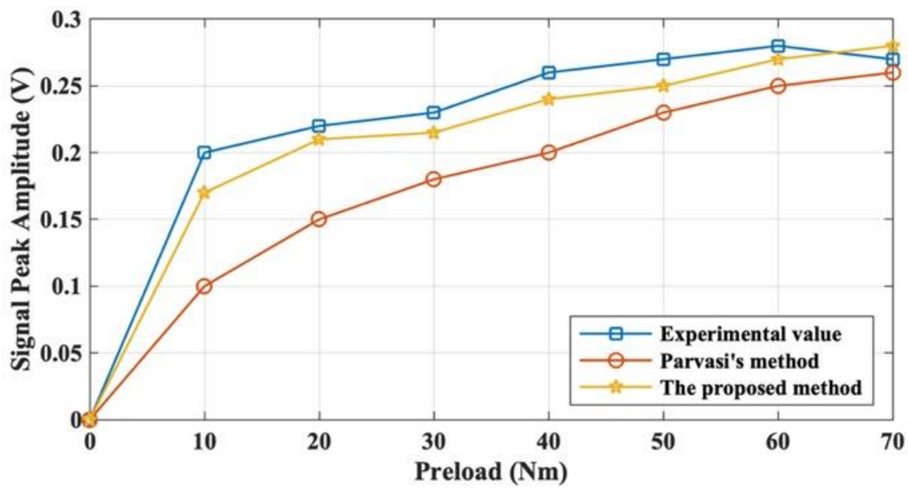

Fig. 3-8 Comparison of numerical and experimental results

3.4 Semi-analytical modeling of the active sensing method

In this subchapter, the author sets up a semi-analytical model of the active sensing method based on the fractal contact theory. The earlier introduction reveals that the core issue of modeling the active sensing method is how to develop the two relationships. One is the relationship between bolt axial preload and the true contact area, and the other one is the relationship between the energy dissipation of ultrasonic waves and the true contact area. Here, “semi-analytical” denotes that the relationship between bolt axial preload and the true contact area is developed via analytical modeling, while the relationship between energy dissipation of ultrasonic waves and the true contact area is obtained by numerical simulation.

It is worth noting that the surface roughness can be considered as a distribution of asperities. That is to say; the true contact area can be calculated by summing the contact deformation of all asperities, whose distribution can be described by the fractal characteristics. On the other hand, the Hertz contact theory [101] indicates that the deformation of asperities can be related to axial preload. Therefore, based on the fractal contact theory, there is excellent potential to analytically establish the relationship between bolt axial preload and the true contact area.

First, based on the previous investigation [78], the deformation of asperities can be divided into four stages (elastic stage, elastic-plastic-I stage, elastic-plastic-II stage, and plastic stage) as

$$\begin{cases} F_e = \frac{4}{3} E^* R^{1/2} \delta^{3/2} & \delta \le \delta_c \\ F_{e-p1} = \frac{2}{3} \times 1.03 K H \pi R \delta_c \left(\frac{\delta}{\delta_c} \right)^{1.425} & \delta_c \le \delta \le 6\delta_c \\ F_{e-p2} = \frac{2}{3} \times 1.40 K H \pi R \delta_c \left(\frac{\delta}{\delta_c} \right)^{1.263} & 6\delta_c \le \delta \le 110\delta_c \\ F_p = 2 H \pi R \delta & \delta \ge 110\delta_c \end{cases}, \tag{3-4}$$

where F_e , F_{e-p1}, F_{e-p2}, and F_p are the normal contact load in elastic deformation stage, two different elastic-plastic deformation stages, and plastic deformation stage, respectively. Moreover, K is coefficient of hardness, δ is the normal deformation of asperity, δ_c is critical deformation degree of asperity, H is the hardness of the material, R is the radius of asperity on the rough surface, E^* is the equivalent elasticity modulus. Then, the above parameters can be computed as

$$\begin{gathered} E^* = \left[\left(1 - \upsilon_1^2\right) / E_1 + \left(1 - \upsilon_2^2\right) / E_2 \right]^{-1} \\ \delta_c = \left(\frac{\pi K H}{2E^*} \right)^2 R \\ H = 2.8\sigma_s \\ K = 0.454 + 0.41\upsilon \end{gathered}, \tag{3-5}$$

where E_1 and E_2 are elasticity modulus of two contact materials, respectively. Moreover, ν_1 and ν_2 are Poisson's ratio of two contact materials, σ_s is the yield strength of the material, υ is the Poisson's ratio of the material.

Subsequently, Wang and Komvopoulos [85] demonstrated that the distribution of the asperities could be expressed as

$$n\left(A'\right)=\frac{D}{2}\psi^{(2-D)/2}A_1'^{D/2}\,A'^{-(D+2)/2}\quad 0<A'\le A_1', \tag{3-6}$$

where A' is the truncated area of asperities, A_1' is the truncated area of the largest asperity. Then, ψ is the domain extension factor [85], which can be computed as

$$\frac{\psi^{(2-D)/2}-\left(1+\psi^{-D/2}\right)^{-(2-D)/D}}{\left(2-D\right)/D}=1\quad \psi>1. \tag{3-7}$$

Moreover, the normal deformation of asperity δ, radius of asperity R, and critical deformation degree of asperity δ_c can be obtained as

$$\begin{gathered}\delta=G^{D-1}A'^{\frac{2-D}{2}}\\ R=\frac{A'^{D/2}}{2\pi G^{D-1}}\\ \frac{\delta}{\delta_c}=\left(\frac{a_c'}{A'}\right)^{D-1}\\ a_c'=G^2\left(\frac{2^{3/2}E^*}{\pi^{1/2}KH}\right)^{2/(D-1)}\end{gathered}\quad. \tag{3-8}$$

Based on the traditional contact mechanics [101], the relationship between the axial load and truncated contact area can be expressed as

$$F=\int_{0}^{110^{1/(1-D)}a_c'}F_p n(A')dA'+\int_{110^{1/(1-D)}a_c'}^{6^{1/(1-D)}a_c'}F_{e-p2}n(A')dA'+\int_{6^{1/(1-D)}a_c'}^{a_c'}F_{e-p1}n(A')dA'+\int_{a_c'}^{A_l'}F_e n(A')dA' \tag{3-9}$$

Substituting eqns. (3-4, 3-5, 3-6, 3-7, 3-8) into eqn. (3-9) achieves the normalized relationship between bolt axial preload F and the true contact area A_r as

$$F^*=5.6g_1(D)\varphi\psi^{\frac{(D-2)^2}{4}}A_r^{*\frac{D}{2}}a_c^{*\frac{2-D}{2}}+g_3(D)\times\frac{0.46g_4(D)\pi K^3\varphi^3}{G^{*2(D-1)}}\psi^{\frac{(D-2)^2}{4}}a_c^{*\frac{D}{2}}A_r^{*\frac{D}{2}}+$$
$$g_2(D)\times\frac{4G^{*(D-1)}}{3(2\pi)^{1/2}}\psi^{\frac{(D-2)^2}{4}}A_r^{*\frac{D}{2}}\left[\left(\frac{2-D}{D}\right)^{\frac{3-2D}{2}}\psi^{\frac{(D-2)(3-2D)}{4}}\times A_r^{*\frac{3-2D}{2}}-a_c^{*\frac{3-2D}{2}}\right]$$
$$1<D<2\,(D\neq1.5),$$
$$F^*=0.7\varphi A_r^{*3/4}\psi^{1/16}a_c^{*1/4}+0.74\left(\frac{1}{2\pi}\right)^{1/2}G^{*1/2}A_r^{*3/4}\psi^{1/16}\ln\frac{\psi^{-1/4}A_r^*}{3a_c^*}+$$
$$0.85\pi K^3 g_4(D)\frac{\varphi^3 A_r^{*3/4}\psi^{1/16}a_c^{*3/4}}{G^*}$$
$$D=1.5 \tag{3-10}$$

where

$$g_1(D)=110^{\frac{2-D}{2(1-D)}}\left(\frac{D}{2-D}\right)^{(2-D)/2}$$
$$g_2(D)=\frac{2^{(3-D)/2}D^{(2-D)/2}(2-D)^{D/2}}{3-2D}$$
$$g_3(D)=D^{\frac{2-D}{2}}2^D(2-D)^{\frac{D}{2}}.$$
$$g_4(D)=\frac{1.03\left(1-6^{\frac{1.425-0.925D}{1-D}}\right)}{1.425-0.925D}+\frac{1.40\left(6^{\frac{1.263-0.763D}{1-D}}-110^{\frac{1.263-0.763D}{1-D}}\right)}{1.263-0.763D}$$
$$F^*=\frac{F}{EA_a}\quad G^*=\frac{G}{\sqrt{A_a}}\quad A_r^*=\frac{A_r}{A_a}\quad a_c^*=\frac{a_c'}{2A_a}\quad \varphi=\frac{\sigma_s}{E^*}$$

On the other hand, the relationship between energy dissipation of ultrasonic waves and the true contact area is obtained via the numerical simulation through the commercial software ABAQUS. Since the materials of bolt and plate are the same (i.e., steel), the bolt in the numerical model is ignored, as shown in Fig. 3-9 [102]. This simplification is acceptable since only the influence of true contact area on energy dissipation (or amplitude) of ultrasonic waves is the concern here. Moreover, this model has better efficiency, since no thread, which can lead to divergence, is considered. Two PZT transducers (size: 10 mm×10 mm×1 mm) are bonded on two steel plates, and the elements of C3D8 and C3D8E are assigned to the steel plate and the PZT patches, respectively. The thickness of the steel plate is 10 mm, and its area is calculated by eqn. (3-10) under different bolt axial preload. All parameters and setup of the contact between steel plates are given in Table 3-1, and the contact between plate and PZT is set to “Tie constraint” in ABAQUS. The time duration of the analysis process (forward and reverse) are set as 0.001 second and 0.0025 second, respectively, and the time step in the numerical simulation is set as 10^{-7} second.

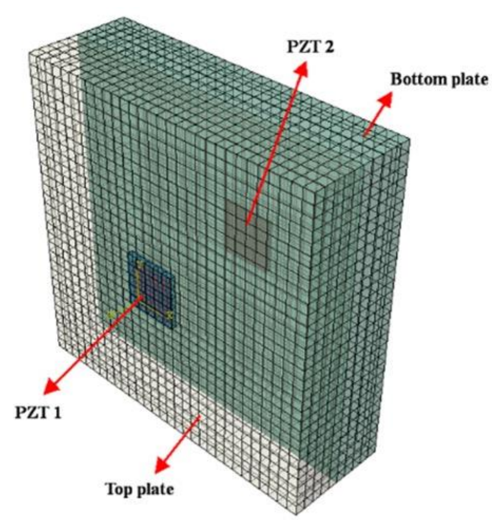

Fig. 3-9 Illustration of the numerical simulation model

To stimulate PZT 1, the author employs a Gaussian pulse (center frequency: 100 kHz, amplitude: 10 V), and the focused signal amplitude, which is obtained via the time-reversal technique, is captured by PZT 1 again. Please note that this is different from the last subchapter (PZT 1 is used to emit waves, and PZT 2 is used to capture waves). The implementation of the time-reversal method [103, 104] is described as follows.

(1) Given the Gaussian input signal $f(t)$, which is emitted at PZT 1, one can obtain the received signal $y(t)$ at PZT 2 as

$$y(t) = f(t) \otimes h(t), \tag{3-11}$$

where $h(t)$ denotes the impulse response function (IRF) of the structures, $\otimes$ is convolution integration.

(2) Then the received signal $y(t)$ is reversed in the time domain as

$$y(-t) = f(-t) \otimes h(-t), \tag{3-12}$$

and transmit it back to PZT 1 (i.e., PZT 2 works as actuator now).

(3) Finally, the focused signal at PZT 1 can be obtained as

$$\begin{aligned} Output^{focused} &= y(-t) \otimes h(-t) \\ &= f(-t) \otimes [h(-t) \otimes h(t)] \end{aligned}. \tag{3-13}$$

Overall, the time-reversal technique helps to improve the performance of the active sensing method. This is because that the time-reversal technology can suppress the energy dissipation caused by scattering and reflection of waves. In other words, one can consider that most of the energy dissipation is caused by bolt looseness, which eliminates the effect of system errors. The result (i.e., the relationship between focused signal amplitude and true contact area) is depicted in Fig. 3-10 [102].

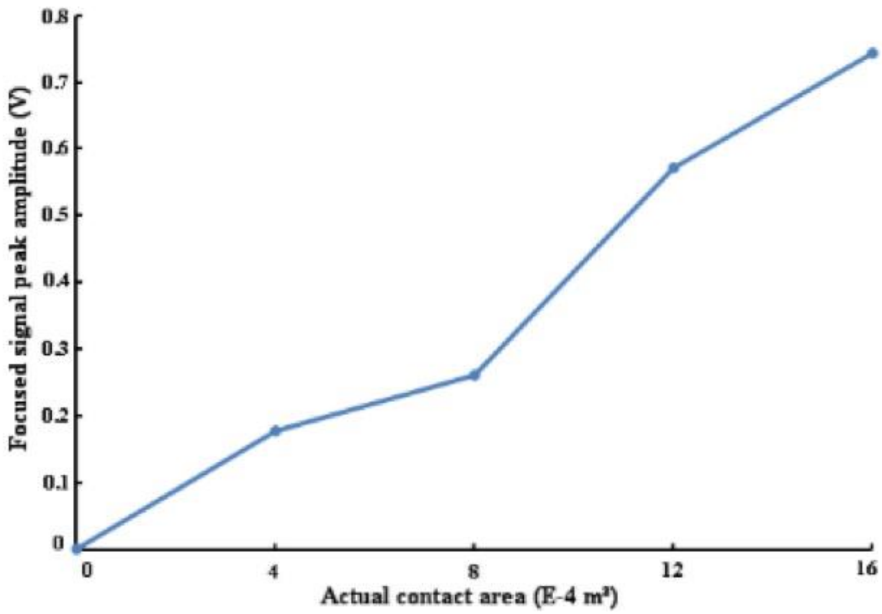

Fig. 3-10 Simulated relationship between focused signal amplitude and true contact area

Additionally, the effect of the total numbers of elements on the simulation accuracy is estimated. For instance, when the true contact area is 16×10^{-4} m^2, a comparison of the results (i.e., focused signal amplitude) is shown in Table 3-2, and one can ignore the error from elements when the total number of elements is large enough.

Table 3-2 Simulation results under different number of elements

Number of elements	Simulation results
4,000	0.743
6,000	0.739
8,000	0.746
11,000	0.751
16,000	0.752

Finally, combining the eqn. (3-10) and the simulation results (Fig. 3-10) results in the relationship between bolt preload and the focused signal peak amplitude, and the result is depicted in Fig. 3-11. Notably, the fractal parameters D and G are measured as 1.4058 and 6.1852×10^{-13} m via a surface profiler shown in Fig. 3-12. Like the numerical results in subchapter 3.3, the focused signal peak amplitude increases with the increasing of bolt preload, and there is a saturation under overlarge preload.

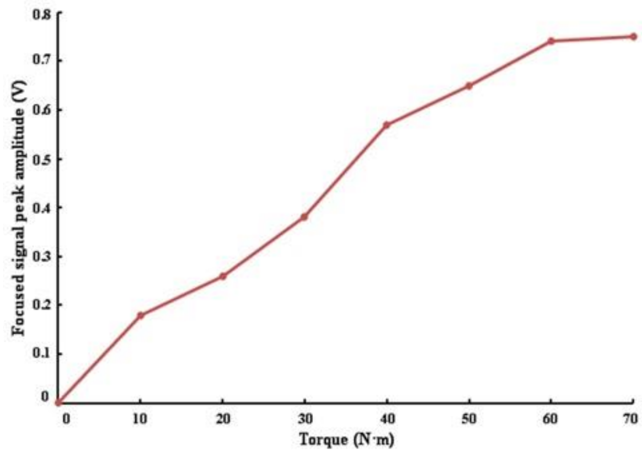

Fig. 3-11 Bolt preload versus focused signal peak amplitude

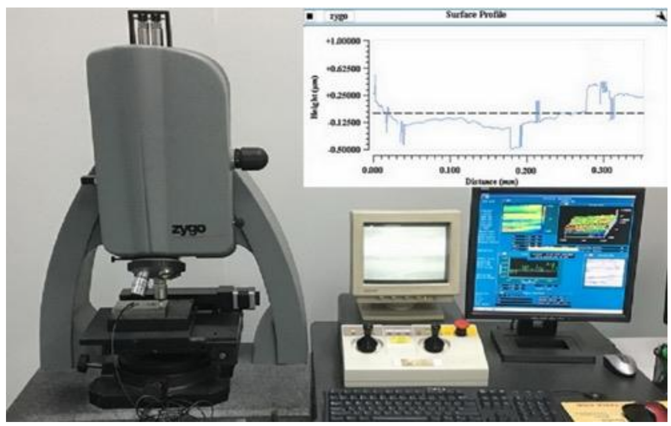

Fig. 3-12 The Zygo surface profiler and the measured surface profile

To demonstrate the accuracy of the proposed semi-analytical model, the author performs an experiment, as shown in Fig. 3-13. The NI DAQ system (NI USB 6366) is used to emit a Gaussian pulse with a center frequency of 100 kHz and a 10V amplitude to actuate PZT 1 to generate ultrasonic waves. After the forward propagation procedure, the waves can be captured by PZT 2. Then, the received signals is reversed in the time domain and is emit by PZT 2. Finally, the focused signal can be obtained by PZT 1. An example of this forward and reversal propagation is illustrated in Fig. 3-14. On the other hand, a torque wrench is used to apply the preload to the bolt, and the relationship between torque and axial preload is given as

$$0.15 \times F_{axial} \times d = T\,, \tag{3-14}$$

where d is the nominal diameter of the bolt (12 mm in this subsection).

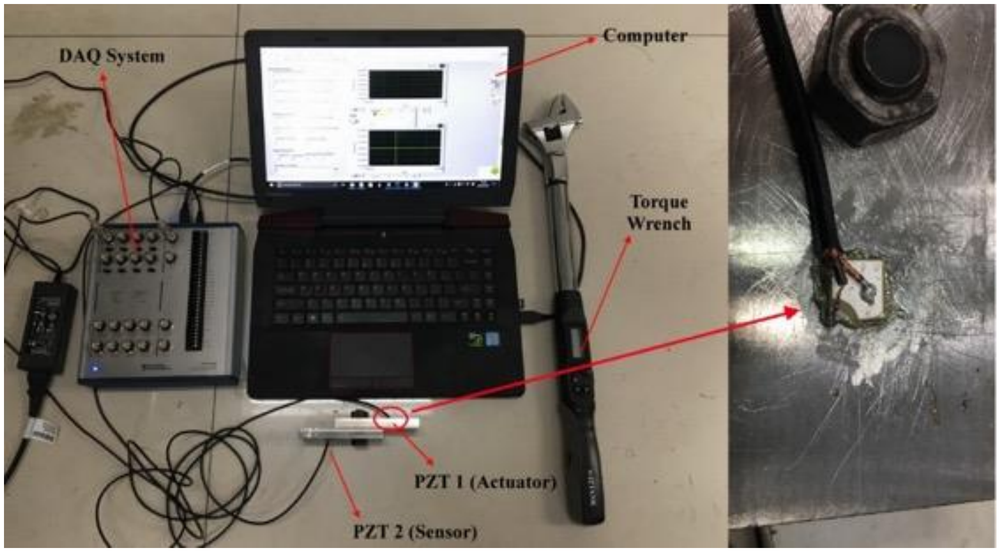

Fig. 3-13 Experimental setup

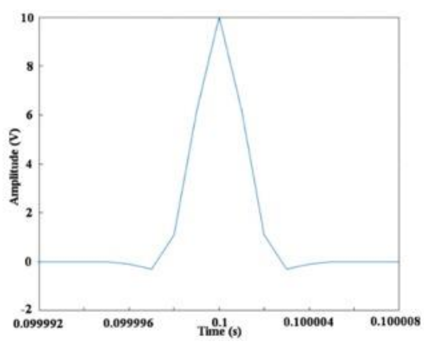

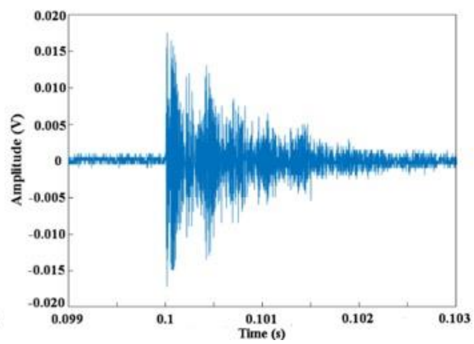

(a) Pulse signal (b) Received signal

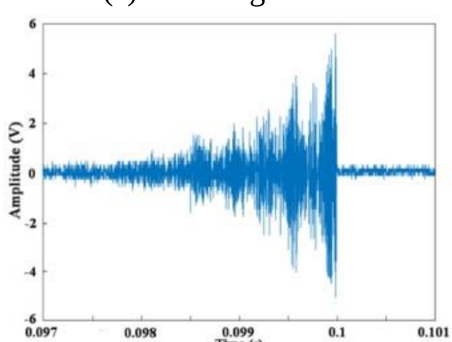

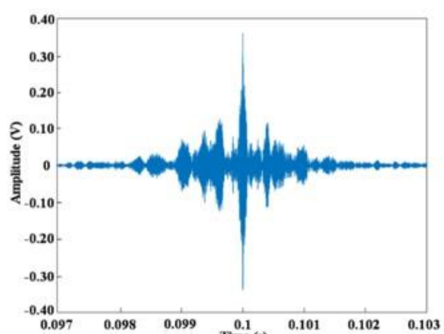

(c) Reversed signal (d) Focused signal

Fig. 3-14 Experimental signals

Under each bolt preload, the effectiveness of the proposed model is verified by comparing experimental results and predicted results (Fig. 3-11). The results are given in Table 3-3, and it is clear that the error is small, thus demonstrating the accuracy.

Table 3-3 Comparison between the predicted values and the experimental values

Axial preload (Nm)	Predicted value (V)	Experimental value (V)	Error (%)
10	0.18	0.17	5.9
20	0.26	0.28	7.1
30	0.38	0.35	8.6
40	0.57	0.54	5.5
50	0.65	0.68	4.4
60	0.74	0.72	2.3
70	0.75	0.72	4.2

3.5 Analytical modeling of the active sensing method

In the last subchapter, the relationship between energy dissipation of ultrasonic waves and the true contact area is obtained via the numerical simulation, which constructs a semi-analytical model. In this subchapter, this relationship will be developed by an analytical model, thus proposing an analytical model of the active sensing method.

Overall, it is well known that the signal energy dissipation is due to the tangential damping of the bolted joint when ultrasonic waves propagate across the bolted interface. Based on the previous investigation [101], one can express the tangential damping w_d of a single asperity under external load as

$$w_d = \frac{F_t^3}{36rG'\mu F_n}, \tag{3-15}$$

where F_t is the tangential load, F_n is the normal preload, μ is the coefficient of friction, r is the radius of the asperity's true contact area. Moreover, G' is the equivalent shear modulus, and it can be computed as

$$G' = \left[\left(2-\upsilon_1\right)/G_1 + \left(2-\upsilon_2\right)/G_2 \right]^{-1}, \tag{3-16}$$

where G_1 and G_2 are shear moduli of two contact materials, respectively.

Then, with the assumption that the load applied to the asperity is proportional to the contact area, the following relationship is obtained as

$$F_t = A \cdot F_T / A_r \quad F_n = A \cdot F / A_r \ , \tag{3-17}$$

where F_T is the total tangential load that is used to the bolted connection, F is the total applied axial preload, A_r is the nominal contact area. Substituting eqn. (3-17) into eqn. (3-15) gives the following equation based on the relationship between the truncated area A' and true contact area A as

$$w_d = \frac{\pi^{1/2} \left(1/2\right)^{3/2} F_T^3 A'^{3/2}}{36 G' \mu F A_r^2} \ . \tag{3-18}$$

Finally, based on the normalization method, the author constructs the energy dissipation modeling W_d of bolted connection, which is caused by tangential damping as

$$\begin{aligned} W_d^* &= \frac{W_d}{G' A_a^{3/2}} = \frac{\int_{110^{1/(1-D)} a_c'}^{A_1'} w_d n\left(A'\right) dA'}{G' A_a^{3/2}} \\ &= \frac{0.017 g\left(D\right)\left(F_T^*\right)^2 \psi^{\frac{(D-2)^2}{4}} A_r^{*\frac{D}{2}}}{\mu A_r^{*2}} \frac{F_T}{F} \times \left[\left(\frac{2-D}{D}\right)^{\frac{3-D}{2}} \psi^{\frac{(3-D)(D-2)}{4}} A_r^{*\frac{3-D}{2}} - 110^{\frac{3-D}{2(1-D)}} a_c^{*\frac{3-D}{2}} \right], \end{aligned} \tag{3-19}$$

where $F_T^* = \dfrac{F_T}{G' A_a}$, $g\left(D\right) = \dfrac{D}{3-D}\left(\dfrac{2-D}{D}\right)^{D/2}$. Moreover, F_T [105] can be calculated as

$$F_T = T A_r \ , \tag{3-20}$$

where T is the stress, which can be calculated by the piezoelectric constitutive equation [106] as

$$\begin{aligned} S &= sT + d_{31}E \\ D &= d_{31}T + \varepsilon E \end{aligned}, \tag{3-21}$$

where S is the strain, E is the electric field, s is the compliance constant, d_{31} is the piezoelectric strain coefficient, D is the electric displacement, ε is the dielectric constant. The values of all the above parameters are given in Table 3-1.

To demonstrate the effectiveness of the proposed analytical model, the author performs an experiment, as illustrated in Fig. 3-15. All setups are the same as those in the last subchapter (Section 3.4), and the energy of signals E_c that are emitted and captured by PZT patches can be computed as

$$E_c = \int_{t=t_s}^{t_f} E_c(t)dt = \frac{1}{2}\int_{t=t_s}^{t_f} H \cdot V(t)^2 dt, \tag{3-22}$$

where H is the equivalent capacitance of the piezoelectric patches [106], $V(t)$ is the signal voltage.

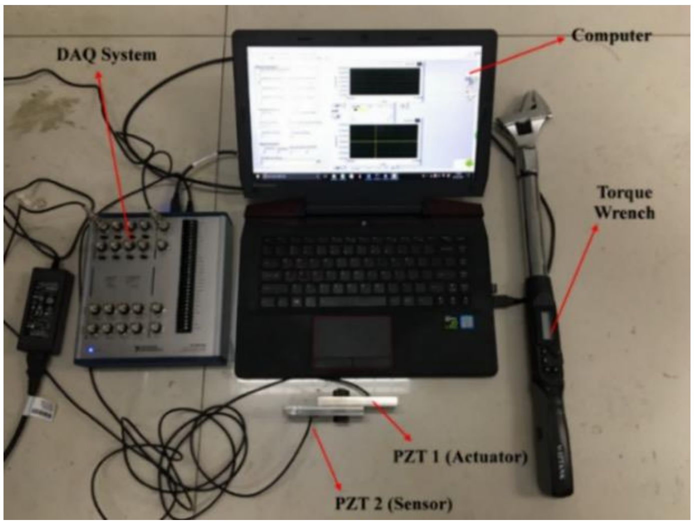

Fig. 3-15 Apparatus of the experiment

Moreover, to measure the fractal parameters D and G, a phase grating interference surface roughness profiler (TALOR HOBSON, PGI 840, UK) is employed to obtain 2D surface topography, as depicted in Fig. 3-16. Using a surface profile $z(x)$, one can obtain its structural function $S(\tau)$ [107] as

$$S(\tau) = \left\langle \left[z(x) - z(x+\tau) \right]^2 \right\rangle = C\tau^{4-2D}, \tag{3-23}$$

where τ is surface profiler's sampling length, $\langle \ \rangle$ is the averaging statistical ensemble. Furthermore, C is the scaling coefficient, which can be calculated [107] as

$$C = \frac{\Gamma(2D-3)\sin\left[(2D-3)\pi/2\right]}{2-D} G^{2(D-1)}. \tag{3-24}$$

Then, D and G is calculated as 1.4102 and 6.2042×10^{-13} m in this subchapter. It is worth noting that they are almost the same as the results measured by another surface profiler (Zygo, NewView 5022, USA) in the last subchapter (D and G are measured as 1.4058 and 6.1852×10^{-13}m). Therefore, this phenomenon verifies the certainty of fractal properties. Based on the measured D and G, the relationship between the energy dissipation W_d and bolt axial preload is generated, as shown in Fig. 3-16.

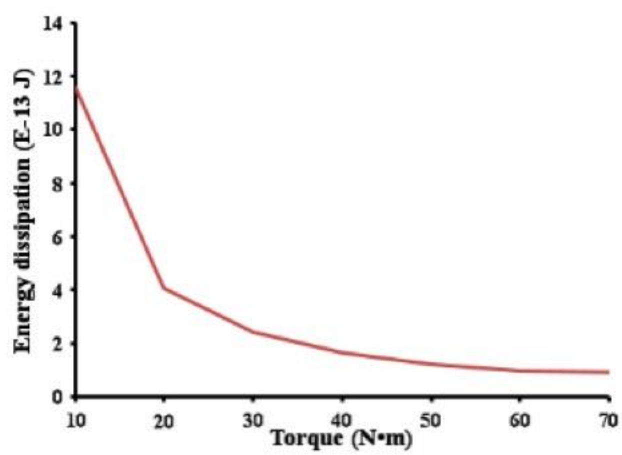

Fig. 3-16 The energy dissipation under different preloads

According to Fig. 3-16, it can be seen that larger applied preload will reduce the energy dissipation more significantly, and a saturation still exists, which conforms to the previous results in subchapter 3.3 and 3.4. Moreover, recalling eqn. (3-19), one can know that smaller D and larger G (more severe roughness) can lead to larger energy dissipation. This phenomenon is in accordance with investigations developed by Britton et al. [108] and Xiao et al. [109].

Finally, the experiment is repeated three times, and the results are illustrated in Fig. 3-17. Then, the comparison between average experimental results and predicted values are given in Table 3-4, which verifies the proposed model.

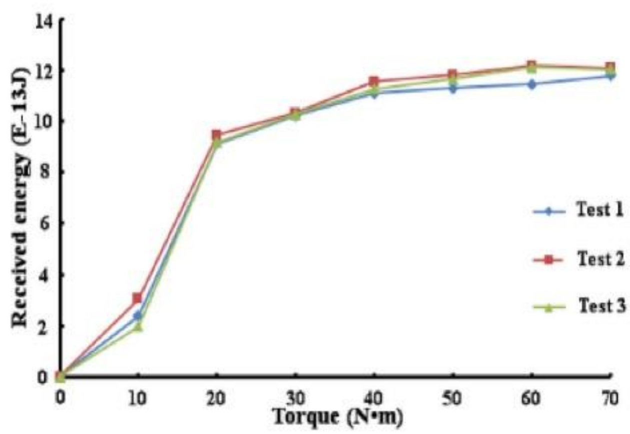

Fig. 3-17 The Received signal energy under different torque levels

Table 3-4 Comparison of the predicted values and the experimental verification values

Axial preload (Nm)	Emitted energy (J)	Received Energy (J)	Experimental value (J)	Predicted value (J)	Error (%)
10	13.1E-13	2.46E-13	10.64E-13	11.57E-13	8.74
20	13.1E-13	9.25E-13	3.85E-13	4.09E-13	6.23
30	13.1E-13	10.27E-13	2.83E-13	2.44E-13	13.78
40	13.1E-13	11.30E-13	1.80E-13	1.67E-13	7.22
50	13.1E-13	11.58E-13	1.52E-13	1.24E-13	18.42
60	13.1E-13	11.90E-13	1.20E-13	0.96E-13	20
70	13.1E-13	11.96E-13	1.06E-13	0.92E-13	19.3

CHAPTER 4. ENTROPY-ENHANCED ACTIVE SENSING METHOD FOR BOLT LOOSENESS DETECTION

As introduced in Chapter 3, the current active sensing method depends on signal amplitude and energy as an index to estimate the looseness of the bolted connection. However, both experimental results and theoretical (numerical simulation, semi-analytical, and analytical modeling) results demonstrate that a saturation exists when larger preload is applied to the bolted connection. In other words, the current active sensing method in incapable detection of bolt early looseness, which is the main drawback. Moreover, no investigation about multi-bolt looseness detection via the active sensing method has been reported yet. Thus, in this chapter, inspired by previous investigations [110, 111, 112, 113, 114], the author developed several novel entropy-enhanced active sensing methods to solve the deficiencies of the current active sensing method.

4.1 Introduction of entropy for time series

Initially, the concept of entropy was derived in the 1850s in the field of thermodynamics (specifically, the second law of thermodynamics). Then, Shannon [115] developed the Shannon entropy, which is a powerful tool in the field of information science, to estimate the complexity of time series. The computation procedure of the Shannon entropy under different cases can be expressed as follows.

(1) Given a discrete variable Y with the probability function $p(Y)$, one can define the entropy as a function $H(Y)$ of Y, which can be expressed as

$$H(Y) = E\{I(Y)\} = E\{-\log(p(Y))\}, \tag{4-1}$$

where $I(Y) = -\log(p(Y))$ is the information content of Y.

(2) Then, supposing that Y has several possibilities $\{y_1, y_2, \cdots, y_n\}$ with corresponding probability function $p_i = P(Y = y_i)$, one can expand the entropy as

$$\begin{aligned} H(Y) &= E\{I(Y)\} = E\{-\log(p(Y))\} \\ &= \sum_{i=1}^{n} (p_i \times (-\log(p_i))) = -\sum_{i=1}^{n} (p_i \log p_i) \end{aligned} \cdot \tag{4-2}$$

Particularly, when Y is a continuous variable with the probability function $f(Y)$, the entropy $H(Y)$ can be expressed as

$$\begin{aligned} H(Y) &= E\{I(Y)\} = E\{-\log(f(Y))\} \\ &= -\int f(Y) \times \log(f(Y)) dY \end{aligned} \; . \tag{4-3}$$

(3) In terms of two continuous variables X and Y, one can set their possibilities as I and J. Then, the marginal mass density functions of X and Y are defined as

$$\begin{aligned} p_X(x_i) &= \sum\nolimits_{j=1}^{J} p(x_i, y_j) \\ p_Y(y_j) &= \sum\nolimits_{i=1}^{I} p(x_i, y_j) \end{aligned} , \tag{4-4}$$

where x_i is the element of X, y_i is the element of Y, $p(x_i, y_i)$ is the probability of the joint (x_i, y_i).

Subsequently, the entropy $H(X,Y)$ of joint (x_i, y_i) can be computed as follows:

$$\begin{aligned} H(X,Y) &= E_{X,Y}\{I(X,Y)\} = E_{X,Y}\{-\log(p(X,Y))\} \\ &= -\sum_{i=1}^{I} \sum_{j=1}^{J} \left(p(x_i, y_j) \log(p(x_i, y_j)) \right) \end{aligned} , \tag{4-5}$$

$$\begin{aligned} H(X) &= E_X\{-\log(p(X))\} = -\sum_{i=1}^{I} \left(p_X(x_i) \log(p_X(x_i)) \right) \\ &= -\sum_{i=1}^{I} \sum_{j=1}^{J} \left(p(x_i, y_j) \log(p_X(x_i)) \right) \\ &= -\sum_{i=1}^{I} \sum_{j=1}^{J} \left(p(x_i, y_j) \log(\sum_{j=1}^{J} p(x_i, y_j)) \right) \end{aligned} , \tag{4-6}$$

and

$$
\begin{aligned}
H(Y) = E_Y\{-\log(p(Y))\} &= -\sum_{j=1}^{J}\left(p_Y(y_j)\log(p_Y(y_j))\right) \\
&= -\sum_{i=1}^{I}\sum_{j=1}^{J}\left(p(x_i, y_j)\log(p_Y(y_j))\right) \\
&= -\sum_{i=1}^{I}\sum_{j=1}^{J}\left(p(x_i, y_j)\log(\sum_{i=1}^{I} p(x_i, y_j))\right)
\end{aligned}
\quad . \qquad (4\text{-}7)
$$

Moreover, the conditional entropy of X and Y can be expressed as

$$
H_X(Y) = E_{X,Y}\{-\log(p(Y|X))\} = -\sum_{i=1}^{I}\sum_{j=1}^{J}\left(p(x_i, y_j)\log\frac{p(x_i, y_j)}{\sum_{j=1}^{n} p(x_i, y_j)}\right). \qquad (4\text{-}8)
$$

Finally, analyzing the above three cases gives the following properties:

(1) If and only if all p_i (except one) are zero, $H = 0$. In other words, H vanishes when we are certain of Y.

(2) H is maximum when all p_i are the same ($1/n$), and the value is $\log n$.

(3) H will increase when p_i toward equalization.

(4) $H(X,Y) \le H(X) + H(Y)$, $H(X,Y) = H(X) + H_X(Y)$, $H(Y) \ge H_X(Y)$.

Moreover, several entropy methods (such as Kolmogorov entropy [116], E-R entropy [117], compression entropy [118], approximate entropy [119], sample entropy [120], permutation entropy [121], fuzzy entropy [122], and transfer entropy [123, 124, 125, 126, 127]) have been developed to overcome the drawbacks of the Shannon entropy.

4.2 Entropy-enhanced active sensing method for detection of bolt early looseness

In this subchapter, based on the multiscale permutation entropy (MPE) [128], the author proposed an entropy-enhanced active sensing method to detect bolt early looseness. Overall, MPE is the combination of the multiscale entropy (MSE) [129] and permutation entropy [122]. Additionally, inspired by MSE, many researchers have proposed various multiscale based entropy (including composite multiscale entropy [130] refined composite multiscale entropy [131], short-time multiscale entropy [132], modified multiscale entropy [133], refined multiscale entropy [134], generalized multiscale entropy [135], intrinsic mode entropy [136], adaptive multiscale entropy [137], multiscale symbolic entropy [138], multiscale compression entropy [139], multiscale fuzzy entropy [140]), which has attracted much attention in analyzing the complexity of time series. Therefore, the MSE will be introduce firstly.

The past decades have seen the rapid development of MSE and its application in scrutinizing the complexity of multiple time series, including heartbeat signals [141], electroencephalogram [142, 143], cardiovascular [144, 145, 146], functional magnetic resonance signal [147], magnetoencephalogram [148], gait time series [149], lung sound signal [150], vibration signal [151], financial market time series [152, 153, 154, 155, 156], traffic system time series [157, 158], geophysical time series [159, 160, 161], and flow time series [162, 163]. Overall, the procedure of the MSE calculation can be divided into two steps: (1) extracting various scales of time series, and (2) entropy computation over those extracted scales. More detailed implementation can be expressed as follows.

(1) Given a time-series $X = \{x(1), \cdots x(i), \cdots, x(N)\}$, the "coarse-grained" procedure is first implemented, as shown in Fig. 4-1 [164]. Then, a new time-series signal can be obtained as

$$Y = \{y^{(\tau)}(1), y^{(\tau)}(2), \cdots, y^{(\tau)}(j)\}, \tag{4-9}$$

where $y^{(\tau)}(j) = 1/\tau \sum_{i=(j-1)\tau+1}^{j\tau} x(i), 1 \le j \le N/\tau$, τ is the scale factor.

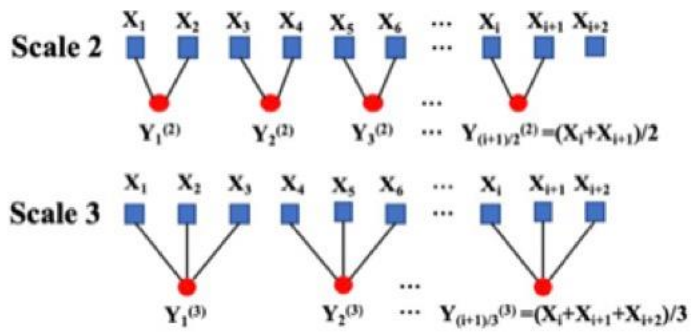

Fig. 4-1 Schematic illustration of the coarse-grained procedure

(2) A m dimensional vector can be constructed as

$$Y(k) = (y^{(\tau)}(k), y^{(\tau)}(k+1), \cdots, y^{(\tau)}(k+m-1)) , \tag{4-10}$$

where $k = 1, 2, \cdots, N-m+1$, and the distance between two vectors can be defined as their maximum difference of corresponding components as

$$d[Y(a) - Y(b)] = \max \left| y^{(\tau)}(a+l) - y^{(\tau)}(b+l) \right| , \tag{4-11}$$

where $a, b \in k;\ 0 \le l \le m-1$.

(3) By defining a tolerance r, one can obtain the total number $count(d[Y(a)-Y(b)])$ of distance that is within the range of r, and the compute the similarity degree as

$$B_k^m(r) = count(d[Y(a)-Y(b)])/(N-m-1) . \tag{4-12}$$

(4) The average of $B_k^m(r)$ can be calculated as

$$B^m(r) = \sum_{i=1}^{N-m} B_k^m(r) \big/ (N-m) . \tag{4-13}$$

(5) By repeating Steps (2)-(4), one can get the average similarity degree $B_k^{m+1}(r)$ in dimension $m+1$.

(6) Then, the Sample entropy is computed as

$$SampEn(m, r, N) = \ln(B^m(r) \big/ B^{m+1}(r)) . \tag{4-14}$$

(7) Finally, repeating Steps (1) to (6) gives the MSE under different scale factor τ as

$$MSE(m,r,N)=\{\tau \mid SampEn(m,r,N)\}. \quad (4\text{-}15)$$

Subsequently, inspired by MSE, one can calculate the MPE as follows.

(1) Denoting a time-series $X=\{x(1),\cdots x(i),\cdots,x(N)\}$, one can map it to a m dimensional vector at time i as

$$\mathbf{x}_i^m=[x(i),x(i+t),\cdots,x(i+(m-1))t], \quad (4\text{-}16)$$

where t is the delay.

(2) Assume that $\mathbf{x}_i^m$ has a permutation $\pi(r_0 r_1 \cdots r_{m-1})$ under the following condition as

$$x(i+r_0 t)\le x(i+r_1 t)\le \cdots \le x(i+r_{m-1}t), \quad (4\text{-}17)$$

where $0\le r_i\le m-1$ and $r_i\ne r_j$.

(3) Based on the definition in Step (2), it is clear that $\mathbf{x}_i^m$ has $m!$ possible permutations, and the relative frequency for each π can be expressed as

$$p(\pi)=\frac{Number\left\{i \middle| i\le T-(m-1)t,\mathbf{x}_i^m has\ type\ \pi\right\}}{N-m+1}. \quad (4\text{-}18)$$

(4) The PE and normalized PE (NPE) of $\mathbf{x}_i^m$ can be computed as follows:

$$H_{PE}(m)=-\sum p(\pi)\ln(p(\pi)) \quad (4\text{-}19)$$

and

$$H_{NPE}(m)=H_{PE}(m)/\ln(m!). \quad (4\text{-}20)$$

(5) Finally, one can implement the "coarse-grained" procedure, which is the same as MSE, to obtain the following new time-series

$$Y=\{y^{(\tau)}(1),y^{(\tau)}(2),\cdots,y^{(\tau)}(j)\}, \quad (4\text{-}21)$$

where $y^{(\tau)}(j)=1/\tau\sum_{i=(j-1)\tau+1}^{j\tau}x(i), 1\le j\le N/\tau$, τ is the scale factor. The MPE can be obtained by computing NPE under each scale.

To verify the effectiveness of MPE, the author conducts an experiment, as shown in Fig. 4-2 [164]. The experimental apparatus consists of a bolted joint, two PZT patches, a computer equipped with a customized LabVIEW program, a torque wrench, an NI-DAQ system (NI USB 6363), and a power amplifier (Trek Model 2100HF). The bolted joint is constructed by tightening two steel plates (size: 150 mm×80 mm×20 mm) via a M20 bolt. Moreover, eleven degrees of tightness (from 0 Nm to 100 Nm, interval: 10 Nm) are applied to the bolted joint through the torque wrench.

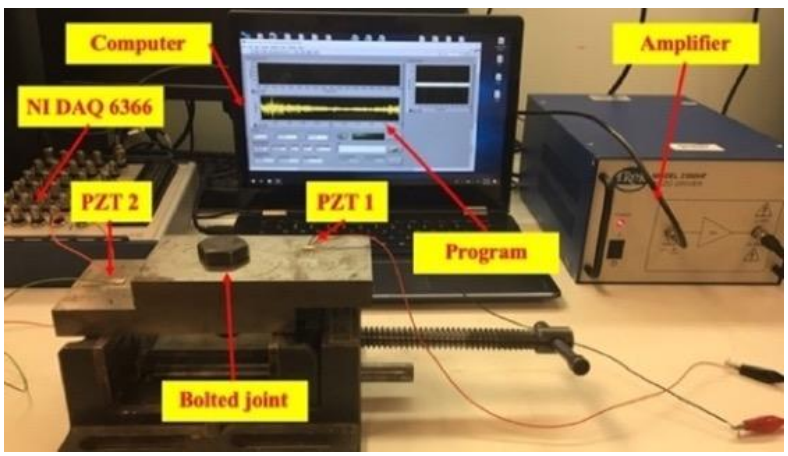

Fig. 4-2 Experimental apparatus

The overall experimental procedure follows the active sensing. A swept frequency wave (duration: 0.01 second) is generated by the NI DAQ system to excite PZT 1, and the frequency range of the wave is from 100 kHz to 300 kHz. Particularly, this wave signal is augmented fiftyfold (amplitude: from 1V to 50 V) to ensure enough power before feeding into PZT 1. After the stress waves propagate across the bolted interface, PZT 2 can capture these waves (sampling rate: 1 MHz), which are then converted to the digital signal by the NI DAQ system. I will compute the MPE value of the saved signal to estimate the looseness of bolted joint, instead of the signal energy.

The saved signals under different preloads are depicted in Fig. 4-3(a) [164], and I calculated corresponding energy, which is shown in Fig. 4-3(b) [164], which shows that the signal energy increases monotonically when the applied torque is below 50 Nm. However, this tendency is prone to saturation when the applied torque is larger than 50 Nm. This phenomenon conforms to the principle of the active sensing (which has been discussed in Chapter 3), and it is the deficiency of the active sensing. In other words, we cannot accurately detect bolted looseness at the range of 50 Nm to 100 Nm.

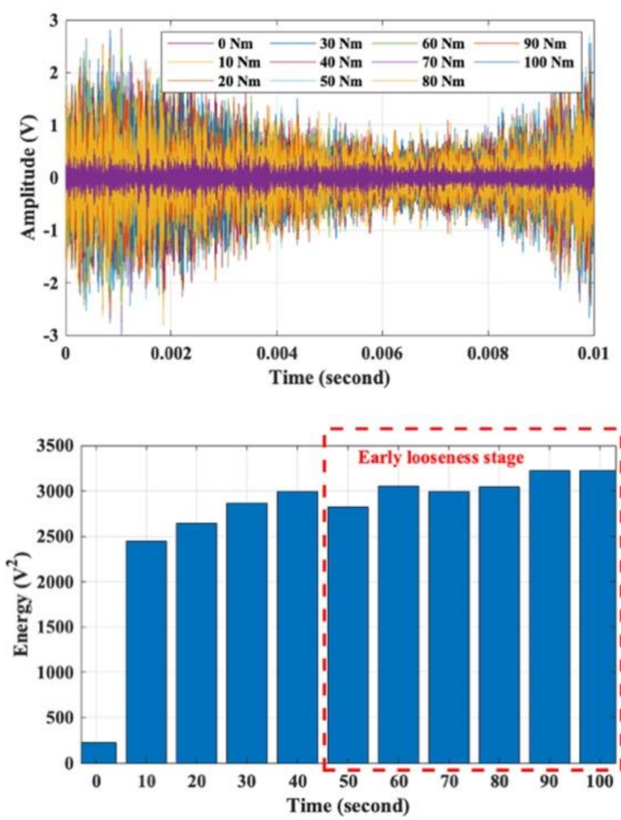

Fig. 4-3(a) Received signal and (b) signal energy versus applied bolt preload

Therefore, the bolt preload with the range from 50 Nm to 100 Nm is defined as the "early looseness," which can be detected and monitored via the MPE index. As introduced earlier, the length of saved signals is 10, 000 (0.01 second ×1 MHz). Then, after trail-and-error, the time delay t and embedded dimension m of MPE are selected as 1 and 5, respectively. The calculation results of MPE under different bolt preloads are illustrated in Fig. 4-4 [164] (scale factor τ is 10).

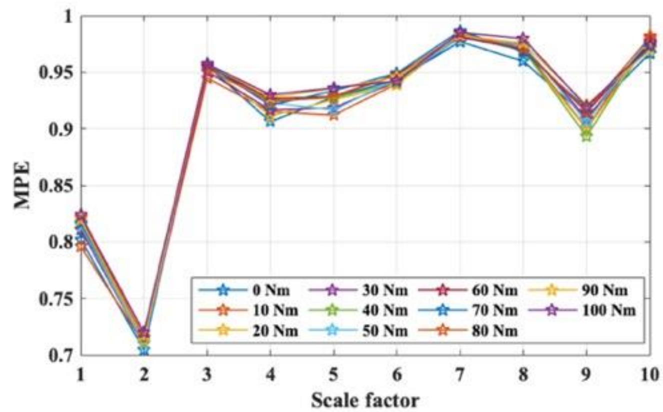

Fig. 4-4 MPE diagram versus bolt preloads

Then, to develop a straightforward relationship between MPE values and bolt preload, a new MPE-based damage index (DI) is proposed as

$$DI = 20\log(\frac{1}{n}\sum_{\tau=1}^{n} E^{(\tau)}), \tag{4-22}$$

where $E^{(\tau)}$ is the MPE values under scale factor τ, and n is the maximum scale factor.

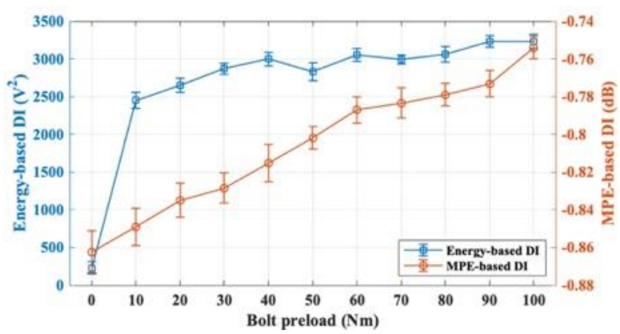

Fig. 4-5 MPE-based DI for bolted looseness monitoring

Finally, the relationship between the proposed MPE-based DI and the bolt preload is depicted in Fig. 4-5 [164]. Notably, to ensure the repeatability of the proposed method, the experiment is repeated ten times. It can be seen that the proposed MPE-based DI increases monotonically with larger bolt preload, which demonstrates that the efficacy of the proposed entropy-enhanced active sensing method.

4.3 Entropy-enhanced active sensing method for on land multi-bolt looseness detection

Notably, the investigation of multi-bolt looseness detection via the active sensing is limited so far, and more attention is paid on other methods. For instance, several studies [165, 166, 167] have demonstrated that the EMI method and magneto-mechanical impedance method [48] can be used to detect multi-bolt looseness with the help of the machine learning (ML) techniques. In addition, the vibration-based method [33, 40, 168, 169, 170], the vibro-acoustic modulation (VAM) method [171], and the impact-acoustic modulation (IAM) method [172] have shown the potential for multi-bolt looseness. However, all the above methods have some drawbacks that impede their further applications. Electrotechnical impedance method is affected by ambient temperature significantly, and the vibration-based/VAM/IAM methods require prudently selected external excitations, which are difficult to implement in some complex working conditions.

Therefore, in this subchapter, the author will develop a new entropy-enhanced active sensing method, which is based on the multivariate multiscale fuzzy entropy (MMFE), to detect on-land multi-bolt looseness. The overall flowchart of the proposed method is illustrated in Fig. 4-6. First, based on the active sensing method, the author constructs the training and testing datasets under different degrees of bolt looseness. Second, features form the training and testing datasets are extracted via the MMFE algorithm [173] to develop the new damage index (DI). Then, with the help of the max-relevance and min redundancy (mRMR) algorithm [174], the first four more significant features can be obtained (i.e., dimension reduction) from the MMFE-based features. Finally, a genetic algorithm-based least square support vector machine (GA-LSSVM) classifier [175] is trained via the training dataset to achieve multi-bolt looseness, and its effectiveness can be verified through the testing dataset.

Fig. 4-6 Flowchart of the proposed MMFE-enhanced active sensing method

As introduced earlier, MSE has been widely used across multiple applications, and a recent investigation has extended the MSE to the multivariate multiscale sample entropy (MMSE) [176] to implement entropy estimation of multichannel time-series. However, an intrinsic drawback of MSE/MMSE is the method of calculating similar degree (Heaviside function), which has been described in Chapter 4.2. Specially, this Heaviside function has a solid boundary, which can lead to discontinuity. For instance, as shown in Fig. 4-7, one can consider that points 2 and 3 are similar to point 0, since they are all within the boundary of the Heaviside function. Though point 1 is near point 2 in distance, it is still regarded as dissimilarity. In other words, the Heaviside function may downgrade the accuracy of the entropy estimation. Therefore, attempting to solve this problem, some researchers have replaced the Heaviside function by the Gaussian function to propose the fuzzy entropy [122, 140]. Particularly, the MMFE [173] has been proposed based on the concept of the MMSE, and its computation procedure is given as follows.

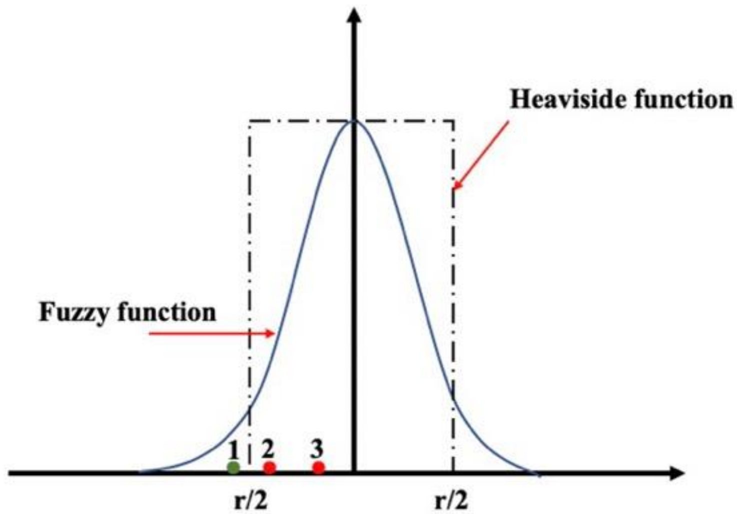

Fig. 4-7 Heaviside function and fuzzy function for entropy estimation

(1) Given a time-series $\{x_{k,i}\}_{i=1}^{N}$ $k=1,2,\cdots,p$, one can construct the m dimensional composite vector $X_m(i)\in\mathbb{R}^m$, and $i=1,2,\cdots,N-n$. n can be computed as

$$\max\{M\}\times\max\{\tau\}, \tag{4-23}$$

where $M=[m_1,m_2,\cdots m_p]\in\mathbb{R}^p$ is the embedding vector, and $\boldsymbol{\tau}=[\tau_1,\tau_2,\cdots,\tau_p]$ is the time lag vector.

(2) Then, the local mean $x_0(i)=\sum_{j=0}^{m-1}x(i+j)/m$ can be removed from each vector as

$$X_m(i)=[x(i)-x_0(i),x(i+1)-x_0(i),\cdots,x(i+m-1)-x_0(i)]. \tag{4-24}$$

(3) The maximum norm d_{ij}^m can be obtained by the distance between two vectors as

$$d_{ij}^m=\mathbf{distance}[X_m(i),X_m(j)]=\max_{l=1,\cdots,m}\{|x(i+l-1)-x(j+l-1)|\}. \tag{4-25}$$

(4) Subsequently, define a new function $B^m(r)$, which can be expressed as

$$B^m(r)=\frac{1}{N-n}\sum_{i=1}^{N-n}\left(\frac{1}{N-n-1}\sum_{j=1,i\neq j}^{N-n-1}D_{ij}^m\right), \tag{4-26}$$

where r is the tolerance, $D_{ij}^{m}=\mu(d_{ij}^{m},r)$ is the similarity degree, and it can be calculated via a Gaussian function as

$$\mu(d_{ij},r)=\exp(-(d_{ij})^2 / 2r^2)\,. \tag{4-27}$$

(5) Extending dimension m to $m+1$ gives the vectors $X_{m+1}(i)\in\mathbb{R}^{m+1}$.

(6) Then, repeating Steps (2)-(4) gives $B^{m+1}(r)$ as

$$B^{m+1}(r)=\frac{1}{p(N-n)}\sum_{i=1}^{p(N-n)}\left(\frac{1}{p(N-n)-1}\sum_{j=1,i\neq j}^{p(N-n)-1}D_{ij}^{m+1}\right), \tag{4-28}$$

where $D_{ij}^{m+1}=\mu(d_{ij}^{m+1},r)$.

(7) By using $B^{m+1}(r)$ and $B^{m}(r)$, the multivariate fuzzy sample entropy (MFSampEn) can be calculated as

$$MFSampEn(M,\tau,r,N)=-\ln\left[\frac{B^{m+1}(r)}{B^{m}(r)}\right]. \tag{4-29}$$

(8) Finally, the MMFE can be obtained by calculating MFSampEn under different scale factors.

It is well known that over many extracted features can deteriorate the classification accuracy since some of features may be redundancy. That is to say, one need to select the most significant features from data to ensure optimal classification results. Among different methods [177, 178], the most popular approach is the mRMR algorithm [174], whose procedure can be implemented as the following steps.

(1) Denoting two random variables x and y with corresponding probabilistic density functions $p(x)$ and x, one can obtain the mutual information as

$$I(x;y)=\iint p(x,y)\log\frac{p(x,y)}{p(x)p(y)}dxdy\,, \tag{4-30}$$

where $p(x,y)$ is the function of the joint probabilistic density.

(2) A feature subset S can be obtained by selecting the features with max-relevance and min-redundancy under the following criterions

$$\max D(S,c) \quad D=\frac{1}{|S|}\sum_{x_i\in S} I(x_i;c); \quad \min R(S) \quad R=\frac{1}{|S|^2}\sum_{x_i,x_j\in S} I(x_i;x_j)\,, \tag{4-31}$$

where c is the target class, $I(x;c)$ is the mutual information between x and c, $|S|$ is the total of features in the feature subset S.

(3) Upon the above two criterions, one can define the following operators as

$$\max\Phi(D,R) \quad \Phi=D-R; \quad \max\Phi(D,R) \quad \Phi=D/R\,. \tag{4-32}$$

(4) Finally, in terms of set $\{x-S_{m-1}\}$, one can obtain the m^{th} feature via the following criterions

$$\max_{x_j\in x-S_{m-1}}\left[I(x_j;c)-\frac{1}{m-1}\sum_{x_i\in S_{m-1}} I(x_j;x_i)\right]; \quad \max_{x_j\in x-S_{m-1}}\left[I(x_j;c)\Big/\frac{1}{m-1}\sum_{x_i\in S_{m-1}} I(x_j;x_i)\right]. \tag{4-33}$$

The core issue of multi-bolt looseness detection is to find an effective classifier. In this subsection, the author selects the GA-LSSVM classifier, which is based on the traditional support vector machine (SVM). Overall, SVM is a data-driven method that can implement classification via the hyperplane [179]. For instance, as illustrated in Fig. 4-8(a) [180], one can separate two kinds of data (red circle and blue rectangle) by using a hyperplane $w\cdot x+b=0$. Particularly, the best performance (classification accuracy) can be ensured by maximizing the margin $2/\|w\|$ between two boundaries

$|w \cdot x+b|=1$. Furthermore, the nonlinear classification can be accomplished through a nonlinear mapping function ϕ, as shown in Fig. 4-8(b) [180].

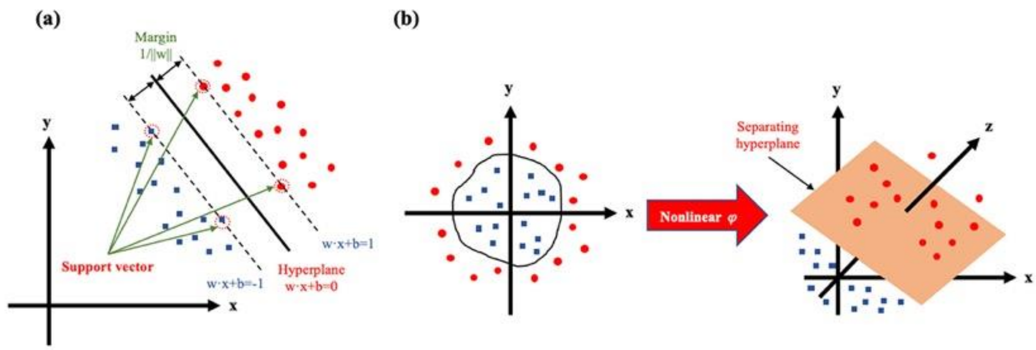

Fig. 4-8 (a) SVM for linear classification (b) SVM for nonlinear classification

Subsequently, the least square support vector machine (LSSVM) [181] is developed to enhance the capacity of SVM.

(1) First denote a training dataset as

$$U=\{(x_i, y_i), x_i \in \mathbb{R}^n, y_i \in \mathbb{R}\}_{n=1}^{N}, \tag{4-34}$$

where x_i represents the input, y_i is the target value, N is the total number of samples.

(2) Develop the LSSVM classifier as

$$y(x)=w^T \phi(x)+b, \tag{4-35}$$

where $w \in \mathbb{R}^n, b \in \mathbb{R}$ are the modal parameters.

(3) Then, the classification can be achieved by implementing the following optimization

$$Min(w,b,e)=\frac{1}{2}w^T w+\frac{\gamma}{2}\sum_{i=1}^{N}e_i^2=E_w+\gamma \cdot E_D, \tag{4-36}$$

where γ denotes the penalty factor, e_i is the prediction error.

(4) Solving eqn. (4-36) with the help of Lagrange Multiplier gives the following matrix

$$\begin{bmatrix} 0_{1\times n} & 1_{1\times n} \\ 0_{n\times 1} & P+1/\gamma \end{bmatrix}\begin{pmatrix} b \\ \alpha \end{pmatrix}=\begin{pmatrix} 0 \\ y \end{pmatrix}, \tag{4-37}$$

where $P = K(x, x_i) = \phi(x)^T \phi(x_j)$ is the Kernel function, α is the Lagrange multiplier.

(5) Finally, one can rewrite the LSSVM classifier as

$$y(x) = \sum_{i=1}^{N} \alpha_i K(x, x_i) + b; \quad K(x, x_i) = \exp\left(-\frac{\|x - x_i\|^2}{\sigma^2} \right), \tag{4-38}$$

where σ^2 is the Kernel bandwidth parameter. Particularly, the radial basis function [182] is employed as the Kernel function.

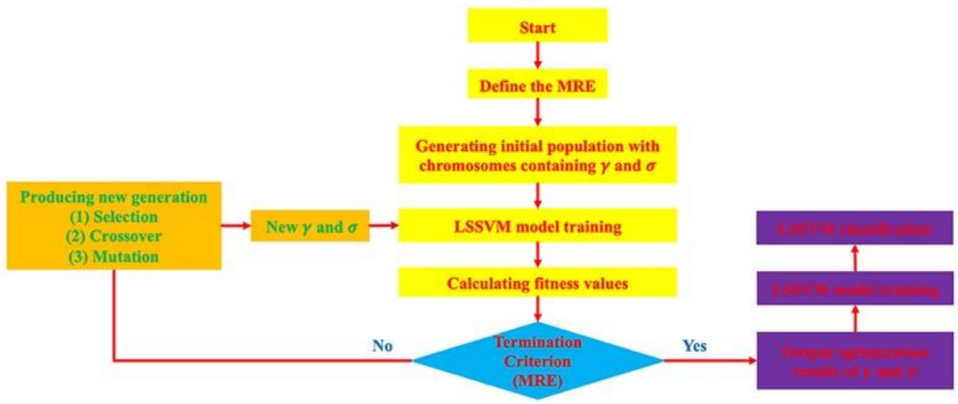

Fig. 4-9 Flow chart of GA-based LSSVM

Based on the above introduction, one can see that prudent selection of the penalty factor γ and Kernel bandwidth parameter σ^2 is necessary to achieve promising performance. Thus, the genetic algorithm [183, 184, 185] is used to optimize these two parameters. The flowchart of the GA-LSSVM is illustrated in Fig. 4-9, and the mean relative error (MRE) is used as the fitness function

$$MRE = \frac{1}{N} \sum_{i=1}^{N} \frac{|y_i - \hat{y}|}{y_i} \times 100\%, \tag{4-39}$$

where N is the sample size, and $\hat{y}$ is the prediction value.

To verify the effectiveness of the proposed MMFE-enhanced active sensing, the author conducts two experiments, as shown in Fig. 4-10 (a) and (b) [180]. Overall, the equipment consists of a digital torque wrench, a computer that installs the LabVIEW program for data sampling, an NI-DAQ system (NI USB-6363), a power amplifier (Trek 2100 HF), and two PZT patches (PZT A and PZT B). A swept sine wave with the range of 100-300 kHz (amplitude: 1 V, duration: 0.01 second) is generated by the NI-DAQ system and then amplified fiftyfold via the amplifier. This augmented signal is used to excite PZT A to emit stress waves, and these waves are received by PZT B (sampling rate: 1 MHz) after they propagate across the bolted interface. Moreover, two specimens are used: one is a three-bolt connection, and the other one is a four-bolt connection. For the three-bolt connection, two aluminum beams (size: 230 mm×40 mm×5 mm) are tightened by three M8 bolts. For the four-bolt connection, two steel plates (size: 150 mm×150 mm×5 mm) are tightened by four M8 bolts.

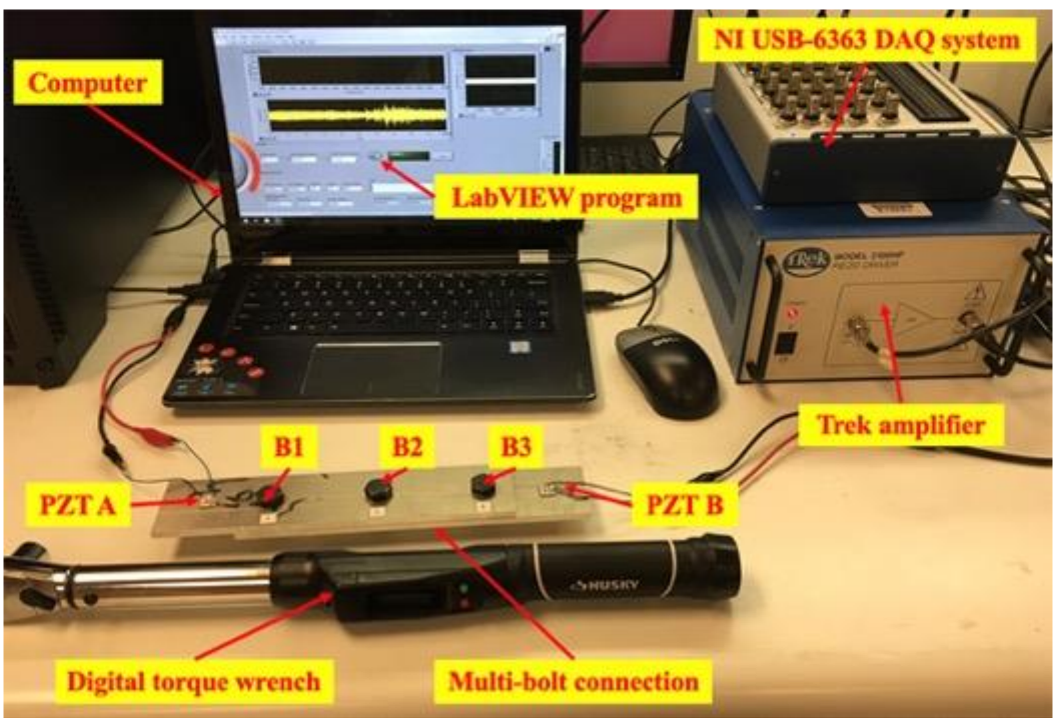

(a) specimen of three-bolt connection

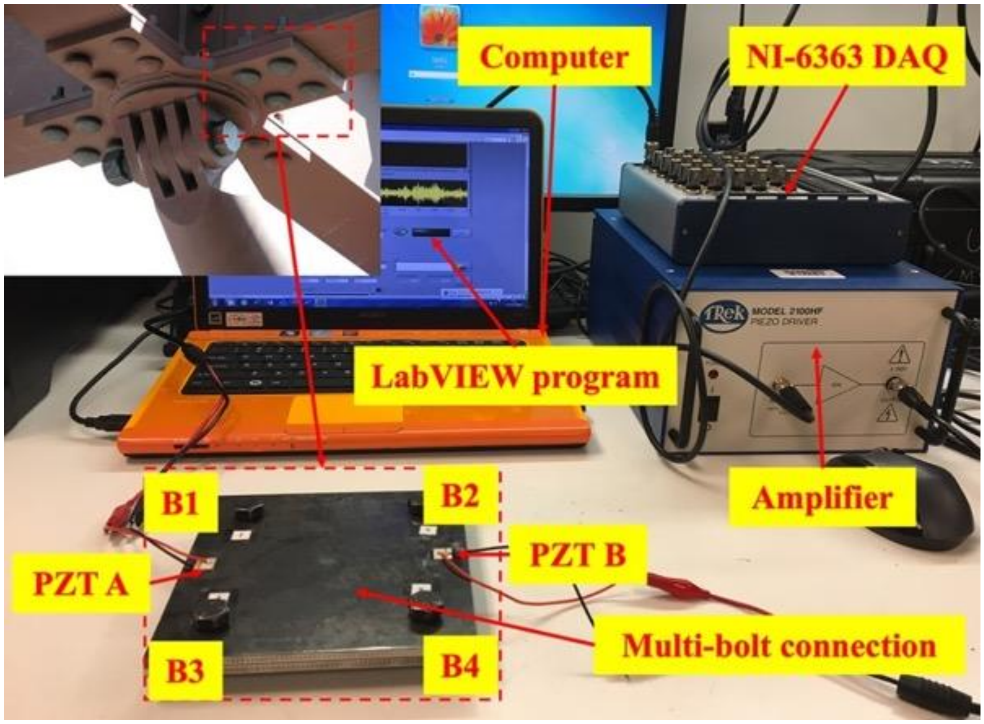

(b) specimen of four-bolt connection

Fig. 4-10 Experimental apparatus

For convenience, only two degrees of preload for each bolt are considered (i.e., fully tightened and loosen completely). Therefore, there are eight cases and 16 cases for the three-bolt connection and four-bolt connection, respectively. More details about the arrangement are given in Table 4-1 and Table 4-2. Here, B1, B2, B3, and B4 denote the bolt, and their detailed location in two specimens can be observed in Fig. 4-10 (a) and (b), respectively.

Table 4-1 Detailed arrangement of the experimental for three-bolt connection

Case	B1	B2	B3	Total number of training data	Total number of testing data
1	Loose	Loose	Loose	20	20
2	Tighten	Loose	Loose	20	20
3	Loose	Tighten	Loose	20	20
4	Loose	Loose	Tighten	20	20
5	Tighten	Tighten	Loose	20	20
6	Tighten	Loose	Tighten	20	20
7	Loose	Tighten	Tighten	20	20
8	Tighten	Tighten	Tighten	20	20

Table 4-2 Detailed arrangement of the experimental for four-bolt connection

Case	B1	B2	B3	B4	Total number of training data	Total number of testing data
1	Loose	Loose	Loose	Loose	20	20
2	Tighten	Loose	Loose	Loose	20	20
3	Tighten	Tighten	Loose	Loose	20	20
4	Tighten	Loose	Tighten	Loose	20	20
5	Tighten	Loose	Loose	Tighten	20	20
6	Tighten	Tighten	Tighten	Loose	20	20
7	Tighten	Loose	Tighten	Tighten	20	20
8	Tighten	Tighten	Loose	Tighten	20	20
9	Tighten	Tighten	Tighten	Tighten	20	20
10	Loose	Tighten	Loose	Loose	20	20
11	Loose	Tighten	Tighten	Loose	20	20
12	Loose	Tighten	Loose	Tighten	20	20
13	Loose	Tighten	Tighten	Tighten	20	20
14	Loose	Loose	Tighten	Loose	20	20
15	Loose	Loose	Tighten	Tighten	20	20
16	Loose	Loose	Loose	Tighten	20	20

For the three-bolt connection, the received signals and corresponding signal energy under different cases are depicted in Fig. 4-11, which reveals that difference of the signal energy under some cases are not obvious (e.g., Case 2, 5, 7, and 8). In other words, signal energy is incapable for multi-bolt looseness detection.

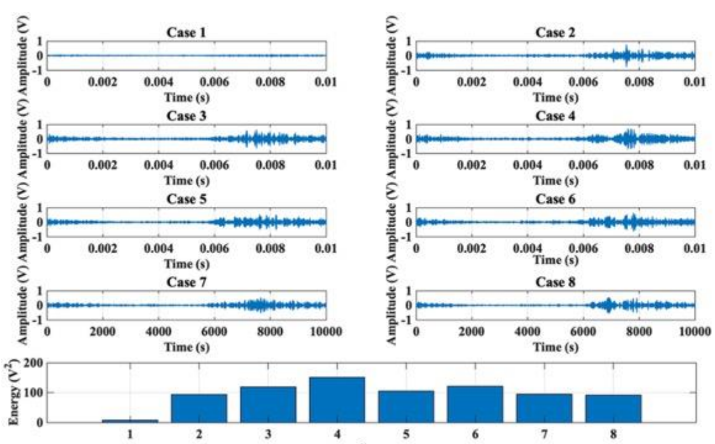

Fig. 4-11 Received signals and signal energy under different cases for three-bolt connection

Then, the MMFE values of the received signals under different cases are computed. Particularly, the scale factor τ of 20 are selected after the trial-and-error. Generally, small τ cannot reveal the complexity of signals adequately, and large τ will induce computation redundancy. The results are shown in Fig. 4-12. For each case, the computation of MMFE is repeated five times (via five received signals), and it can be observed that the MMFE results maintain a good consistency. That is to say, the MMFE has robustness, which is suitable for on-line monitoring. The only exception is Case 1, which can be explained that the complexity of signals under this case (all bolts are loosening) has great randomness.

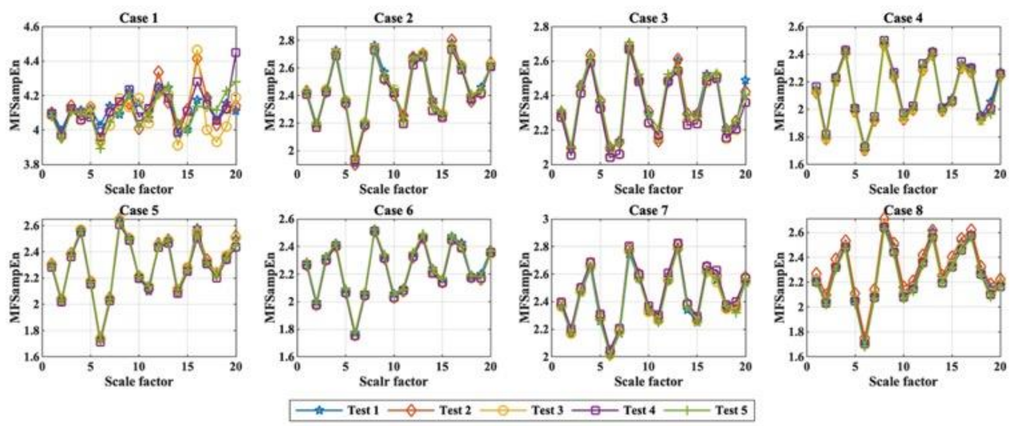

Fig. 4-12 MMFE values of received signals under different cases for three-bolt connection

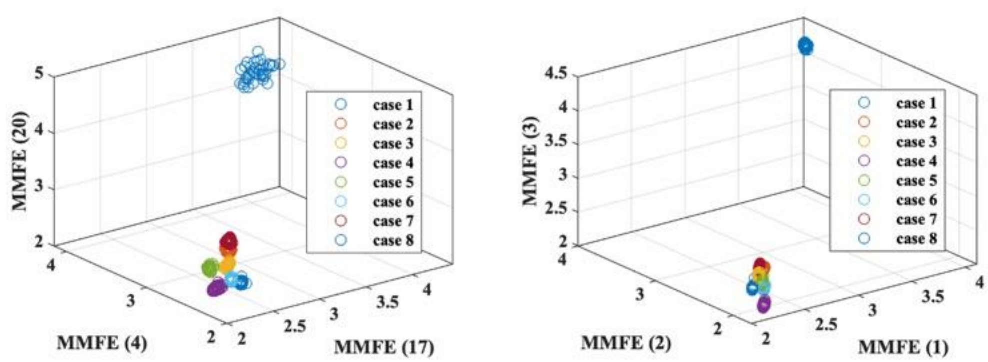

Fig. 4-13 Comparison between new feature sets and initial feature sets (left $\tau = 17, 4, 20$, right $\tau = 1, 2, 3$)

Using the mRMR algorithm, one can select the first four significant features from the MMFE results. For the three-bolt connection, the selected significant features are $\tau = 17, 4, 20, 13$. Moreover, to verify the effectiveness of the mRMR algorithm, the feature set of $\tau = 17, 4, 20$ and the feature set of $\tau = 1, 2, 3$ (which is randomly selected) are compared, and the results are plotted in Fig. 4-13, which shows that the feature set selected by the mRMR clusters around the center of each case, and there are obvious boundaries among different cases.

After selecting the first four significant features, the following training/testing dataset matrix and corresponding label matrix is performed,

$$T_j = \begin{bmatrix} MMFE_{\tau=17,1} & MMFE_{\tau=4,1} & MMFE_{\tau=20,1} & MMFE_{\tau=13,1} \\ MMFE_{\tau=17,2} & MMFE_{\tau=4,2} & MMFE_{\tau=20,2} & MMFE_{\tau=13,2} \\ \vdots & \vdots & \vdots & \vdots \\ MMFE_{\tau=17,i} & MMFE_{\tau=4,i} & MMFE_{\tau=20,i} & MMFE_{\tau=13,i} \end{bmatrix}; \quad L_j = \begin{bmatrix} l_1 \\ l_2 \\ \vdots \\ l_i \end{bmatrix}, \tag{4-40}$$

where $i = 1, 2, \cdots, 8$ denotes the case number, $j = 1, 2, \cdots, 20$ is the total number of training/testing dataset. Then, based on the training dataset, a GA-LSSVM classifier is trained, and the testing dataset is used to demonstrate the capacity (classification accuracy) of the classifier.

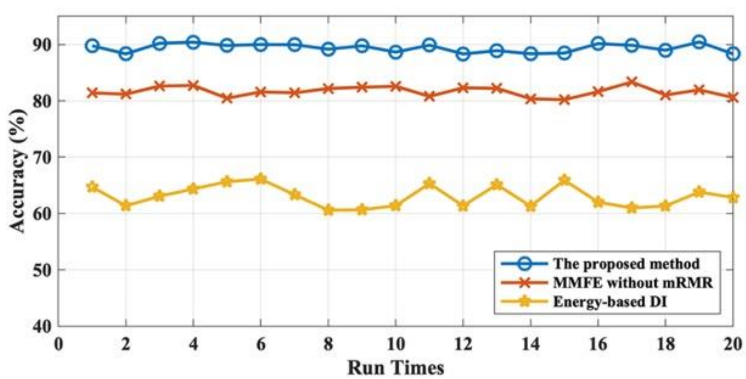

Fig. 4-14 Comparison of classification accuracy for three methods

As depicted in Fig. 4-14, repeated the training and testing twenty times to avoid the randomness. Notably, the author sets another two baseline systems, including traditional active sensing method (i.e., energy-based DI) and the proposed MMFE-enhanced active sensing without mRMR. All statistical results are summarized in Table 4-3, which shows that the proposed method can achieve the best performance.

Table 4-3 Classification accuracy of different methods

Method	Optimized model parameters		Accuracy (%)		
	γ	σ^2	Max	Min	Mean
The proposed method	20.8233	1.1355	90.44	88.33	89.39
MMFE without mRMR	5.6794	0.9929	83.34	80.20	81.65
Energy-based DI	12.5637	0.0448	66.11	60.58	63.06

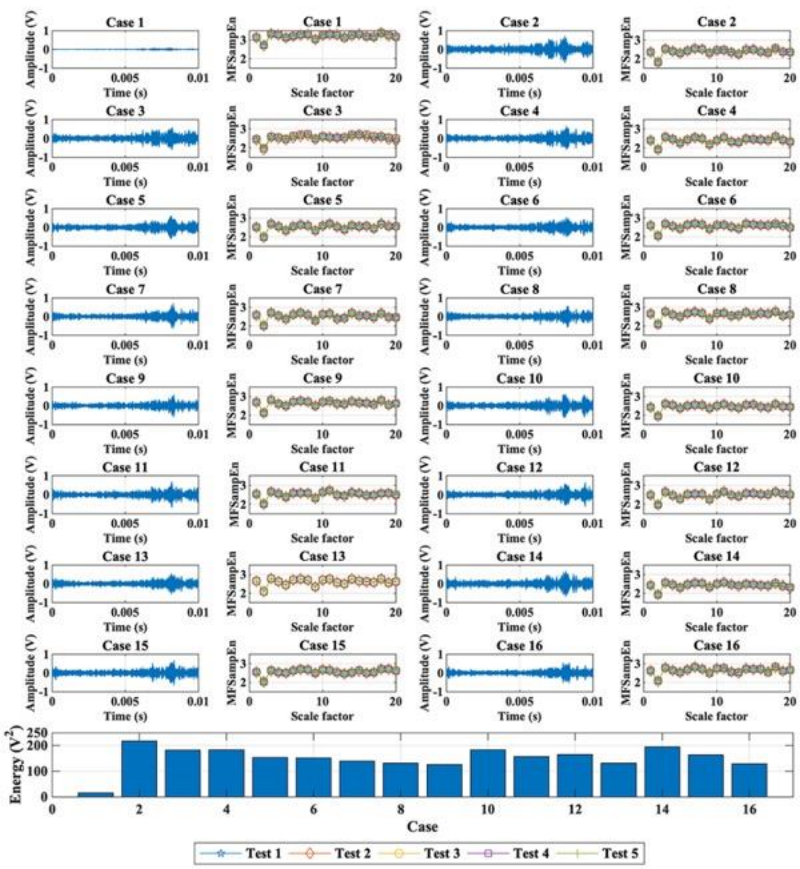

Fig. 4-15 Received signals with corresponding MMFE values under different cases for four-bolt connection

Similarly, the author implements the multi-bolt looseness detection for the four-bolt connection. The received signals, signal energy, and corresponding MMFE results are given in Fig. 4-15. Then, using the mRMR algorithm, the first four significant is determined as $\tau = 1, 17, 16, 4$. Fig. 4-16 demonstrates the effectiveness of the mRMR again. Finally, the classification results of three methods are compared in Fig. 4-17 and Table 4-4, which conforms the capacity of the proposed method.

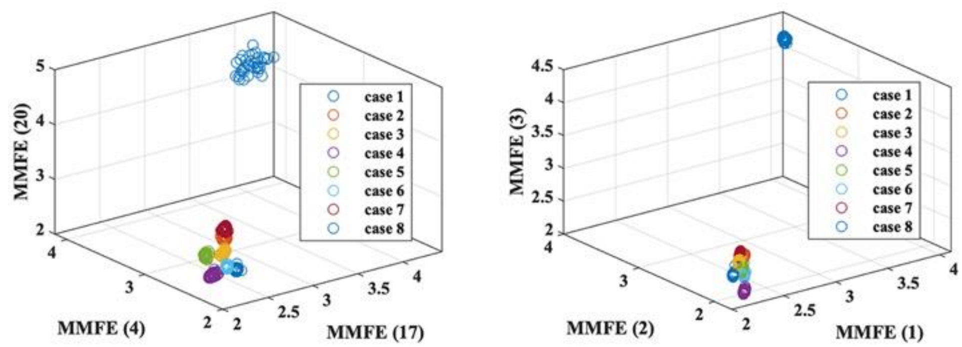

Fig. 4-16 Comparison between new feature sets and initial feature sets (left $\tau = 1, 17, 16$, right $\tau = 1, 2, 3$)

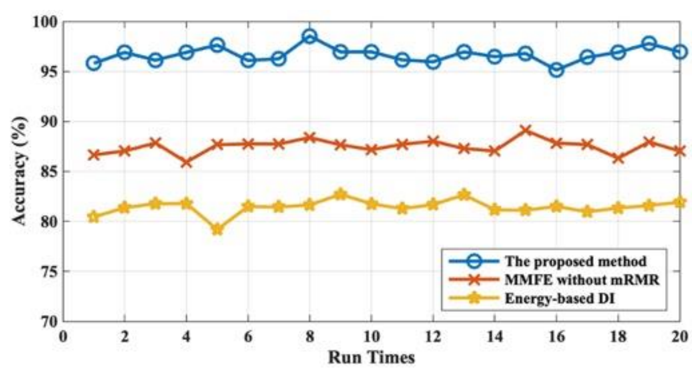

Fig. 4-17 Comparison of classification accuracy among three methods

Table 4-4 Classification accuracy among three methods

Method	Optimized model parameters		Accuracy (%)		
	γ	σ^2	Max	Min	Mean
The proposed method	5.2740	0.8021	98.55	95.14	96.69
MMFE without mRMR	1.0089	0.0038	89.10	85.93	87.49
Energy-based DI	3.4237	1.0354	82.71	79.19	81.44

4.4 Entropy-enhanced active sensing method for under water multi-bolt looseness detection

The past decades have seen the rapid development of the oil industry; particularly, more than one hundred million barrels of petroleum are produced every day to meet the requirements of global economy. It is worth noting that such a large-scale work is mainly achieved by using sprawling networks of pipelines, which are placed all over the world. For now, most oil pipelines are connected via the bolted flange, and we are facing severe challenges caused by bolt looseness in the flange connections. Particularly, compared to their counterparts on land, the subsea oil pipelines are more prone to losing enough preload, since the complex working conditions under the water can accelerate the procedure of creep and stress relaxation. Therefore, it is essential for us to develop reliable methods to detect underwater bolt looseness timely, while no related investigation has been performed before.

Recently, with the help of gripper and specific transducers, the Remote Operated Vehicles (ROVs) have been widely used to detect structural damages under the water [186, 187, 188]. For example, a low-cost ROV equipped with a gripper was designed by Manjunatha et al. [189] to inspect surface damages of subsea pipelines. Aggarwal et al. [190] developed a new tactile sensor that can be installed on the gripper of the ROV, thus improving the capacity of ROV for subsea tasks. Therefore, with the help of integrated grippers and specific transducers, we can expect the potential of ROV in detecting multi-bolt looseness of subsea flanges. For instance, as depicted in Fig. 4-18, if the ROV is equipped with grippers and PZT transducers, we may enable the ROV to implement the entropy-enhanced active sensing method to detect multi-bolt looseness. Therefore, this subsection presents a feasibility study to demonstrate the effectiveness of the above concept by designing a "Smart Crawfish" (i.e., a ROV equipped with a gripper and a pair of PZT transducers). Here, it is called the "Smart Crawfish" since the configuration of ROV with gripper is like a biological crawfish. Moreover, a new entropy-enhanced active sensing method is developed. After the "Smart Crawfish" grasps the bolted flange through the gripper, the entropy-enhanced active sensing method can be implemented via the PZT transducers to realize the multi-bolt looseness detection. More details are discussed as follows.

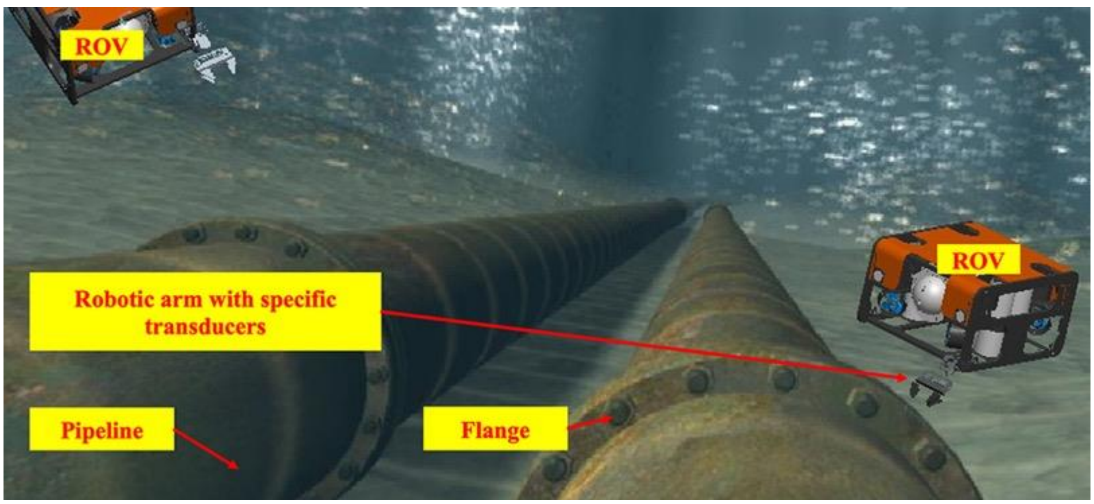

Fig. 4-18 Illustration of subsea multi-bolt looseness detection via the ROV

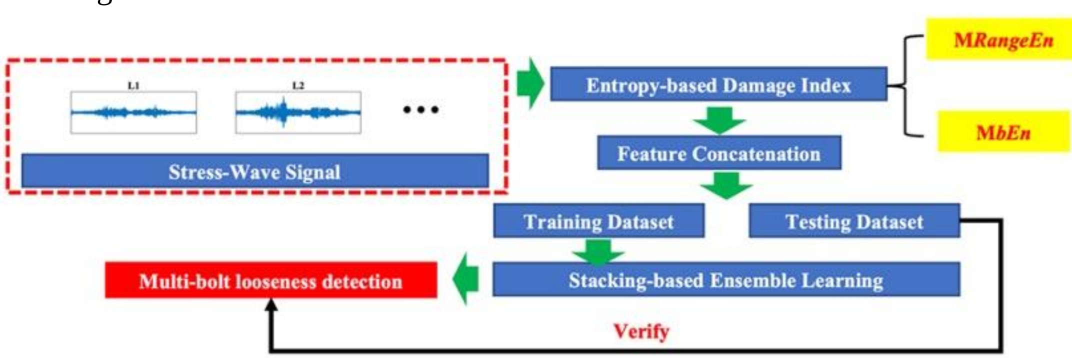

Fig. 4-19 Flowchart of the proposed multi-bolt looseness strategy

Fig. 4-19 illustrates the flowchart of the entire procedure of multi-bolt looseness. Stress wave signals under different cases of multi-bolt looseness can be obtained after the “Smart Crawfish” grasps the bolted flange and implements the active sensing. Then, a new entropy index that consists of two entropy methods (i.e., multiscale range entropy and multiscale bubble entropy) is developed to process the stress wave signals. Moreover, the training and testing datasets can be constructed. Finally, a stacking-based ensemble learning classifier is trained to identify different cases of multi-bolt looseness.

Overall, the multiscale range entropy (M*RangeEn*) is developed based on the range entropy [191], and its detailed computation procedure is described as follows.

(1) Given a time-series $\boldsymbol{x} = \{x(1), \cdots, x(i), \cdots, x(N)\}$, one first can implement the coarse-grained time-series $\boldsymbol{y}^{(\tau)}$ as

$$y^{(\tau)}(j) = \frac{1}{\tau} \sum_{i=(j-1)\tau+1}^{j\tau} x(i), \quad 1 \le j \le N/\tau, \tag{4-40}$$

where τ is the scale factor.

(2) Subsequently, one can map $\boldsymbol{y}^{(\tau)}$ into several spaces with m dimension as

$$\boldsymbol{Y}_m^{(\tau)}(1), \cdots, \boldsymbol{Y}_m^{(\tau)}(l), \cdots, \boldsymbol{Y}_m^{(\tau)}(N/\tau - m + 1), \tag{4-41}$$

where $\boldsymbol{Y}_m^{(\tau)}(l) = \{y^{(\tau)}(l), y^{(\tau)}(l+1), \cdots, y^{(\tau)}(l+m-1)\}$.

(3) A criterion [191] can be defined as

$$d_{range}(\boldsymbol{Y}_m^{(\tau)}(l), \boldsymbol{Y}_m^{(\tau)}(k)) = \frac{\max\limits_n \left| y^{(\tau)}(l+n) - y^{(\tau)}(k+n) \right| - \min\limits_n \left| y^{(\tau)}(l+n) - y^{(\tau)}(k+n) \right|}{\max\limits_n \left| y^{(\tau)}(l+n) - y^{(\tau)}(k+n) \right| + \min\limits_n \left| y^{(\tau)}(l+n) - y^{(\tau)}(k+n) \right|} \le r,$$
$$1 \le k \le N/\tau - m; k \ne l; 0 \le n \le m-1 \tag{4-42}$$

where r is the tolerance, which can be calculated via the standard deviation std of x, and r is within the range of $(0.1 \times std, 0.25 \times std)$.

Then, the total numbers of $\boldsymbol{Y}_m^{(\tau)}(l)$ that satisfy the above criterion can be obtained as $B_l^m(r)$.

(4) The average of $B^m(r)$ can be calculated as

$$B^m(r) = \frac{1}{N/\tau - m} \sum_{l=1}^{N/\tau - m} B_l^m(r) . \tag{4-43}$$

Similarly, after increasing the dimension from m to $m+1$ and repeating Steps (3-4), one can get $B_l^{m+1}(r)$.

(5) Finally, the M*RangeEn* can be expressed as

$$MRangeEn = -\ln\left[B^{m+1}(r) / B^m(r) \right] . \tag{4-44}$$

Similarly, the multi bubble entropy (M*bEn*) can be calculated based on the bubble entropy [192], and detailed procedure is introduced as follows.

(1) Given a $\boldsymbol{x} = \{x(1), \cdots, x(i), \cdots, x(N)\}$, one can construct the coarse-grained time-series $\boldsymbol{y}^{(\tau)}$ and map it into a series of spaces $\boldsymbol{Y}_m^{(\tau)}(1), \cdots, \boldsymbol{Y}_m^{(\tau)}(l), \cdots, \boldsymbol{Y}_m^{(\tau)}(N/\tau - m + 1)$ with dimension m.

(2) The bubble sorting algorithm is employed to sort each $\boldsymbol{Y}_m^{(\tau)}(l)$ in ascending order, and the total number n_i of necessary swaps can be counted. Then, the entropy H^m can be calculated as follows

$$H^m = -\log \sum_{i=1}^{n} p_i^2 , \tag{4-45}$$

where p_i is the probabilities of n_i, and it can be obtained by histogram.

(3) After increasing m to $m+1$, one can compute H^{m+1} and obtain the M*bEn* as

$$\mathrm{M}bEn = (H^{m+1} - H^{m}) \Big/ \log(m+1 \big/ m-1) \,. \tag{4-46}$$

To verify the effectiveness of the proposed M*RangeEn* and M*bEn*, two tests (i.e., stability test and discriminating power test) are performed. For the stability test, two kinds of synthetic signals (including the Gaussian noise and pink noise) with different lengths (signal length= 10,000; 30,000; and 50,000) are used. Parameters m and r in M*RangeEn* are set to 2 and 0.2, and parameter m in M*bEn* is set to 6. Moreover, the maximum scale factor τ is set to 10. The results are depicted in Fig. 4-20, which shows that signal length has little effect on both M*RangeEn* and M*bEn*. In other words, the proposed M*RangeEn* and M*bEn* have great stability.

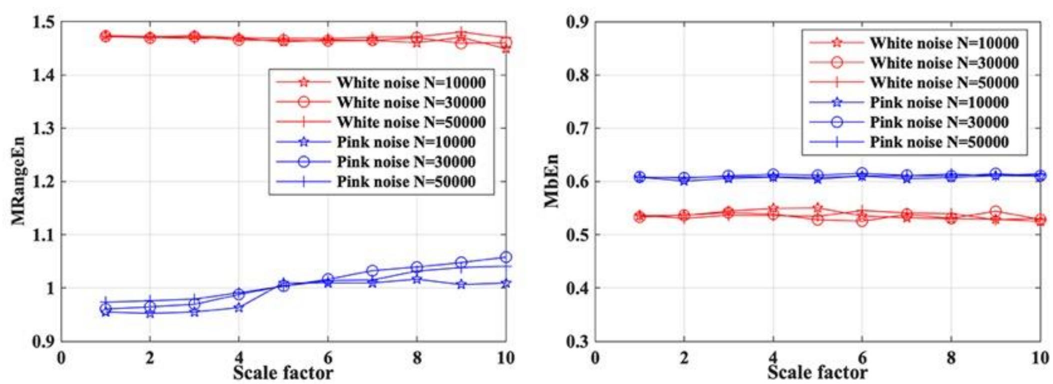

Fig. 4-20 Stability of M*RangeEn* and M*bEn* over different signal lengths

In terms of the test of discriminating power, a widely used dataset, i.e., the Rolling Bearing Data Center of Case Western Reverse University [193] is employed. Particularly, five different cases are selected, including the normal condition and four abnormal conditions with inner bearing faults. The sizes of inner faults are 0.007 inch, 0.014 inch, 0.021 inch, and 0.028 inch, respectively. All signals are collected at driving end bearing of the motor with a sampling rate of 12 kHz, and the motor speed is 1,797 rpm. The signal length is set to 50, 000, and the results are indicated as M*RangeEn* and

M*bEn* in Fig. 4-21. Overall, the differences among five cases are obvious, which demonstrates the discriminating power of M*RangeEn* and M*bEn*.

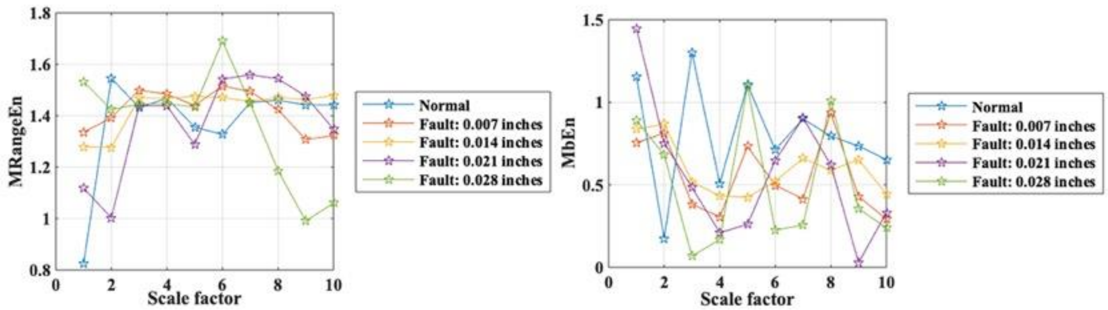

Fig. 4-21 Discriminating power of M*RangeEn* and M*bEn*

In the last subchapter, the GA-LSSVM is used to classify the entropy-based indexes under different cases. However, a deficiency is that one single classifier may not implement the classification adequately due to the existence of variance and noise in data. Therefore, the ensemble learning [194] is developed, and the core concept is to train multiple classifiers (which are always called as base learners) can combine them to achieve the final classification. Generally, the base learners consist of support vector machine (SVM) [195], logistic regression (LR) [196], k-nearest neighbor (KNN) [197], and naïve Bayes (NB) [198], etc. That is to say, the ensemble learning can be regarded as a family of classification algorithms, and thus the generalization ability can be ensured [199, 200, 201, 202]. Overall, the ensemble learning can be divided to three categories: boosting, bagging, and stacking [203]. The weight distribution of base learners in boosting ensemble learning are updated each iteration, and the final classification is achieved via the combination of base learners (notably, the combination strategy is according to weights). On the other hand, the bagging ensemble learning method trains each base learner by using the Bootstrap sampling, and the major base learner is employed to accomplish the classification. Different from the boosting and bagging ensemble learning, the concept of stacking-based ensemble learning is to train a meta-classifier based on base learners (particularly, several boosting and bagging ensemble learning algorithm can be used as base learners in stacking-based ensemble learning, e.g., random forest [204]).

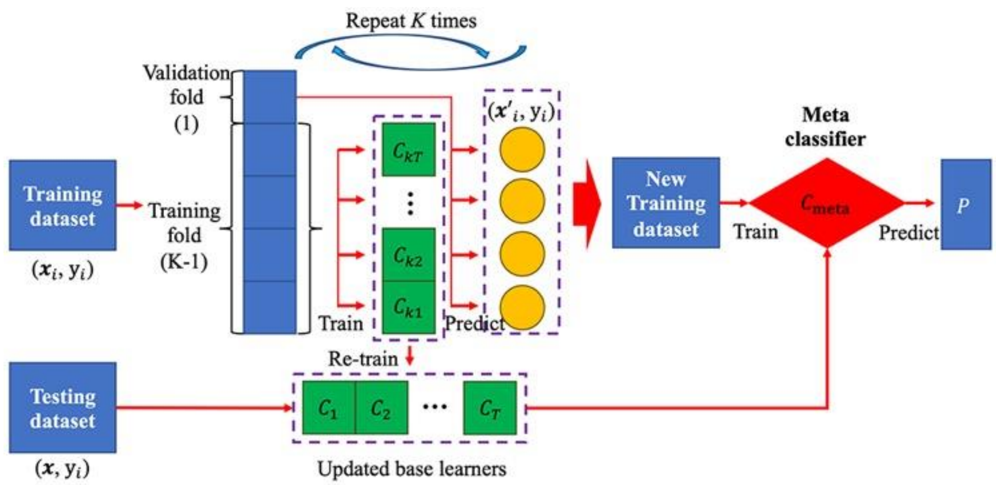

Fig. 4-22 Flowchart of the stacking-based ensemble learning

According to Fig. 4-22, one can accomplish the stacking-based ensemble learning as follows [203]:

(1) Given a training dataset $D_{train} = \left\{\boldsymbol{x}_i, y_i\right\}_{i=1}^{m} (\boldsymbol{x}_i \in \mathbb{R}^n, y_i \in y)$, one can divide it to K subsets. $K-1$ subsets are used to train the base learners C_{kt}, where $k = 1, 2, \cdots K$ and $t = 1, 2, \cdots T$ (T is the total numbers of base learners). Then, the output $\left\{\boldsymbol{x}_i', y_i\right\}$ ($\boldsymbol{x}'_i = \{C_{k1}(\boldsymbol{x}_i), C_{k2}(\boldsymbol{x}_i), \cdots, C_{kT}(\boldsymbol{x}_i)\}$) can be obtained by applying C_{kt} to the remaining subset.

(2) The output of all base learners can be obtained by repeating Step (1) K times, and then a new training dataset is constructed by combining all outputs. This new training dataset is employed to train the meta-classifier C_{meta}. It is worth noting that this procedure is similar to that in the K-fold cross validation. The reason of using

this K-fold cross strategy is that over-fitting can be effectively avoided since the training datasets for C_{kt} and C_{meta} are different.

(3) After the meta-classifier is trained, we can retrain the new base learners C_t via the entire training dataset D_{train}. Finally, the predicted label of the testing sample x, which is from the testing dataset, can be obtained as $C_{meta}(C_1(\boldsymbol{x}), C_2(\boldsymbol{x}), \cdots, C_T(\boldsymbol{x}))$.

To verify the effectiveness of the proposed underwater multi-bolt looseness detection via the proposed entropy-enhanced active sensing method and the stacking-based ensemble learning classifier, the author designs a prototype of the "Smart Crawfish" and conducts a lab-level test. As shown in Fig. 4-23, the "Smart Crawfish" consists of a ROV, a gripper, two chambers for buoyancy balancing, and two PZT transducers (PZT A and B). A direct-current (DC) power supply is used to actuate the gripper to grasp the flange, which is tightened by four M4 bolts (which, for convenience, are denoted as B1, B2, B3, and B4). Particularly, to simulate the condition under the sea, the "Smart Crawfish" and the flange are placed in a glass jar with sea water. A swept sine wave (frequency range: 20 kHz-150 kHz, duration: 0.1 second; amplitude: 10 V) is generated by an NI multifunctional DAQ system (NI USB 6363) to actuate PZT A to produce stress wave signals. Then, PZT B is employed to receive the stress wave signals (sampling rate: 500 kHz) after they propagate across the bolted interface. The received stress wave signals are converted to digital signals via the NI DAQ system and saved in a computer that has a customized LabVIEW program.

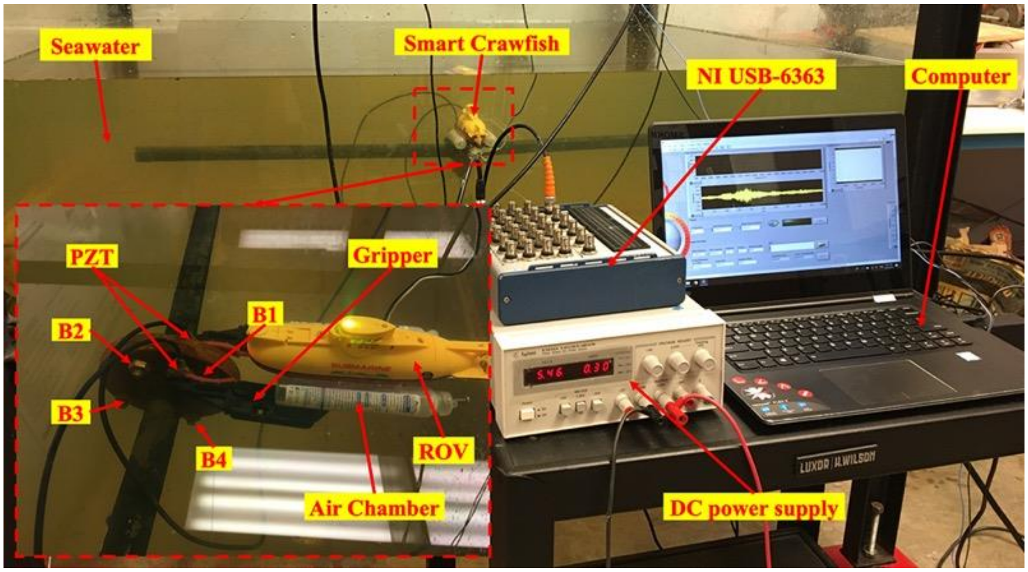

Fig. 4-23 Experimental apparatus

In this subsection, six different cases of multi-bolt looseness are considered, whose detail is given in Table 4-5. Notably, for each bolt, only two states (fully tightened and loosening completely) are considered. Under each case, the active sensing is repeated 100 times. In other words, there are a total of 600 samples to construct the training dataset and testing dataset, respectively. The ratio of training dataset to testing dataset is 4:1 (i.e., 480 training samples and 120 testing samples). Finally, a stacking-based ensemble learning classifier will be trained via the training dataset, and its capacity can be verified by using the testing dataset.

Table 4-5 Detailed arrangement of six classes

Case	B1	B2	B3	B4
1	Loose	Loose	Loose	Loose
2	Tighten	Loose	Loose	Loose
3	Tighten	Loose	Tighten	Loose
4	Tighten	Tighten	Loose	Loose
5	Tighten	Tighten	Loose	Tighten
6	Tighten	Tighten	Tighten	Tighten

The received signals under six different cases and corresponding energy are illustrated in Fig. 4-24. Similar to earlier discussion in Chapter 4.3, one can see that the signal is not a good index/indicator for multi-bolt looseness.

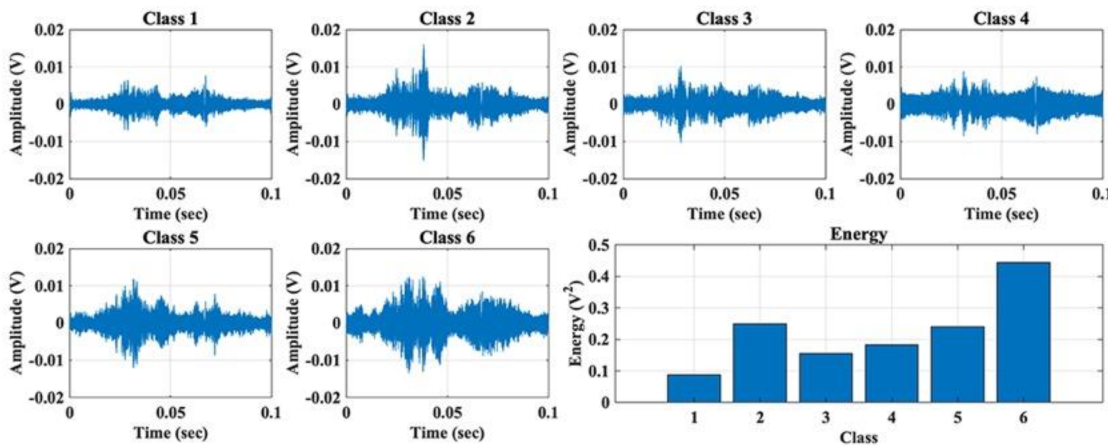

Fig. 4-24 Received stress wave signals under six different classes and corresponding signal energy

The M*RangeEn* and M*bEn* values of received stress wave signals under different classes are shown in Fig. 4-25. The parameters m and r of the M*RangeEn* are set to 2 and 0.2, and m of M*bEn* is set to 6. Moreover, the scale factor τ is set to 10. Then, the feature vectors of M*RangeEn* and M*bEn* are concatenated to build the training dataset and testing dataset (i.e., the dimension of features are 20).

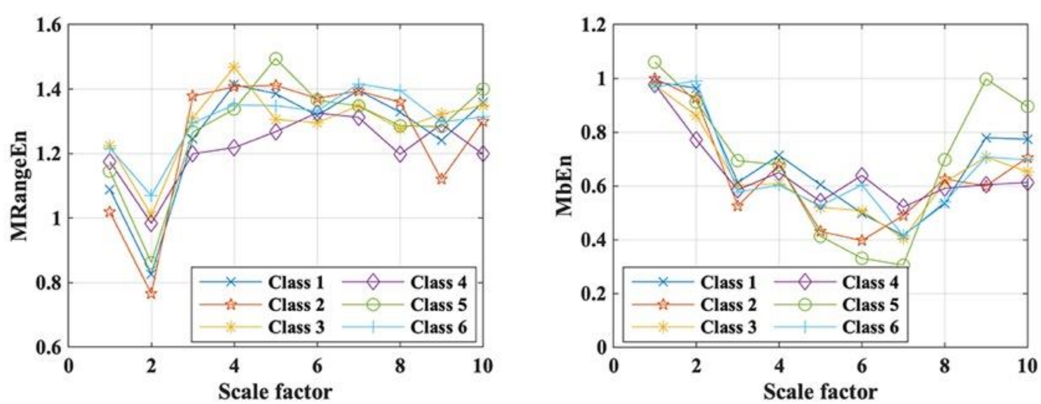

Fig. 4-25 M*RangeEn* and M*bEn* values of received stress wave signals under different classes

Finally, a stacking-based ensemble learning classifier is trained with three base learners (including the random forest, the Gaussian NB, and the KNN), and the meta-classifier is SVM. Additionally, the times of repetition (i.e., K) are set to 10. Particularly, the performance between the method proposed in this subsection and previous investigation (in Chapter 4.3) is compared. The confusion matrix of two methods are given in Fig. 4-26, and the classification accuracy is summarized in Table 4-6, which demonstrates that the proposed method is capable of underwater multi-bolt looseness detection, which has good potential for future applications.

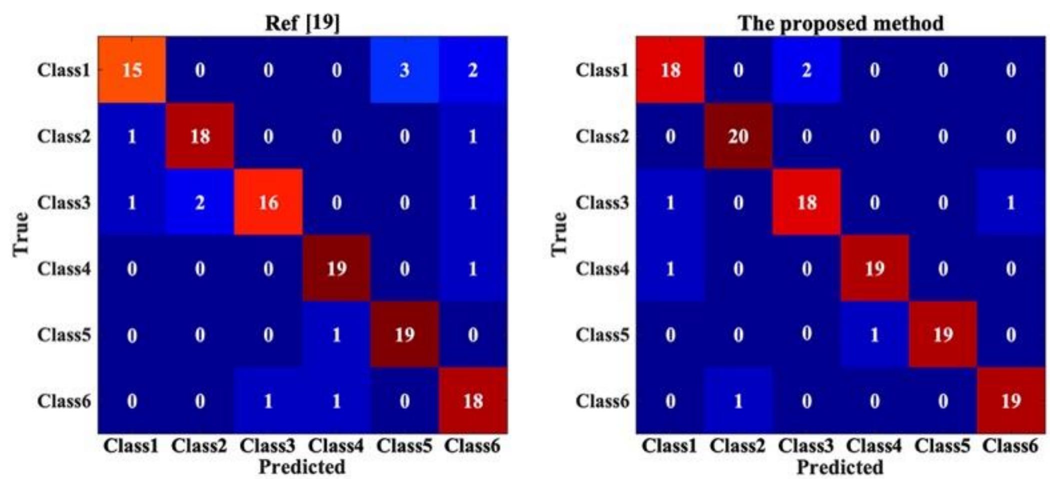

Fig. 4-26 Classification results (confusion matrix) of the proposed method and previous investigation

Table 4-6 Comparison of classification performance between two methods

Method	Accuracy (%)
Previous method	87.50
The proposed method	**94.17**

CHAPTER 5. MODELING OF ELECTROMECHANICAL IMPEDANCE METHOD FOR BOLT LOOSENESS DETECTION

This chapter presents an analytical modeling of the EMI method for bolt looseness detection, based on the fractal contact theory. Overall, the EMI method is an effective SHM methods for multiple structures, including composite materials [206], aircraft components [207], gas pipelines [208], fatigue cracks [209], pin connection [210], truss structures [211], and concrete structures [212]. Particularly, the EMI method has shown promising performance for bolt looseness monitoring [24, 25, 26, 213, 214, 215]. However, it should notice that all above investigations depend on qualitative detection, and no analytical modeling of EMI for specific structures has been provided.

On the other hand, several researchers have attempted to build analytical models of the EMI method for detecting some simple structures, such as 1D structures (beam) [216, 217, 218, 223, 224], 2D structures (plate) [21, 219, 220, 221, 225], and 3D structures (cube and cylindrical shell) [22, 222, 226, 227]. Notably, Bhalla et al. [21, 221] developed the concept of "effective impedance" to precisely characterize the electromechanical interaction between the PZT transducer and the structures. Therefore, inspired by Bhalla's investigation, the author developed the EMI model of bolted joint.

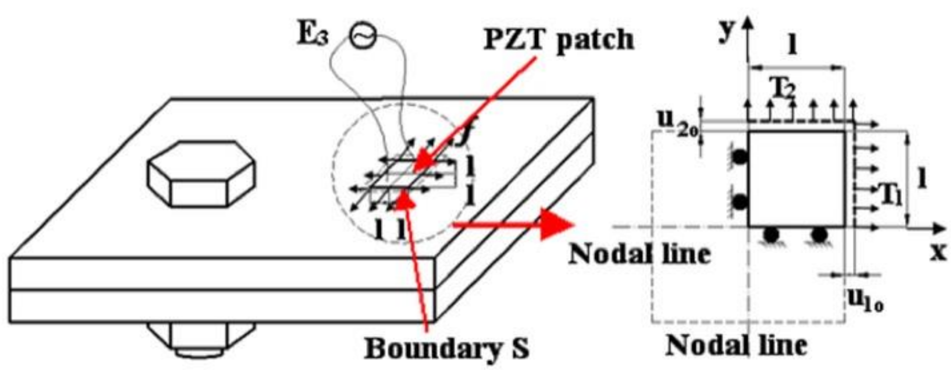

Fig. 5-1 stresses/displacements on PZT patch installed on the bolted joint

As depicted in Fig. 5-1 [239], a harmonic electric field (an angular frequency of ω) is applied to a bolted joint. Due to symmetry (i.e., nodal lines are also symmetrical axes), one can investigate the relationship between PZT and bolted connection by only regrading 1/4 of the patch. According to previous investigation [21], three assumptions are made:

(1) To ignore the mass and stiffness of the PZT patch, consider the PZT patch as an infinitesimal object,

(2) The influence of vibration of the PZT patch (along the thickness direction) is neglected,

(3) The force from the PZT to the bolted connection is transmitted via all boundaries.

Then, the "effective mechanical impedance" of the PZT patch [21] can be given as

$$Z_{a,eff} = \frac{\oint_s f \cdot \hat{n} ds}{\dot{u}_{eff}} = \frac{F}{\dot{u}_{eff}}, \tag{5-1}$$

where l is half length of the PZT patch, f is the boundary traction per unit length (please note that $\oint_s f ds = 0$ since entire force is equilibrium). Moreover, F represents the planar force, which is the reason of area deformation of the PZT patch, $\hat{n}$ is the unit vector along the direction that is normal to the boundary, $u_{eff} = \delta A / p_o$ is the "effective displacement" of the patch, δA is the area change of the PZT patch, p_o denotes the total length of the patch.

The constitutive function [230] of piezoelectric materials can be expressed as

$$\begin{bmatrix} D \\ S \end{bmatrix} = \begin{bmatrix} \overline{\varepsilon^T} & d^d \\ d^c & \overline{s^E} \end{bmatrix} \begin{bmatrix} E \\ T \end{bmatrix}, \tag{5-2}$$

where $D(3\times 1)$ (C/m^2) is the vector of electric displacement, $S(6\times 1)$ is the strain vector, $E(3\times 1)$ (V/m) is the vector of applied external electric field, $T(6\times 1)$ (N/m^2) is the stress vector, $\overline{\varepsilon_{ij}^T} = \varepsilon_{ij}^T(1-\delta j)(3\times 3)$ is the complex dielectric permittivity matrix under constant stress, $\overline{s_{km}^E} = s_{km}^E(1-\eta j)(6\times 6)$ is the complex elastic compliance matrix under constant electric field, $d_{im}^d(3\times 6), d_{jk}^c(6\times 3)$ are the piezoelectric strain coefficients matrices, δ is the dielectric loss factor, and η is the mechanical loss factor.

The assumption that the PZT patch has mechanical and piezoelectrical isotropic in x-y plane simplifies eqn. (5-2) as

$$\begin{aligned} D_3 &= \overline{\varepsilon_{33}^T}E_3 + d_{31}(T_1+T_2) \\ S_1 &= \frac{T_1 - vT_2}{\overline{Y^E}} + d_{31}E_3 \quad , \\ S_2 &= \frac{T_2 - vT_1}{\overline{Y^E}} + d_{31}E_3 \end{aligned} \tag{5-3}$$

where υ is the material's Poisson ratio, $\overline{Y^E}=Y^E(1+\eta j)$ is the complex Young's modulus in a constant electric field. Subsequently, via algebraical transform, we can obtain

$$T_1 + T_2 = \frac{\left(S_1 + S_2 - 2d_{31}E_3\right)\overline{Y^E}}{1-v}. \tag{5-4}$$

Equation (5-4) can be rewritten when the PZT patch is in a zero-electric field

$$(T_1+T_2)_{short-circuited} = \frac{\left(S_1+S_2\right)\overline{Y^E}}{1-v}. \tag{5-5}$$

The displacement of PZT patch [20] in x and y directions can be expressed as

$$\begin{cases} u_1 = (A_1 \sin\kappa x)e^{j\omega t} \\ u_2 = (A_2 \sin\kappa y)e^{j\omega t} \end{cases}, \tag{5-6}$$

where A_1, A_2 are coefficients that can be calculated through boundary conditions, $\kappa = \omega\sqrt{\rho\left(1-v^2\right)/\overline{Y^E}}$ is the wave number. Differentiating eqn. (5-6) gives the velocities and strains of the PZT patch as

$$\begin{cases} \dot{u}_1 = \dfrac{\partial u_1}{\partial t} = (A_1 j\omega \sin\kappa x)e^{j\omega t} \\ \dot{u}_2 = \dfrac{\partial u_2}{\partial t} = (A_2 j\omega \sin\kappa y)e^{j\omega t} \\ S_1 = \dfrac{\partial u_1}{\partial x} = (A_1 \kappa \cos\kappa x)e^{j\omega t} \\ S_2 = \dfrac{\partial u_2}{\partial y} = (A_2 \kappa \cos\kappa y)e^{j\omega t} \end{cases}. \tag{5-7}$$

Substituting eqn. (5-5) and (5-7) into eqn. (5-1) achieves the following "effective impedance"

$$Z_{a,eff} = \frac{\left(T_{1(x=l)}lh + T_{2(y=l)}lh\right)_{short\text{-}circuited}}{\left(\dfrac{\dot{u}_{1(x=l)} + \dot{u}_{2(y=l)}}{2}\right)} = \frac{2\kappa lh\overline{Y^E}}{j\omega(\tan\kappa l)(1\text{-}v)}, \tag{5-8}$$

where h is thickness of PZT patch. Then, the entire force F [21] can be obtained as

$$F = \oint_s f \cdot \hat{n}ds = T_{1(x=l)}lh + T_{2(y=l)}lh = \text{-}Z_{s,eff}\dot{u}_{eff} = \text{-}Z_{s,eff}\left(\frac{\dot{u}_{1(x=l)} + \dot{u}_{2(y=l)}}{2}\right). \tag{5-9}$$

Substituting eqn. (5-4) and (5-7) into eqn. (5-9) results in the following relationship

$$A_1 + A_2 = \frac{2d_{31}V_o Z_{a,eff}}{(\cos\kappa l)kh(Z_{s,eff} + Z_{a,eff})}. \tag{5-10}$$

Finally, via eqn. (5-3), (5-4), (5-7), and (5-10), the admittance $\bar{Y}$ (i.e., reciprocal of the impedance) can be expressed as

$$\bar{Y}=\frac{\bar{I}}{\bar{V}}=\frac{j\omega\iint_{A_1+A_2}D_3dxdy}{\bar{V}}=4\omega j\frac{l^2}{h}\left[\overline{\varepsilon_{33}^T}-\frac{2d_{31}^2\overline{Y^E}}{(1-\nu)}+\frac{2d_{31}^2\overline{Y^E}Z_{a,eff}}{(1-\nu)(Z_{s,eff}+Z_{a,eff})}\left(\frac{\tan\kappa l}{\kappa l}\right)\right],(5\text{-}11)$$

where $\bar{I}$ denotes the electric current, $\bar{V}=V_oe^{j\omega t}$ is the voltage applied to the PZT patch. Notably, the mechanical impedance $Z_{s,eff}$ of the bolted joint is the only unknown parameter in eqn. (5-11), and its computation method will be given later.

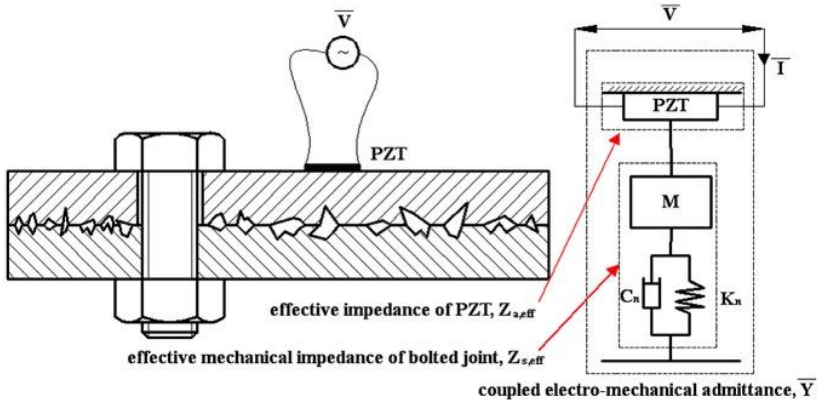

Fig. 5-2 Bolted joint bonded with PZT and its equivalent dynamic model

Overall, as shown in Fig. 5-2, the bolted connection can be equivalent to a mass-spring-damper system, due to the existence of surface roughness (i.e., micro asperities). According to previous investigation [231], the mechanical impedance $Z_{s,eff}$ of a mass-spring-damper system can be described as

$$\begin{cases} Z_{s,eff}\ real\ part=\dfrac{Cm^2\omega^2}{C^2+(\omega m-K/\omega)^2} \\ Z_{s,eff}\ imaginary\ part=\dfrac{m\omega\left[C^2-\dfrac{K}{\omega}(\omega m-K/\omega)\right]}{C^2+(\omega m-K/\omega)^2} \end{cases}, \tag{5-12}$$

where m, C and K are the mass, damping coefficient, and stiffness of the mechanical system. The interfacial damping and stiffness of bolted joint can be modeled by using the fractal contact theory [82] to take the imperfect interface into account as follows.

(1) Based on the Hertz contact theory [101], one can develop the relationship between the deformation δ of the asperity and the load as

$$\begin{cases} elastic\ deformation\ stage \quad P_e = \frac{4}{3}E^* R^{1/2}\delta^{3/2} \quad \delta \le \delta_c \\ plastic\ deformation\ stage \quad P_p = 2H\pi R\delta \quad \delta \ge \delta_c \end{cases}, \tag{5-13}$$

where P_e and P_p are the normal contact load in elastic and plastic deformation stages, respectively. Moreover, R is asperity radius, $\delta_c = \left(\frac{\pi H}{2E^*}\right)^2 R$ is critical deformation of asperity, $E^* = \left[\left(1-\upsilon_1^2\right)/E_1 + \left(1-\upsilon_2^2\right)/E_2\right]^{-1}$ is the equivalent elasticity modulus, E_1 and E_2 are elasticity modulus; υ_1 and υ_2 are the Poisson's ratio; $H = 2.8\sigma_s$ [232] is the hardness of the material; and σ_s is the yield strength of the material. Moreover, δ and R can be calculated as [67]

$$\delta = G^{D-1}a^{\frac{2-D}{2}}; R = \frac{a^{D/2}}{2\pi G^{D-1}}, \tag{5-14}$$

where a is the truncated area of asperity; D is the fractal dimension, G is the scaling constant. Then, when $\delta = \delta_c$, the critical truncated area a_c of asperity can be expressed as

$$a_c = G^2\left(\frac{2E^*}{H}\right)^{2/(D-1)}. \tag{5-15}$$

Particularly, the relationship [233] between load and a can be described as

$$\begin{cases} elastic\ deformation\ stage \quad P_e = \frac{4}{3\sqrt{2\pi}}E^* G^{D-1} a^{\frac{3-D}{2}} \quad a \ge a_c \\ plastic\ deformation\ stage \quad P_p = Ha \quad a \le a_c \end{cases}. \tag{5-16}$$

(2) The distribution function [85] of asperities on bolted contact interface can be expressed as

$$n(a)=\frac{D}{2}\psi^{(2-D)/2}a^{D/2}a^{-(D+2)/2} \quad 0<a\le a_l\,, \tag{5-17}$$

where a_l is the truncated area of the largest asperity; ψ is the domain extension factor. Moreover, the relationship between normalized bolt preload P^* and the real contact area A_r can be computed as

$$\begin{cases} P^*=\dfrac{P}{E^*A_a}=\dfrac{\int_0^{a_c}n(a)P_p(a)da+\int_{a_c}^{a_l}n(a)P_e(a)da}{E^*A_a} \\ \quad =\dfrac{1}{3\sqrt{\pi}}G^{*(D-1)}g_1(D)\psi^{\frac{2-D}{2}}A_r^{*\frac{D}{2}}\left[\psi^{\frac{-D^2+7D-6}{4}}(\dfrac{2-D}{D})^{\frac{3-2D}{2}}A_r^{*\frac{3-2D}{2}}-a_c^{*\frac{3-2D}{2}}\right]+ \\ \quad 2.8\varphi g_2(D)\psi^{(\frac{2-D}{2})^2}A_r^{*\frac{D}{2}}a_c^{*\frac{2-D}{2}} \qquad (D\ne1.5) \\ P^*=\dfrac{2^{\frac{1}{4}}}{\sqrt{\pi}}G^{*\frac{1}{2}}\psi^{\frac{1}{16}}(\dfrac{A_r^*}{3})^{\frac{3}{4}}\ln(\dfrac{A_r^*}{3\psi^{\frac{1}{4}}a_c^*})+8.4\varphi\psi^{\frac{1}{16}}(\dfrac{A_r^*}{3})^{\frac{3}{4}}a_c^{*\frac{1}{4}} \qquad (D=1.5) \end{cases}, \tag{5-18}$$

where A_a is the nominal contact area; $G^*=\dfrac{G}{\sqrt{A_a}}$ $\quad A_r^*=\dfrac{A_r}{A_a}$ $\quad a_c^*=\dfrac{a_c}{A_a}$ $\quad \varphi=\dfrac{\sigma_s}{E^*}$;

$g_1(D)=2^{\frac{6-D}{2}}(\dfrac{2-D}{D})^{\frac{D}{2}}\dfrac{D}{3-2D}$; $g_2(D)=(\dfrac{D}{2-D})^{\frac{2-D}{2}}$.

Then, the relationship between the normalized interfacial stiffness K_n^* and the real contact area A_r can be expressed as

$$\begin{cases} k_n=\dfrac{dP_e}{d\delta}=2E^*R^{\frac{1}{2}}\delta^{\frac{1}{2}}=2E^*\sqrt{\dfrac{a}{2\pi}} \qquad \delta\le\delta_c, a\ge a_c \\ K_n^*=\dfrac{K_n}{E^*\sqrt{A_a}}=\dfrac{\int_{a_c}^{a_l}n(a)k_n da}{E^*\sqrt{A_a}}=\dfrac{2}{\sqrt{\pi}}g_3(D)\psi^{\left(\frac{2-D}{2}\right)^2}A_r^{*\frac{D}{2}}\left[\left(\dfrac{2-D}{D}\right)^{\frac{1-D}{2}}\psi^{\frac{-D^2+3D-2}{4}}A_r^{*\frac{1-D}{2}}-a_c^{*\frac{1-D}{2}}\right] \end{cases},$$

(5-19)

where $g_3(D) = \dfrac{D^{\frac{2-D}{2}}(2-D)^{\frac{D}{2}}}{1-D}$.

On the other hand, the ratio of the plastic strain energy W_p to the elastic strain energy W_e can be defined as damping loss factor

$$\eta_C = \frac{W_p}{W_e} = \frac{\int_0^{a_c}\int_0^{\delta} P_p n(a) d\delta da}{\int_{a_c}^{a_l}\int_0^{\delta} P_e n(a) d\delta da} = \frac{15\sqrt{2\pi}H(5-3D)a_c^{2-D}}{16E^* G^{D-1}(2-D)\left(a_l^{\frac{5-3D}{2}} - a_l^{\frac{D}{2}} a_c^{\frac{5-3D}{2}}\right)}. \quad (5\text{-}20)$$

Finally, the relationship between the normalized interfacial damping coefficient C_n and the real contact area A_r can be computed as

$$C_n^* = \frac{C_n}{A_a^{\frac{1}{4}}\sqrt{ME^*}} = \frac{\eta\sqrt{MK_n}}{A_a^{\frac{1}{4}}\sqrt{ME^*}}$$
$$= \frac{42\varphi\sqrt{\pi}(5-3D)a_c^{*(2-D)}\left\{\dfrac{2D}{\sqrt{\pi}(1-D)}(\dfrac{2-D}{D})^{\frac{D}{2}}\psi^{\frac{(D-2)^2}{4}}A_r^{*\frac{D}{2}}\left[\psi^{\frac{-D^2+3D-2}{4}}(\dfrac{2-D}{D})^{\frac{1-D}{2}}A_r^{*(\frac{1-D}{2})} - a_c^{*(\frac{1-D}{2})}\right]\right\}^{\frac{1}{2}}}{2^{\frac{8-D}{2}}G^{*(D-1)}(2-D)\left[\psi^{\frac{-3D^2+11D-10}{4}}(\dfrac{2-D}{D})^{\frac{5-3D}{2}}A_r^{*(\frac{5-3D}{2})} - a_c^{*(\frac{5-3D}{2})}\right]}.$$

(5-21)

According to eqn. (5-18), (5-19), and (5-21), the relationship between the bolt preload P of the bolted joint and the interfacial stiffness/damping coefficient K_n / C_n can be calculated via the real contact area A_r as an intermediary, thus obtaining the mechanical impedance of the bolted joint. Combining this relationship with the effective electro-mechanical modeling proposed earlier, the EMI modeling of the bolted looseness detection can be achieved.

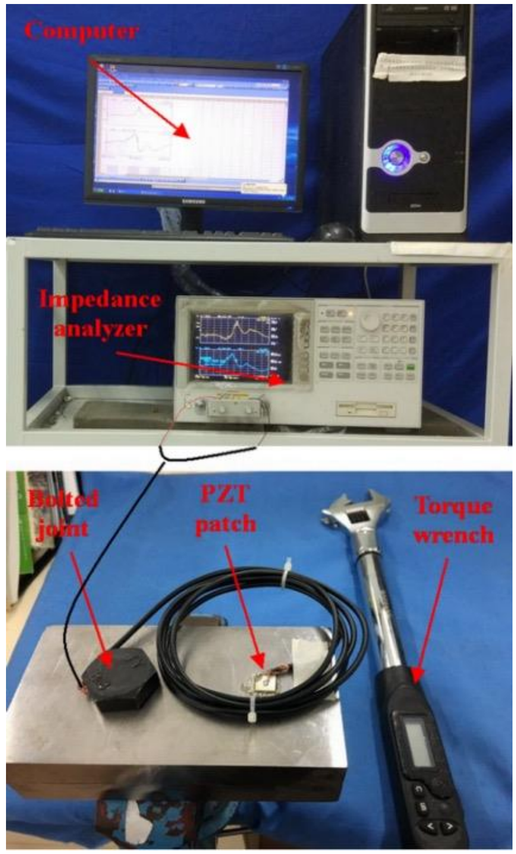

Fig. 5-3 Experimental setup

To verify the effectiveness of the proposed model, the author conducts an experiment, whose apparatus is shown in Fig. 5-3. Overall, a PZT patch (size: 10mm×10mm×1mm) is bonded on the bolted connection through the epoxy resin. The bolted connection consists of two rectangular steel plates (size: 150mm×80mm×20mm) and a pair of M20 bolt and nut. A precision impedance analyzer (Agilent HP4294A) is employed to obtain the electrical impedance of the PZT patch under different preloads (four degrees of bolt preload: 10 Nm, 30 Nm, 50 Nm, and 70 Nm). Notably, the detection sensitivity of the EMI method is affected by the frequency range of the excitation signal [234]. Therefore, as depicted in Fig. 5-4, a swept frequency test is implemented to select proper frequency range [235], and it is clear that the frequency range from 100 kHz to 400 kHz is the optimal frequency range for excitation signals.

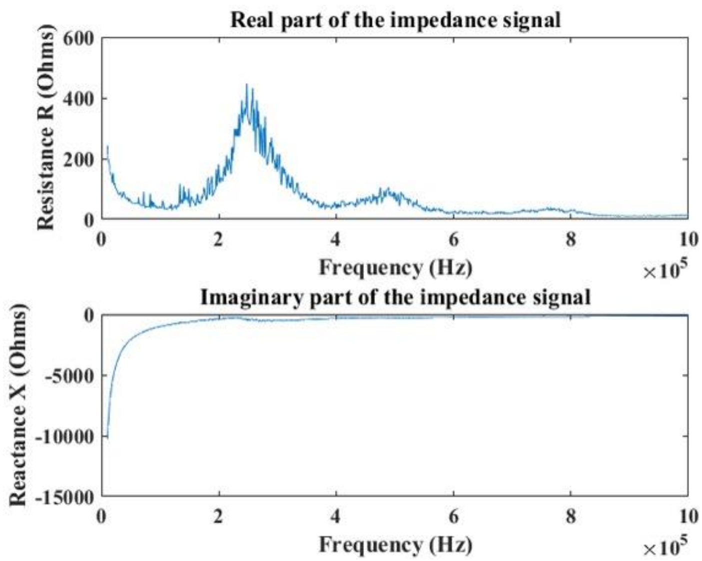

Fig. 5-4 Sweep frequency with rang of 10 Hz - 1MHz

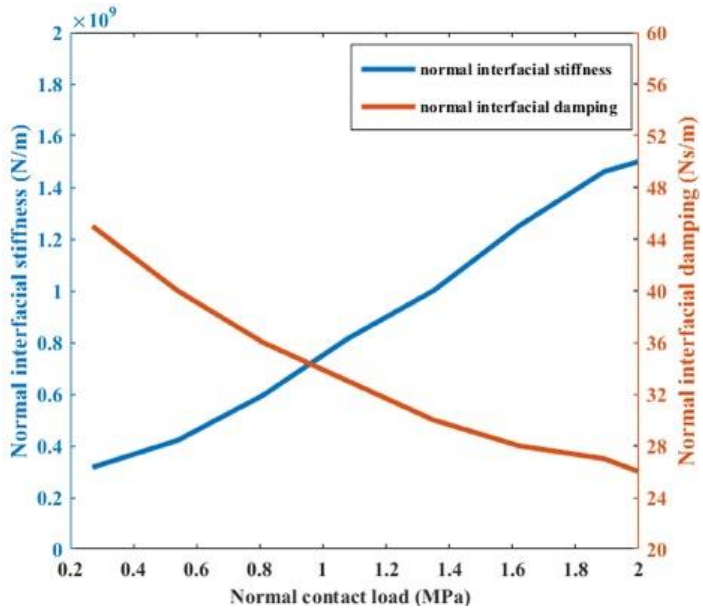

Fig. 5-5 Tendency of interfacial stiffness and damping

Moreover, using materials' properties given in Table 3-1 and the fractal parameters D (1.21) and G (5.26×10^{-14} m) measured by the surface roughness profiler (TALOR HOBSON, PGI 840, UK), the relationships between the interfacial stiffness/damping and the bolt preload is compared, as given in Fig. 5-5, which shows that the interfacial stiffness increases with larger applied torque (i.e., bolt preload), while interfacial damping decreases simultaneously. These phenomena conform previous investigation [236]. Particularly, it is noticed that the change tendency of interfacial stiffness and interfacial damping is prone to saturation, which can be attributed to severe plastic deformation of asperities under heavy axial load.

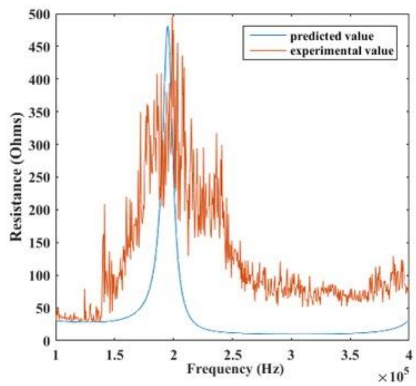

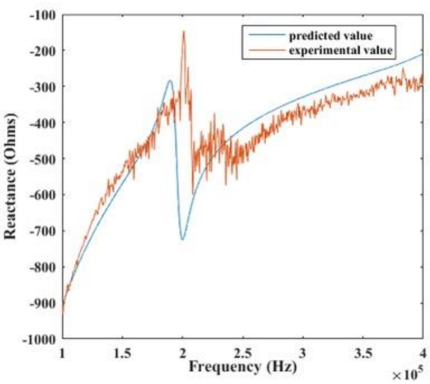

(a) Resistance under 10 N m torque (b) Reactance under 10 N m torque

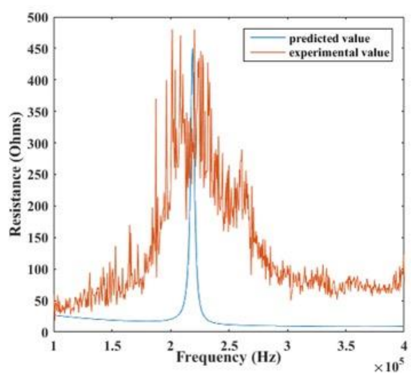

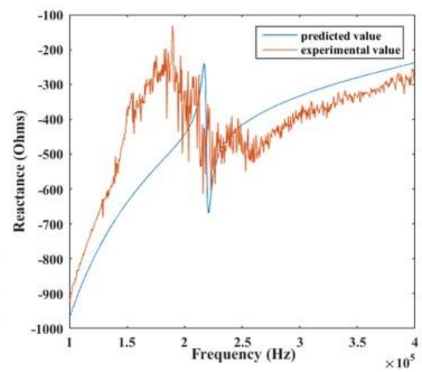

(c) Resistance under 30 N m torque (d) Reactance under 30 N m torque

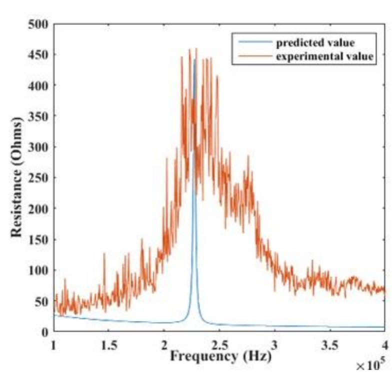

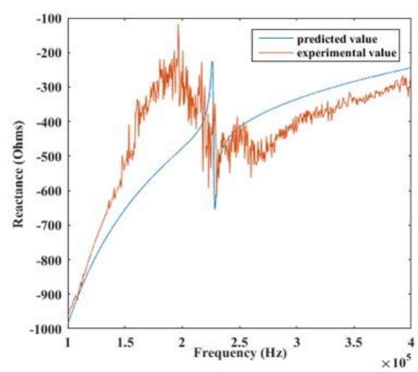

(e) Resistance under 50 N m torque (f) Reactance under 50 N m torque

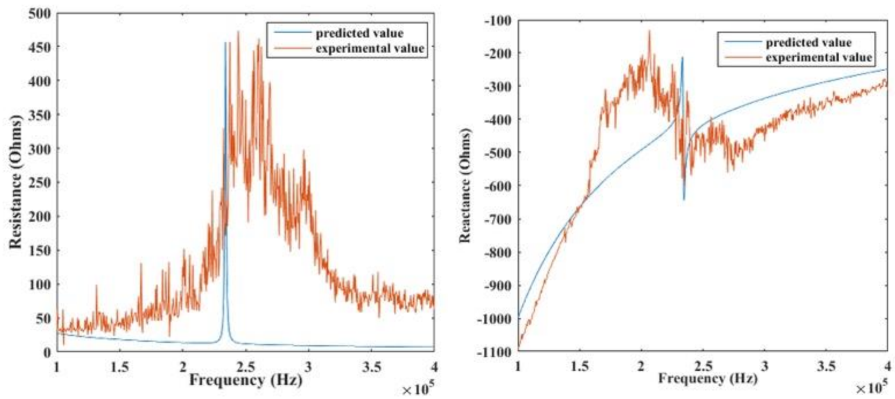

(g) Resistance under 70 N m torque (h) Reactance under 70 N m torque

Fig. 5-6 EMI of predicted and experimental values under various bolted preload

Finally, the resistance and reactance of bolted joint under various loads (10, 30, 50, 70 N m) are obtained by using eqn. (5-11) and compared in Fig. 5-6, which reveals that the resistance of bolted joint decreased with the increase of the applied preload (torque), which is consistent with the previous experimental results [237, 238]. Peak frequency of the resistance signature also increased with the increase of the applied preload, since larger preload can lead to improved interfacial stiffness and increase of the resonance frequency. Based on the comparative results of predicted and experimental values, the validity of the proposed EMI model is verified.

CHAPTER 6. BOLT LOOSENESS DETECTION VIA THE VIBRO-ACOUSTIC MODULATION METHOD

Recently, to circumvent the deficiencies of the active sensing method and EMI method, many researchers have paid more attention to the nonlinear-based ultrasonic methods that depend on nonlinear features such as high-order or semi-order harmonics [240] and resonance frequency shift [241]. Among these nonlinear-based ultrasonic methods, the vibro-acoustic modulation (VAM) method is the most attractive technique, and it has been successfully employed to detect various structural damages, including impact damage [242, 243], crack [244], and fatigue [245, 246]. Particularly, the VAM method has shown good potential in detecting bolt looseness [61], and the schematic is depicted in Fig. 6-1, which shows two kinds of inputs (one is the low-frequency (LF) vibration and the other one is high-frequency (HF) ultrasonic wave) are used to excite the bolted joint. The LF vibration will enable the imperfect contact interface caused by bolt looseness to close and open periodically (i.e., “breathing”), thus inducing a modulation with the HF permutation. Finally, this modulation can be expressed as the nonlinear features such as sidebands in the frequency spectrum, and the tightness of bolted joint can be identified by quantifying the sideband.

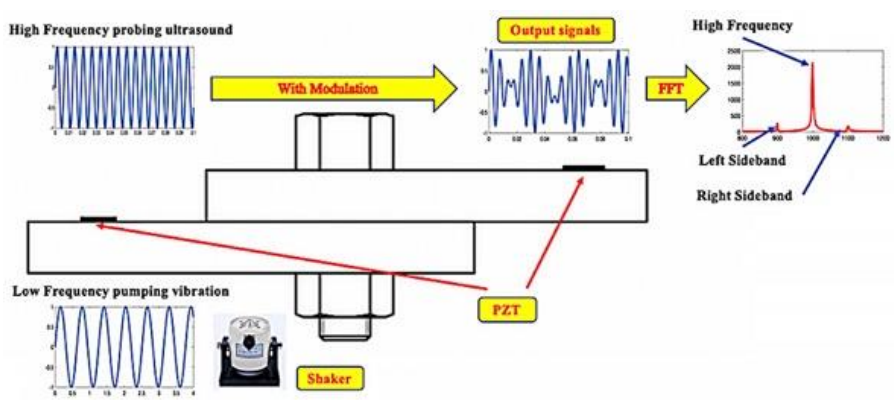

Fig. 6-1 Schematic diagram of the traditional VAM-based method for a loosening bolt

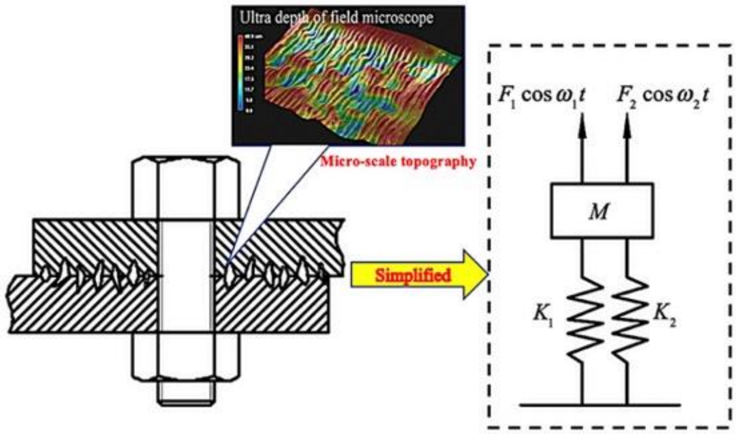

Fig. 6-2 Simplified model of a bolted joint

The working mechanism of the VAM method can be mathematically described as follows. As shown in Fig. 6-2, the bolted joint as a one-degree-of-freedom system is considered, and its motion equation under the LF vibration and HF ultrasonic can be given as

$$M\ddot{x} + K_1 x - \varepsilon K_2 x^2 = F_1 \cos \omega_1 t + F_2 \cos \omega_2 t \,, \tag{6-1}$$

where $F_1 \cos \omega_1 t$ is the LF vibration with frequency ω_1; $F_2 \cos \omega_2 t$ is the HF ultrasonic wave with frequency ω_2; M is the mass; K_1 is the linear stiffness; K_2 is the nonlinear stiffness; ε denotes the permutation; t is the time. Then, based on the permutation theory, the solution to eqn. (6-1) can be expressed as

$$x = x_1 + \varepsilon x_2 \,, \tag{6-2}$$

where x_1 and x_2 are linear and nonlinear responses of the bolted joint, respectively. It is worth noting that x_2 is caused by sidebands. Subsequently, substituting eqn. (6-2) into eqn. (6-1) eliminates ε-related terms and achieves the following relationships

$$\begin{gathered} M\ddot{x}_1 + K_1 x_1 = F_1 \cos \omega_1 t + F_2 \cos \omega_2 t \\ M\ddot{x}_2 + K_1 x_2 = K_2 x_1^2 \end{gathered} \,. \tag{6-3}$$

Finally, the magnitude of sideband in the frequency spectrum can be obtained via the following formula

$$x_{sidebands} = \frac{G_1 G_2}{K_1 - M(\omega_2 + \omega_1)^2} K_2 \cos(\omega_2 + \omega_1)t + \frac{G_1 G_2}{K_1 - M(\omega_2 - \omega_1)^2} K_2 \cos(\omega_2 - \omega_1)t \text{ ,(6-4)}$$

where $G_1 = \frac{F_1}{K_1 - M\omega_1^2}$ and $G_2 = \frac{F_2}{K_1 - M\omega_2^2}$. Obviously, it can be seen that the left sideband and the right sideband are located at frequencies ω_1 and ω_2 .

However, several deficiencies hamper the further applications of the VAM for bolt looseness detection: (1) LF vibration in current VAM is implemented by using a shaker, which is impractical on site sometimes; (2) both LF and HF inputs are single-frequency harmonics, and the capacity of the VAM severely depends on the prudent selection of special values, while it is impossible to achieve the optimal inputs in most cases [247, 248]. Therefore, a new entropy-enhanced VAM method is developed to overcome drawbacks of current VAM and improve practicability.

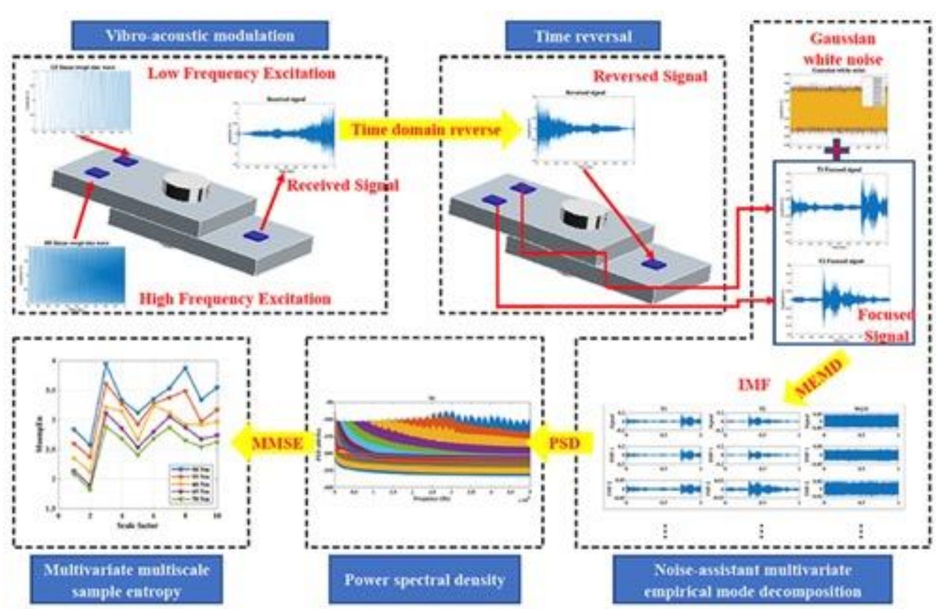

Fig. 6-3 Schematic diagram of the entropy-enhanced VAM method

6.1 Entropy-enhanced vibro-acoustic modulation method for bolt early looseness

The flowchart of the proposed entropy-enhanced vibro-acoustic modulation method is illustrated in Fig. 6-3, which shows that it consists several parts, including the improved VAM, the time-reversal (TR), the noise-assistant multivariate empirical mode decomposition (NA-MEMD) [249, 250] and multivariate multiscale sample entropy (MMSE) [251]. Particularly, the LF and HF inputs are replaced with swept sine waves, which is inspired by previous investigations [252, 253, 254]. In other words, no prudent selection (or priori knowledge of monitored structures) of LF and HF signals is needed. Moreover, the shaker for LF vibration in current VAM method is replaced by a PZT transducer, which is easier to implement in practice. Finally, a relationship between bolt preload and MMSE-based damage index is developed to quantify early looseness.

On the other hand, the traditional damage index (i.e., quantification of sidebands) is no longer applicable for the improved VAM method, since the swept sine waves are used. Therefore, an MMSE-enabled damage index is developed to quantify the received modulation waves to identify the bolt looseness. Particularly, the TR technique and NA-MEMD approach are used to strengthen the looseness-related nonlinearity performance and relieve the effect of environment noise. More details about TR, NA-MEMD and MMSE are introduced as follows.

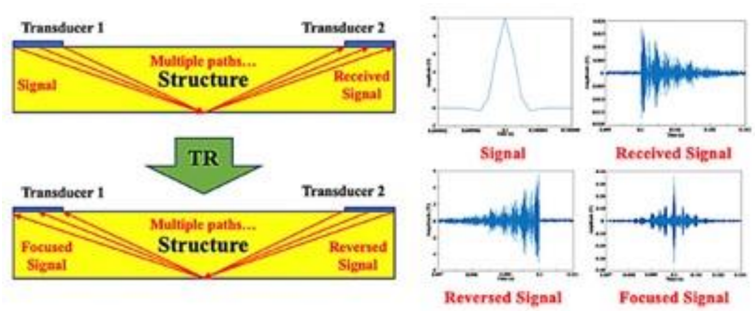

Fig. 6-4 Schematic diagram of the Time reversal (TR) method

As introduced earlier [103, 104], the TR technique that is derived from the reciprocity principle can be used to focus the energy of ultrasonic signals, and its implementation is illustrated in Fig. 6.4 and is described as follows.

Denoting an input signal $f(t)$ that is emitted from Transducer 1, the received signal $u(t)$ is obtained by summarizing all multi-path propagation as

$$u(t) = \sum_{i=1}^{\infty} A_i f(t - t_i), \tag{6-5}$$

where i is the path number during the propagation path, t_i is the time delay of ith path, A_i is the wave amplitude of path. Then, the reversal signal $f^{TR}(t)$ can be achieved by reversing the received signal in time-domain with normalization as

$$u(T-t) = \sum_{i=1}^{\infty} A_i f(T - t - t_i) \Rightarrow f^{TR}(t) = \sum_{i=1}^{\infty} \frac{A_i}{A_{\max}} f(T - t - t_i), \tag{6-6}$$

where T is the time range of received signal, and $A_{\max}$ is the maximum value of A_i. Finally, by resending the reversal signal as a new excitation from Transducer 2, and the focused signal $u^{TR}(t)$ can be obtained at Transducer 1 as

$$u^{TR}(t) = \sum_{j=1}^{\infty} \sum_{j \neq i}^{\infty} \frac{A_j A_i}{A_{\max}} f(T - (t - t_j) - t_i) = \sum_{i=j=1}^{\infty} \frac{A_j A_i}{A_{\max}} f(T - t) + \sum_{j=1}^{\infty} \sum_{j \neq i}^{\infty} \frac{A_j A_i}{A_{\max}} f(T - t + t_j - t_i), \tag{6-7}$$

where A_j is the amplitude of reversed signal amplitude, j is the path number of the reversed signal during the propagation, t_j is the time delay of the reversed signal. Particularly, when $t_j = t_i$, one can obtain $f(T-t)$ that means all signals from different paths arrive simultaneously. On the other hand, $f(T-t+t_j-t_i)$ is obtained when $t_j \neq t_i$ (i.e., the side peaks around the main peak).

The multivariate empirical mode decomposition (MEMD) [255] is developed to circumvent the disadvantages of the empirical mode decomposition (EMD) [256], i.e., lack of abilities to address multivariate signals. Overall, after projecting a n-variable signal to the direction vectors with $n-1$ dimensions, the MEMD algorithm can be employed to decompose the original n-variable signal into several intrinsic mode functions (IMFs) via the EMD. In other words, there are two issues that affect the performance of MEMD: (1) the construction of direction vectors; (2) the stopping criterion for IMFs calculation (i.e., the sifting process). Here, the Hammersley sequence [257] (i.e., quasi-Monte Carlo lower deviation sequence) is employed to construct the direction vectors, and the stopping criterion is given as: the Cauchy-type convergence condition through a threshold (0.2) [258]. The detailed procedure of the MEMD can be described as follows.

(1) First can denote a n-variable signal $\left\{\boldsymbol{y}(t)\right\}_{t=1}^{T}=\left\{y_1(t), y_2(t), \cdots, y_n(t)\right\}$ and assume that it can be decomposed into J IMFs as

$$\boldsymbol{y}(t)=\sum_{j=1}^{J}\boldsymbol{d}_j(t)+\boldsymbol{r}(t)\,, \tag{6-8}$$

where $\boldsymbol{d}_j(t)$ is the jth IMF of $\boldsymbol{y}(t)$, $\boldsymbol{r}(t)$ is the residual.

(2) Based on the Hammersley sequence, the direction vectors $\boldsymbol{X}^{\theta_k}$ can be constructed on a $n-1$ dimensional space as

$$\boldsymbol{X}^{\theta_k}=\left\{x_1^k, x_2^k, \cdots, x_n^k\right\}, \tag{6-9}$$

where $\boldsymbol{\theta}_k = \left\{\theta_1^k, \theta_2^k, \cdots, \theta_n^k\right\}$ is the angle in the space, and $k = 1, 2, \cdots, K$.

(3) Then, $\boldsymbol{y}(t)$ can be projected along the direction vectors as $\left\{\boldsymbol{p}^{\theta_k}(t)\right\}_{k=1}^{K}$.

(4) The time constant $\left\{\boldsymbol{t}_i^{\theta_k}(t)\right\}_{k=1}^{K}$ can be figured out via the maximum $\left\{\boldsymbol{p}^{\theta_k}(t)\right\}_{k=1}^{K}$.

(5) By interpolating $\left[\boldsymbol{t}_i^{\theta_k}, \boldsymbol{y}(t_i^{\theta_k})\right]$, one can obtain the multivariate envelops $\left\{\boldsymbol{e}^{\theta_k}(t)\right\}_{k=1}^{K}$.

(6) The mean value of envelops can be calculated as

$$\boldsymbol{m}(t) = 1\Big/K\sum_{k=1}^{K}\boldsymbol{e}^{\theta_k}(t)\ . \tag{6-10}$$

(7) $\boldsymbol{d}_j(t)$ can be calculated as $\boldsymbol{d}_j(t) = \boldsymbol{y}(t) - \boldsymbol{m}(t)$. Finally, one can implement the judgment of stopping criterion: if so, the IMF component and residual $\boldsymbol{r}_j(t) = \boldsymbol{y}(t) - \boldsymbol{d}_j(t)$ can be determined; if not, repeating Steps (2)-(6) to obtain another $\boldsymbol{d}_j(t)$.

Furthermore, the NA-MEMD [249, 250] was developed to enhance the performance of MEMD by adding white Gaussian noise (WGN) into the n-variable signal, and the detailed implementation can be introduced as follows:

(1) First create a l-variable signal WGN signal and add it into the input (i.e., n-variable signal) to construct a $l+n$-variable signal. Please note that the EGN signal and input have the same length.

(2) Using the MEMD algorithm, one can obtain the IMFs of this $l+n$-variable signal.

(3) Finally, one discards the WGN signal from the $l+n$-variable signal to extract a set of IMFs of the original n-variable signal.

The MMSE [251] is proposed to address the issue of multi-channel signals for the calculation of multivariate sample entropy (MSampEn), and its computation process is given as follows:

(1) First denote a n-variable signal $\left\{x_{k,i}\right\}_{i=1}^{N}$ ($k=1,2,\cdots,n$), and then a coarse-grained multivariate input can be expressed as

$$y_{k,j}^{\varepsilon}=\frac{1}{\varepsilon}\sum_{i=(j-1)\varepsilon+1}^{j\varepsilon}x_{k,i}\ , \tag{6-11}$$

where $1\leq j\leq N/\varepsilon$, and ε is the scale factor.

(2) Based on the multivariate embedding theory [251], a composite delay vector can be developed as

$$X_m(i)=\left[x_{1,i},\cdots,x_{1,i+(m_1-1)\tau_1},x_{2,i},\cdots,x_{2,i+(m_2-1)\tau_2},\cdots,x_{p,i},\cdots x_{p,i+(m_p-1)\tau_p}\right], \tag{6-12}$$

where $X_m(i)\in\mathbb{R}^m$; $\mathbf{M}=\left[m_1,m_2,\cdots m_n\right]\in\mathbb{R}^n$ is the embedding vector, $\boldsymbol{\tau}=\left[\tau_1,\tau_2,\cdots\tau_n\right]$ is the time lag vector, $i=1,2,\cdots,N-p$; $p=\max\left\{\mathbf{M}\right\}\times\max\left\{\boldsymbol{\tau}\right\}$.

(3) Then, the maximum form is defined as the distance between two vectors $X_m(i)$ and $X_m(j)$ as

$$d\left[X_m(i),X_m(i)\right]=\max_{l=1,\cdots,m}\left\{\left|x(i+l-1)-x(j+l-1)\right|\right\}. \tag{6-13}$$

(4) Using a threshold r, one can count the total number of cases P_i that satisfy $d\left[X_m(i),X_m(i)\right]\leq r$, $j\neq i$, and compute the corresdponding frequency as

$$B_i^m(r)=P_i/(N-p-1) \tag{6-14}$$

and

$$B^m(r) = \sum_{i=1}^{N-p} B_i^m(r) \big/ (N-p) . \tag{6-15}$$

(5) Similarly, after extending the composite delay vectors from $X_m(i)$ to $X_{m+1}(i) \in \mathbb{R}^{m+1}$, one can obtain total number of cases Q_i that satisfy $d\left[X_{m+1}(i), X_{m+1}(i)\right] \le r,\ j \ne i$, and compute the corresdponding frequency as

$$B_i^{m+1}(r) = Q_i \big/ (n(N-p)-1) \tag{6-16}$$

and

$$B^{m+1}(r) = \sum_{i=1}^{n(N-p)} B_i^{m+1}(r) \big/ n(N-p) . \tag{6-17}$$

(6) Finally, the MSampEn of each $y_{k,j}^{\varepsilon}$ (i.e., MMSE of the original n-variable signal $\{x_{k,i}\}_{i=1}^{N}$) can be computed as

$$MSampEn(\mathbf{M}, \boldsymbol{\tau}, r, N) = -\ln\left[\frac{B^{m+1}(r)}{B^m(r)}\right]. \tag{6-18}$$

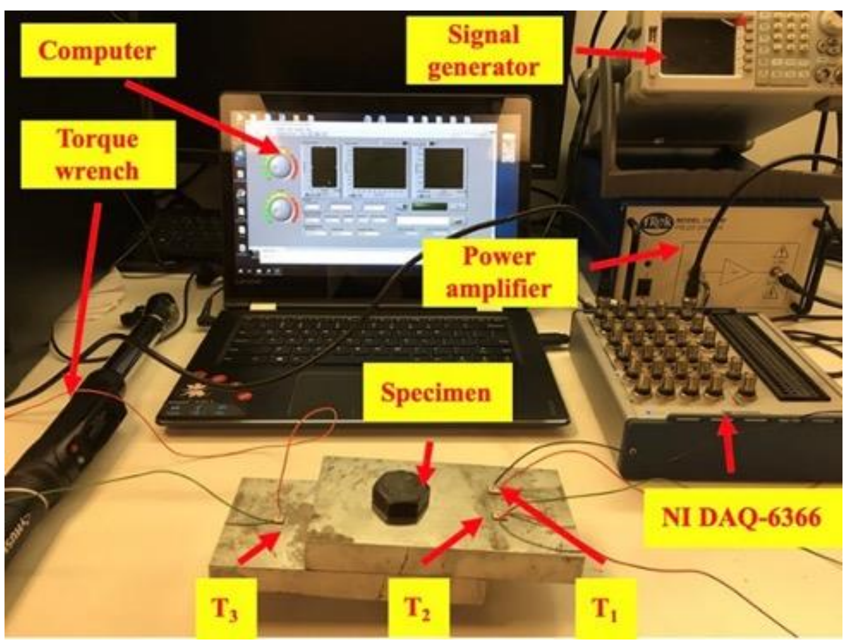

Fig. 6-5 Experimental setup

To demonstrate the proposed entropy-enhanced VAM method, the author conducts a lab test, whose apparatus is depicted in Fig. 6-5 [259]. Three PZT transducers (denoted as T1, T2, and T3) are bonded on an M20 bolted joint (steel plate size: 150mm×80mm×20mm) to implement the entropy-enhanced VAM method. A swept sine waves (duration: 1s; frequency range: 100Hz-2 kHz) is generated via a signal generator (SIGLENT SDG 1025), and it is fed into a power amplifier (Trek Model-2100HF) to expand to 250 V to excite T1 (i.e., working as LF vibration). On the other hand, a swept sine wave from 100 kHz to 300 kHz (duration: 1 s) is emitted through an NI DAQ system (NI USB-6366) and is fed into T2 to work as HF ultrasonic wave. Then, the received signal is captured in T3 with sampling rate of 1 MHz. Finally, after the reversing implementation (i.e., the TR technique), the focused signal can be obtained at T1 and T2. In this section, the bolt preload is set to a range of 50 to 70 N m with an increment of 5 N m since the active sensing is employed to determine the early looseness stage of the used bolted joint (as shown in Fig. 6-6).

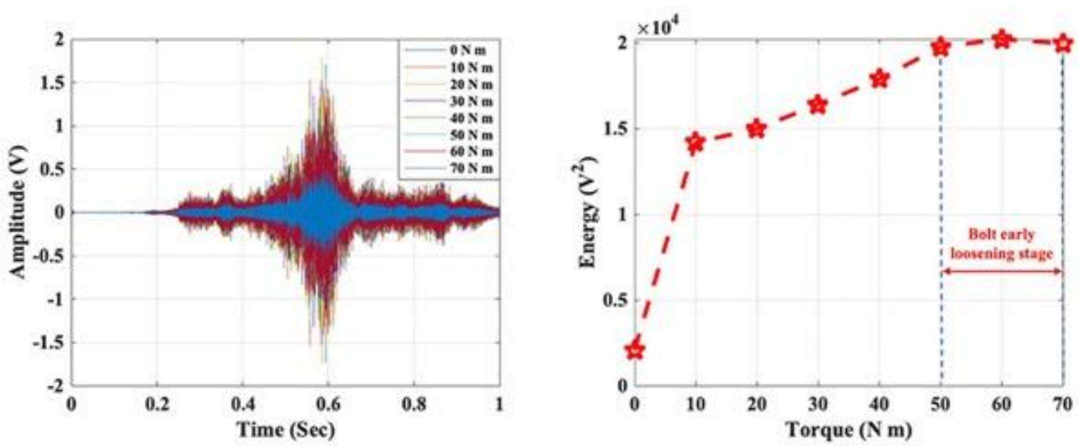

Fig. 6-6 Received signal by active sensing method and corresponding energy versus bolt pre-load

The received focus signals of T1 and T2, and the WGN signal are decomposed to 22 IMFs and a residual. Then, an example (preload: 50 N m) is illustrated in Fig. 6-7.

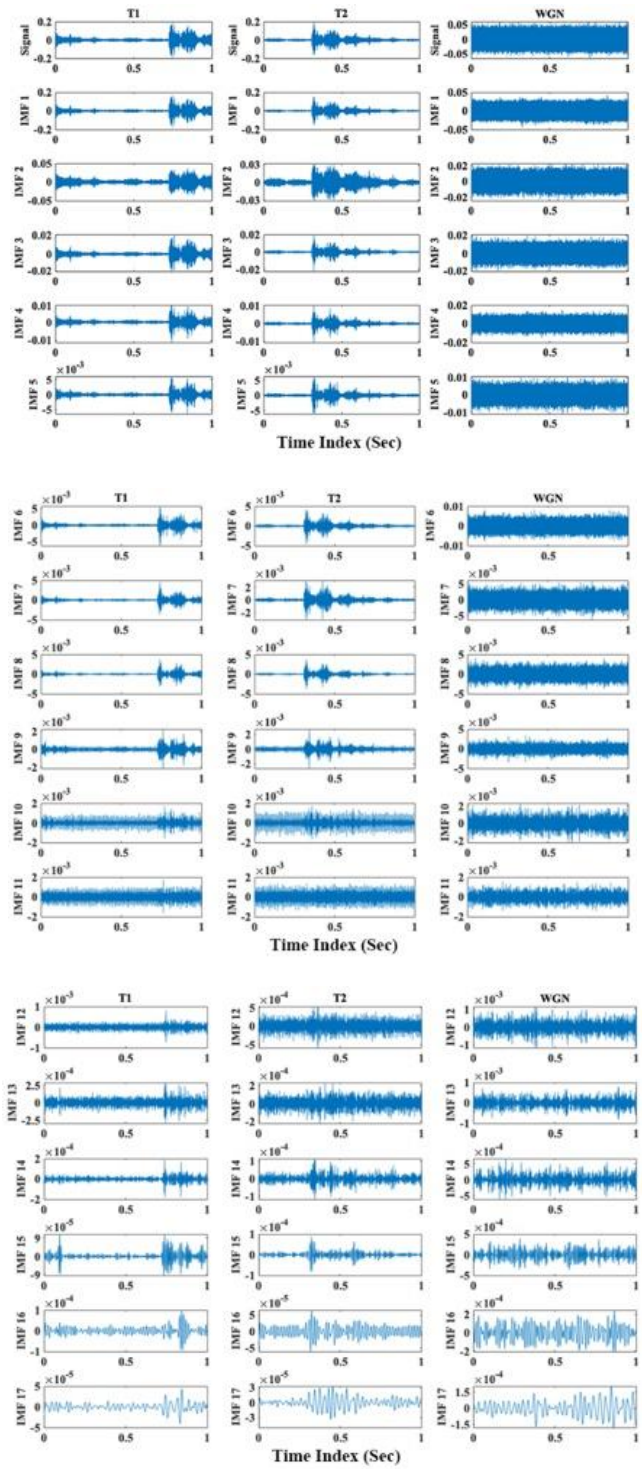

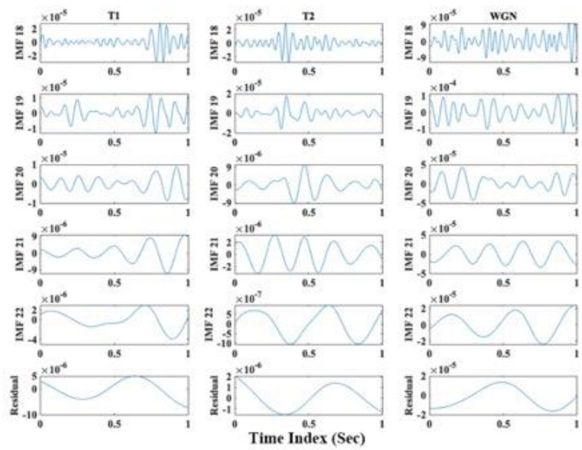

Fig. 6-7 Decomposition results of multivariate signal using NA-MEMD

Then, to select the most significant IMF for MMSE computation, the power spectral density (PSD) of all IMFs is constructed to find that the first IMFs of T1 signal and T2 signal have the maximum values, as depicted in Fig. 6-8. Thus, the MMSE algorithm is used to calculate their MSampEn; particularly, the embedding parameter m is set to 2, and the time lag vector τ is set to 1. Moreover, the threshold r is set to 0.15 times the standard deviation of the normalized input, and the range of scale factor is from 1 to 10. The results of MMSE under different preloads (55 N m, 60 N m, 65 N m, and 70 N m) are depicted in Fig. 6-8 (please note that each preload is repeated for eight times to ensure the repeatability).

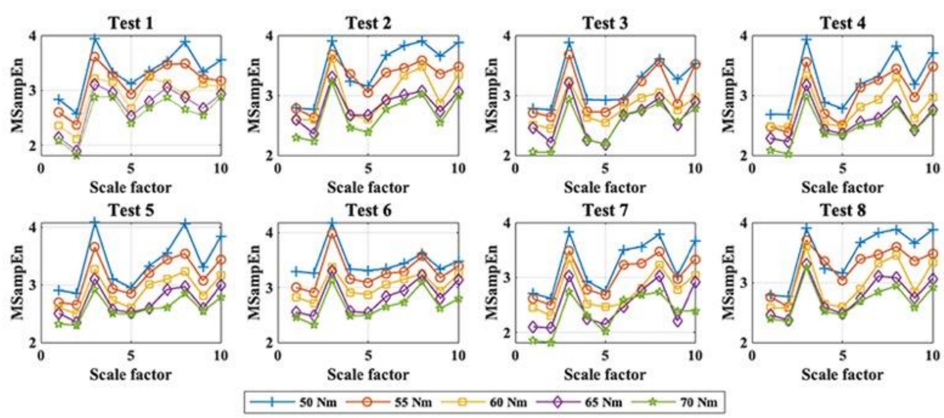

Fig. 6-8 MMSE analysis results under different torque levels (repeat eight times)

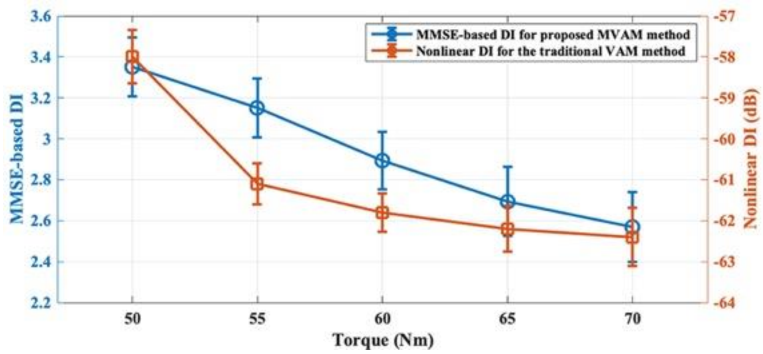

Fig. 6-9 Comparison of performance between the proposed entropy-enhanced VAM method and traditional VAM method

Finally, by calculating the average of MMSE under all scale factors, a new MMSE-based damage is developed to quantify the bolt early looseness. The proposed entropy-enhanced VAM method shows the monotonic tendency, while current VAM method is prone to saturation. In other words, the proposed entropy-enhanced VAM method is more sensitive to bolt early looseness, which demonstrates the advantage.

6.2 Multi-bolt looseness detection via the entropy-enhanced vibro-acoustic modulation method

Another issue ignored in the previous investigations is that the potential of the VAM method for multi-bolt looseness detection. Therefore, in this section, a new entropy-enhanced VAM method is developed to detect multi-bolt looseness with the help of the machine learning technique. The flowchart of the overall strategy of multi-bolt looseness detection is depicted in Fig. 6-10. The improved VAM (i.e., both LF and HF inputs are swept sine waves) is first implemented on a multi-bolt connection, and the sparse representation method [260] is used to preprocess the data to improve computation efficiency and exclude redundant features. Then, a new entropy index (i.e., Gnome entropy [261], which as abbreviated as *gEn*) is proposed to estimate the complexity of expressed modulation signals to construct the training and testing dataset.

Finally, a random forest classifier [262] is used to identify different bolt preloads (i.e., multi-bolt looseness detection). More detailed about the *gEn*, the sparse representation, and the random forest will be introduced later.

The detailed computation of *gEn* is given as follows:

(1) First denote a time series $x = x_1, x_2, \cdots x_N$, which can be mapped into a space with m dimension as

$$X = X_1, X_2, \cdots X_{N-m+1}, \tag{6-19}$$

where $X_i = (x_i, x_{i+1}, \cdots x_{i+m-1})$.

(2) For each vector, the Gnome sort algorithm (generally, it is called as stupid sort) is used to implement sort in ascending order. Particularly, the necessary swaps for the sort is denoted as n_i.

(3) After denoting that the probabilities of n_i is p_i, one can calculate the *Renyi* permutation entropy [263] as

$$RpEn^m = \frac{1}{1-\alpha} \log\left(\sum_{i=1}^{n} p_i^{\alpha}\right), \tag{6-20}$$

where $\alpha = 2$, and the reason is that previous investigation has demonstrated that $\alpha = 2$ has the best performance at the most cases.

(4) Extending m to $m+1$, one can obtain $RpEn^{m+1}$ by repeating Steps (2) and (3).

(5) Finally, based on previous investigation [263], the *gEn* can be obtained as

$$gEn = \frac{RpEn^{m+1} - RpEn^m}{\log(m+1/m-1)}. \tag{6-21}$$

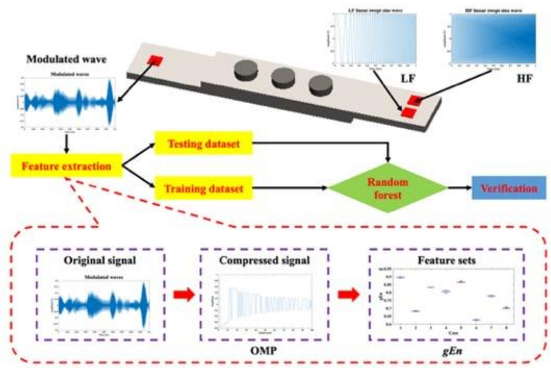

Fig. 6-10 Schematic diagram of the proposed strategy

Subsequently, tests are conducted to verify the effectiveness of the proposed *gEn*, and the first one is stationary test. Two kinds of noise signal (i.e., Gaussian white noises and $1/f$ noises) with different lengths (N = 6144, 8192 and 10,240) are employed, and their *gEn* results under dimension m (from 2 to 10) are depicted in Fig. 6-11. Moreover, the results of sample entropy (tolerance $r = 0.2SD$, SD is standard derivation of input) and permutation entropy (time delay $\lambda = 1$) are given as comparison. It is clear that sample entropy and permutation entropy have good stability under different signal length, while they are sensitive to the dimension m (the performance of sample entropy is better than permutation entropy; however, sample entropy depends on tolerance r severely). On the other hand, the *gEn* has the best stability without extra parameters such as tolerance r and time delay λ.

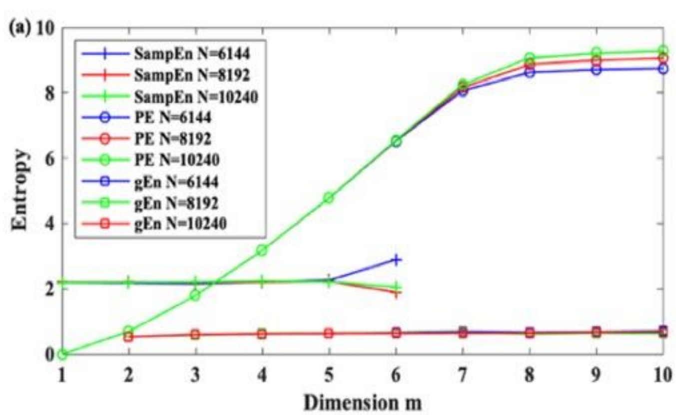

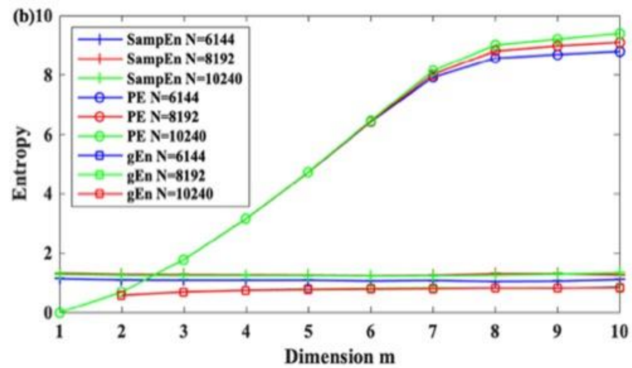

Fig. 6-11 Stability analysis under varying length N and dimension m (a) Gaussian white noises (b) $1/f$ noises

Another testing is the distinguishing capacity of the *gEn*, including synthetic signals and a widely accepted database, i.e., the Rolling Bearing Data Center of Case Western Reserve University [193]. First, the author generates six synthetic signals: $x_1 = \sin(2\pi 10t)$, $x_2 = \sin(2\pi 30t)$, $x_3 = \sin(2\pi 60t)$, $x_4 = x_1 + x_2$, $x_5 = x_2 + x_3$, $x_6 = x_1 + x_2 + x_3$, and the computaion results of the *gEn* for six synthetic signals are shown in Fig. 6-12. Several phenomena can be found: signal with larger frequency leads to larger *gEn* (e.g., $gEn(x_3) > gEn(x_2) > gEn(x_1)$); mixed signal has larger *gEn* than single signal (e.g., $gEn(x_4) > gEn(x_1)$). These phenomena are explainable, since the complexity of signal is related to frequency (generally, higher frequency means more complexity), and multiple components in the mixed signal can also increase complexity.

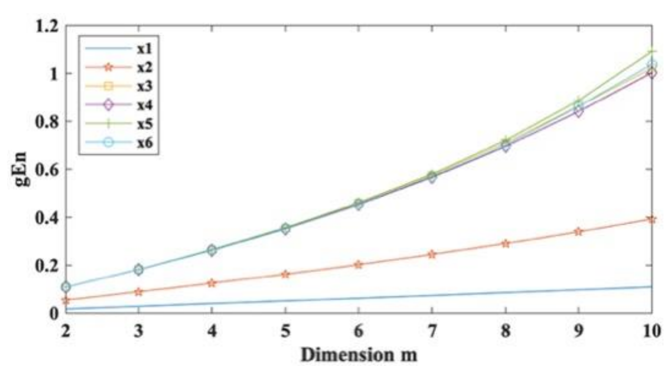

Fig. 6-12 *gEn* of multiple signals with varying frequencies

Furthermore, the author selects four normal rolling bearing data under Load HP0 (rotate speed: 1797 rpm), Load HP1 (rotate speed: 1772 rpm), Load HP2 (rotate speed: 1750 rpm), and Load HP3 (rotate speed: 1730 rpm), and denotes them as N1, N2, N3, and N4, respectively. The comparison of *gEn* for four cases is illustrated in Fig. 6-13, which shows good consistence. In other words, it is demonstrated again that the *gEn* is not sensitive to signal length and has good stability. Then, three cases of rolling bearings that have fault at different locations (F1: inner race, F2: ball, and F3: outer race) are selected, and the *gEn* of these three cases with N1 are compared, as shown in Fig. 6-13. Since the differences among four cases are obvious, it can be concluded that the distinguishing capacity of *gEn* is reliable.

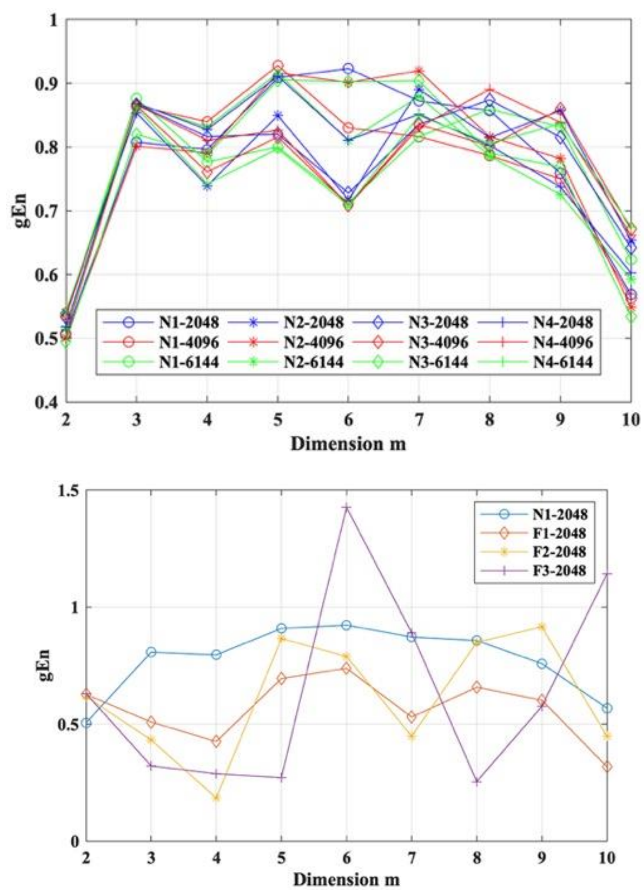

Fig. 6-13 *gEn* of rolling bearing data under different cases

Then, as a kind of linear representation method, the sparse representation approach [260] has been widely used to improve efficiency of signal processing. Particularly, it can also be utilized to extract more significant features from original signal. As depicted in Fig. 6-14, the basic concept of the sparse representation can be described as follows. A d dimensional column vector y can be approximated by a $d \times n$ dimensional matrix $\boldsymbol{X} = [x_1, x_2, \cdots x_n]$ (known as dictionary) as

$$y = x_1\alpha_1 + x_2\alpha_2 + \cdots x_n\alpha_n = \boldsymbol{X}\alpha \, , \tag{6-22}$$

where $\alpha = [\alpha_1, \alpha_2, \cdots \alpha_n]^T$ is the coefficient matrix.

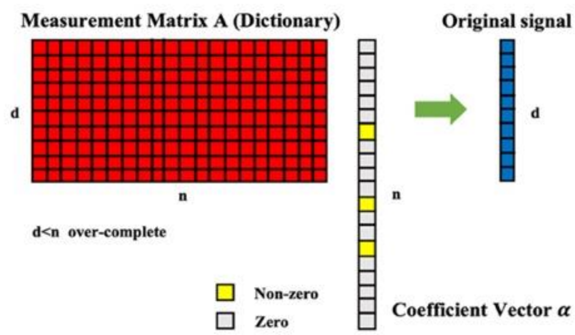

Fig. 6-14 Schematic diagram of the sparse representation

Generally, to solve eqn. (6-22), several researchers have proposed some approaches, including two kinds: the greedy strategy approximation and the convex relaxation algorithms. Particularly, the orthogonal matching pursuit (OMP) algorithm [264] is one of the most popular methods, and thus is employed to compress the modulation signals in the VAM method. Overall, the object of the OMP is to find the l_0 -norm minimization constraint $\hat{\alpha} = \arg\min \| \alpha \|_0$ $(s.t. \, y = \boldsymbol{X}\alpha)$ [265], and the detailed procedure can be implemneted as follows.

(1) First, denote initial conditions: $\alpha = 0$, residual $r_0 = y$, $t = 1$, index set $\Lambda_0 = \phi$, where ϕ is an empty set; $\| r_t \| > \tau$; τ is a small constant.

(2) The largest inner product between r_{t-1} and x_i can be found by using $\lambda_t = \arg\max_{i \notin \Lambda_{t-1}} \left| \langle r_{t-1}, x_i \rangle \right|$.

(3) Via the $\Lambda_t = \Lambda_t \cup \lambda_t$, one can reconstruct the dictionary as $\boldsymbol{X}_t = [\boldsymbol{X}_{t-1}, x_{\lambda_t}]$.

(4) Using the least square method, one can obtain the coefficient $\hat{\alpha} = \arg\min \| y - \boldsymbol{X}_t \hat{\alpha} \|_2$ and thus update the residual as $r_t = y - \boldsymbol{X}_t \hat{\alpha}$.

(5) Finally, increase t to $t+1$, one can obtain the output $\hat{\alpha}$ by repeating Steps (2)-(4).

The random forest [262], which is a kind of ensemble learning technique, can be used as a classifier, and its operation can be expressed as follows:

(1) For an original data (i.e., feature set), n_{tree} bootstrap samples can be obtained,

(2) For each sample, grow an unpruned classification tree and choose the best split among m_{try} predictors,

(3) By summarizing predictions of all n_{tree} trees, one can implement the final prediction,

(4) Additionally, the predictions of “out-of-bag (OOB)” can be used to obtain the error.

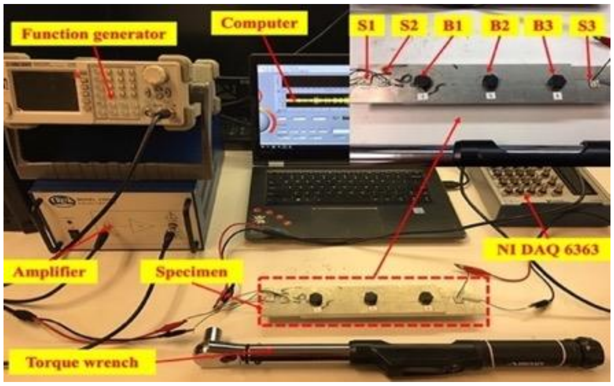

Fig. 6-15 Experimental apparatus

To demonstrate the effectiveness of the proposed entropy-enhanced VAM method, the author conducts an experiment, whose apparatus is shown in Fig. 6-15. Three PZT transducers (S1, S2, and S3) are bonded on a three-bolt (M8) bolted connection (aluminum plate size: 150mm×80mm×20mm). For convenience, denote these three bolts as B1, B2, and B3. LF vibration (frequency range: 100 Hz-2 kHz; duration: 0.1 s; amplitude: 250 V augmented by Trek Model-2100HF amplifier) generated by a function generator (Siglent SDG 1025) is fed into S1, and HF ultrasonic (frequency range: 30 kHz-50 kHz; duration: 0.1 second; amplitude: 10 V) is used to excite S2. Eight different cases (i.e., multi-bolt looseness) are selected, and detailed arrangement is given in Table 6-1. For each case, the tests repeat 50 times (i.e., 400 samples in total).

Table 6-1 Detailed scenarios of experimental

Case	B1	B2	B3
1	Loose	Loose	Loose
2	Tighten	Loose	Loose
3	Loose	Tighten	Loose
4	Loose	Loose	Loose
5	Tighten	Tighten	Loose
6	Tighten	Loose	Tighten
7	Loose	Tighten	Tighten
8	Tighten	Tighten	Tighten

Then, the received modulation signals captured by S3 via a NI multifunction DAQ device (USB 6363), and corresponding frequency spectra are illustrated in Fig. 6-16. It is worth noting that we cannot directly see significant from received signals (from both time domain and frequency domain). Then, using OMP algorithm and *gEn* to construct the training dan testing dataset. Particularly, the dictionary for OMP consists of the Daubechies least-asymmetric wavelet packet (four vanishing moments at fifth level), the discrete cosine transform (DCT) basis, the shift Kronecker delta sub-dictionary and the sine sub-dictionary.

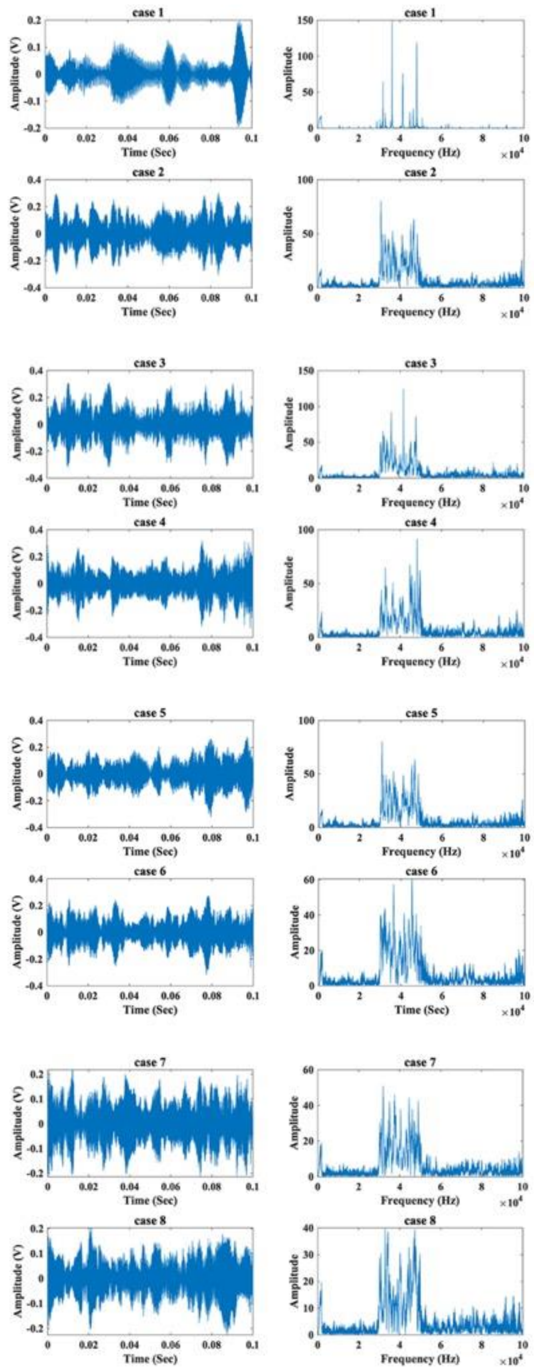

Fig. 6-16 Time domain signals and corresponding frequency spectra of modulated waves

For *gEn* calculation, the dimension m is set to 6. The computation results of *gEn* with OMP and without OMP are illustrated in Fig. 6-17.

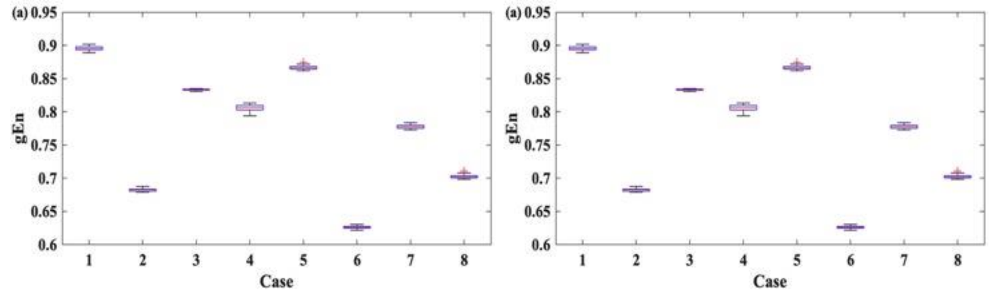

Fig. 6-17 *gEn* values under 8 different cases (a) with the OMP compression (b) without the OMP compression

Finally, a random forest classifier (m_{try} = 1; $n_{tree} = 80$) is trained to identify multi-bolt looseness, and the results are given in Fig. 6-18. A total of 240 (30×8) samples is used to train the random forest model, and the other 160 (20×8) samples are used for testing. It is observed that the combination of OMP and *gEn* achieves the best performance, which demonstrates the effectiveness of the proposed method.

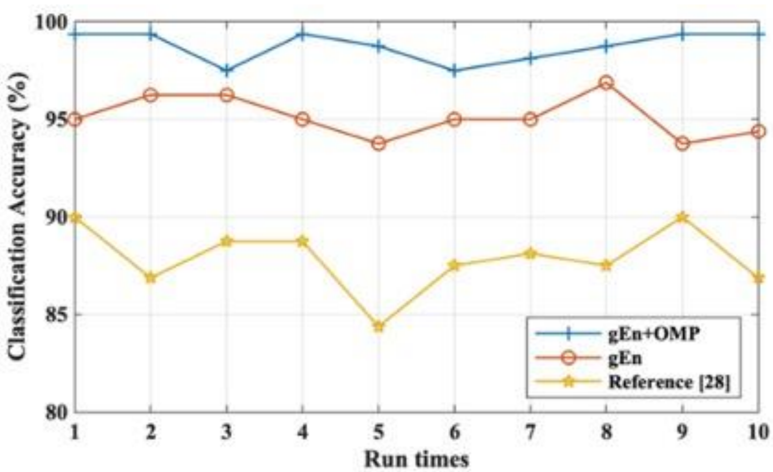

Fig. 6-18 Classification accuracy results

CHAPTER 7. BOLT LOOSENESS DETECTION BY USING THE PERCUSSION-BASED METHOD

The previous chapters have presented several methods to detect bolt looseness, including the active sensing method, EMI method, and VAM method. Overall, these methods are effective, while all of them require permanent contact between PZT transducers and bolted connections. Please note that this requirement will induce more cost and may be impractical in some harsh working conditions. Therefore, we still need another competent approach to detect bolt looseness without constant contact of transducers, i.e., the percussion-based method. In this chapter, the author develops an analytical model to seek the working mechanism of the percussion-based approach. Then, via the audio signal processing technique and deep learning, a practical robotic-assisted percussion-based method is proposed to detect bolt looseness with promising performance.

7.1 Modeling and analysis of percussion-based method for bolt looseness detection

Overall, it is noticed that the percussion-based method has been widely used in our daily life. For instance, when buying watermelons or glasswork in the supermarket, one is used to tap them to identity the maturity (intactness) by listening the sound (generally, crisp sound means ripeness/integrity while dull sound denotes the opposite). Particularly, based on the phenomenon that the percussion-induced sound signals can reflect the changes of structural mechanical properties, the percussion-based method [266] has shown promising performance in detecting damages of engineering structures [267, 268, 269, 270]. Moreover, the sound signals have been employed to identify failures of other structures, such as induction motors [271], gearboxes [272], diesel engines [273], train bearing [274], high-power insulators [275, 276], and external rotors [277, 278]. Therefore, the potential of the percussion-based method should be explored for detecting bolt looseness.

In this subchapter, an analytical model is proposed to seek the working mechanism of the percussion-based method for bolt looseness detection. First, the virtual material method, which is derived from the fractal contact theory, is used to develop an equivalent model of bolted joint as a (three-layer) laminated plate. Then, by using the layer-wise theory (for laminated plate) and the acoustic radiation mode approach, one can model the percussion-induced sound signals of this three-layer laminated plate (i.e., the equivalent model of bolted joint). Moreover, a corresponding numerical model is developed. Finally, an experiment is performed to verify the effectiveness of the proposed analytical and numerical models. More details about the implementation of two models and the experiment can be found as follows.

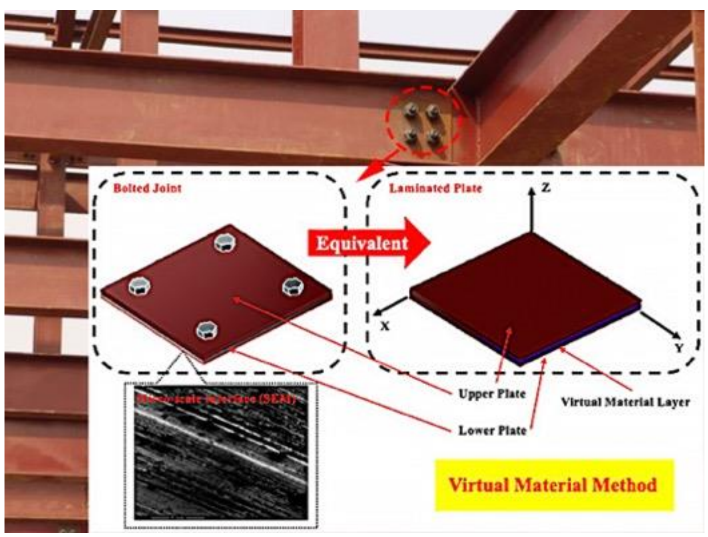

Fig. 7-1 Bolted joint and its equivalent model

Overall, the modeling of a bolted joint is a difficult task, and some attempts have been conducted, such as Iwan’s model [279]. On the other hand, the virtual material method [280] that is based on the fractal contact theory can be used to model the bolted joint as a three-layer laminated plate (i.e., the interfacial roughness is regarded as a virtual layer that is bonded between two tightened plates), as shown in Fig. 7-1. This virtual layer's elastic modules $E_{elastic}$ and shear modulus G_{shear} can be expressed as

$$\begin{cases} E_{elastic}/E' = \dfrac{2D\psi^{1\text{-}0.5D}}{3\pi^2} G^{*(1-D)} \left(\dfrac{2-D}{D} \psi^{0.5D-1} A_r^* \right)^{0.5D} \times \left[a_c^{*(-0.5)} - \left(\dfrac{2-D}{D} \psi^{0.5D-1} A_r^* \right)^{-0.5} \right] & A_r^* > A_{rc}^* \\ G_{shear}/G' = \dfrac{16\psi^{1\text{-}0.5D}}{\pi} \left[\left(\dfrac{2-D}{D} \psi^{0.5D-1} \dfrac{A_r^*}{a_c^*} \right)^{0.5D} - 1 \right] & A_r^* > A_{rc}^* \\ E_{elastic}/E' = 0; G_{shear}/G' = 0 & A_r^* < A_{rc}^* , \end{cases}$$

(7-1)

where $E_1, E_2, G_1, G_2, \mu_1, \mu_2$ are the elastic moduli, shear moduli, and Poisson ratios of two bolted plate, respectively. Moreover, $E' = E_1E_2/((1-\mu_1^2)E_2 + (1-\mu_2^2)E_1)$ and $G' = G_1G_2/((2-\mu_1)G_2 + (2-\mu_2)G_1)$ are the equivalent elastic/shear modulus, D and G ($G^* = G/\sqrt{A_a}$) are the fractal dimension and fractal roughness parameter of surface topography, A_a is the nominal contact area, ψ is the domain extension factor, $a_c^* = G^{*2}/(0.5K\phi)^{2/(D-1)}$, $\phi = \sigma_y/E'$; $K = 2.8$, σ_y is the yield strength, $A_r^* = A_r/A_a$, $A_{rc}^* = A_{rc}/A_a = DG^2\Big/\left((2-D)(0.5K\phi)^{2/(D-1)}\right)$, A_r and A_{rc} are real contact area and real critical contact area of the joint structure, respectively.

Furthermore, the relationship between A_r^* (the normalized real contact area) and the dimensionless bolt preload F^* ($F^* = F/E'A_a$) can be described as

$$F^{*}=\begin{cases}\left(2^{3-0.5D}\psi^{0.25D^{2}-D+1}/3\sqrt{\pi}(3-2D)\right)G^{*(D-1)}\left((2-D)A_{r}^{*}/D\right)^{0.5D}\cdot & \\ \left[\left((2-D)\psi^{0.5D-1}A_{r}^{*}/D\right)^{1.5-D}-a_{c}^{*(1.5-D)}\right]+ & A_{r}^{*}>A_{rc}^{*}(D\neq 1.5)\\ \psi^{0.25D^{2}-D+1}K\phi A_{r}^{*(0.5D)}\left(Da_{c}^{*}/(2-D)\right)^{1-0.5D} & \\ 2^{0.25}\psi^{0.0625}\sqrt{\frac{G^{*}}{\pi}}\left(\frac{A_{r}^{*}}{3}\right)^{0.75}\ln\frac{A_{r}^{*}}{3\psi^{0.25}a_{c}^{*}}+\psi^{0.0625}K\phi A_{r}^{*0.75}\left(3a_{c}^{*}\right)^{0.25} & A_{r}^{*}>A_{rc}^{*}(D=1.5)\\ K\phi A_{r}^{*} & A_{r}^{*}<A_{rc}^{*}\end{cases} \tag{7-2}$$

Subsequently, the properties of the virtual material can be computed as

$$h=\frac{EA_{a}}{K_{N}}\quad \mu=\frac{(1+\mu')E_{elastic}{}^{*}}{G_{shear}{}^{*}}-1\quad \rho=\frac{\rho_{1}+\rho_{2}}{2}, \tag{7-3}$$

where h is the thickness, ρ is the density, μ is the Poisson ratio, K_N is the interfacial stiffness, whose calculated method has been given in Chapter 5, $\mu'=E'/2G'-1$ is the equivalent Poisson ratio, ρ_1 and ρ_2 are densities of two plates.

After equalizing the bolted joint to a three-layer laminated plate, one can achieve the dynamic performance of the equivalent bolted joint (i.e., the laminated plate) under different preloads via several approaches, such as the Equivalent Single Layer (ESL) theory [281], Three-dimensional Elastic Theory (TDET) [282], and Layer-wise Theory (LT) [283]. In this subchapter, the LT is used to characterize the dynamic response as

$$\begin{cases}U\left(x,y,z,t\right)=\sum_{i=1}^{2n+1}u_{i}\left(x,y,t\right)\psi_{i}\left(z\right)\\ V\left(x,y,z,t\right)=\sum_{i=1}^{2n+1}v_{i}\left(x,y,t\right)\psi_{i}\left(z\right)\\ W\left(x,y,z,t\right)=\sum_{i=1}^{2n+1}w_{i}\left(x,y,t\right)\psi_{i}\left(z\right)\end{cases}, \tag{7-4}$$

where n is the total number of layers, $2n+1$ is the number of interpolation surfaces, $U(x,y,z,t), V(x,y,z,t), W(x,y,z,t)$ are displacement of laminated plate in x,y,z directions, $u_i(x,y,t), v_i(x,y,t), w_i(x,y,t)$ are the displacement of i^{th} interpolation place in x,y,z directions, $\psi_i(z)$ is the coefficient of the interpolation expansion, and it can be calculated as

$$\psi_i(z)=\begin{cases}(1-zz/h_j)/(1-2zz/h_j) & (z_{2(j-1)} \le z \le z_{2(j+1)}) \\ 4zz/h_j(1-zz/h_j) & (z_{2j-1} \le z \le z_{2j+1}) \\ -zz/h_j(1-2zz/h_j) & (z_{2j} \le z \le z_{2(j+1)})\end{cases}, \tag{7-5}$$

where $j=1,2,\cdots,n$ is the number of layers, h_j is the thickness of j^{th} layer, z_i is the coordinate value of i^{th} interpolation plane, zz is the internal plate's local coordinate.

Then, based on the finite element discretization, one can describe $u_i(x,y,t), v_i(x,y,t), w_i(x,y,t)$ as

$$\begin{aligned} u_i(x,y,t) &= \sum_{k=1}^{m} N_k(x,y)u_k T(t) \\ v_i(x,y,t) &= \sum_{k=1}^{m} N_k(x,y)v_k T(t) \\ w_i(x,y,t) &= \sum_{k=1}^{m} N_k(x,y)w_k T(t) \end{aligned}, \tag{7-6}$$

where u_k, v_k, w_k are coordinate values of k^{th} node in the x,y,z direction, $k=1,2,\cdots,m$ (m is the total number of nodes) is the number of the finite element node, $N_k(x,y)$ is the shape function, $T(t)$ is the time function. Particularly, the eight-node rectangle element is used, and thus the shape function can be expressed as

$$
\begin{cases}
N_1 = (1 - x/a)(1 - y/b)(-x/a - y/b - 1)/4 & N_5 = (1 + x/a)(1 + y/b)(x/a + y/b - 1)/4 \\
N_2 = \left[1 - (x/a)^2\right](1 - y/b)/2 & N_6 = \left[1 - (x/a)^2\right](1 + y/b)/2 \\
N_3 = (1 + x/a)(1 - y/b)(x/a - y/b - 1)/4 & N_7 = (1 - x/a)(1 + y/b)(-x/a + y/b - 1)/4 \\
N_4 = \left[1 - (y/b)^2\right](1 + x/a)\Big/2 & N_8 = \left[1 - (y/b)^2\right](1 - x/a)\Big/2
\end{cases},
$$

$$(7\text{-}7)$$

where a and b are the length and width of element. Then, the element shape function matrix $\boldsymbol{N}$ can be obtained by subsituting eqn. (7-6) and (7-7) into eqn (7-4), and the element strain matrix $\boldsymbol{B}$ can be obtained based on the displacement-strain relationship. Finally, the stiffness matrix and mass matrix of matrix can be described as

$$\boldsymbol{K} = \iiint_V \boldsymbol{B}^T \boldsymbol{SB} dxdydz \text{ ; } \boldsymbol{M} = \iiint_V \rho \boldsymbol{N}^T \boldsymbol{N} dxdydz \text{ ,} \tag{7-8}$$

where $\boldsymbol{S} = \begin{bmatrix} 1/E_1 & -\mu_{12}/E_2 & -\mu_{13}/E_3 & & & \\ -\mu_{12}/E_2 & 1/E_2 & -\mu_{23}/E_3 & & & \\ -\mu_{31}/E_1 & -\mu_{23}/E_3 & 1/E_3 & & & \\ & & & 1/G_{23} & & \\ & & & & 1/G_{31} & \\ & & & & & 1/G_{12} \end{bmatrix}$.

Therefore, by neglecting the damping of the laminated plate, one can obtain the dynamic equation of the laminated plate as

$$\boldsymbol{M}\ddot{\boldsymbol{X}} + \boldsymbol{KX} = 0 \text{.} \tag{7-9}$$

By solving the above equation, the surface normal velocity $\dot{\boldsymbol{X}}$ of the structure and natural frequency ω can be computed.

After obtaining the dynamic characteristics of the laminated plate, one can finally describe the percussion-induced sound signals of the laminated plate via the acoustic radiation mode approach. Overall, tapping the bolted joint induces the sound signals, and this procedure can be regarded as an issue of acoustic radiation of solid structures. In other words, the vibration of a solid structure due to tapping excitation can cause compressed and outspread displacement of surrounding air medium (i.e., acoustic propagation). In the past decades, to characterize this procedure of acoustic propagation, some researchers have developed two kinds of method, including the time domain analysis (e.g., wave equation [284]) and frequency domain analysis (e.g., Helmholtz equation [285]). However, some investigations have noticed that the coupling among different vibration modes have significant influence on radiated sound power. Therefore, the "acoustic radiation mode approach" [286] is adopted to decompose the structural vibration into several independent acoustic radiation modes and determine the radiated sound power via the summarization of all modes. Notably, the independence means that the decomposed radiation modes are only affected by structural size and shape, instead of boundary conditions and external excitation.

Assuming that the laminated plate (i.e., the equivalent bolted joint) is on an infinite rigid barrier (in other words, the sound only radiates to the upper free half-space) with vibration frequency ω, one can characterize the radiated acoustic power $W(\omega)$ of the structure as

$$W(\omega)=\boldsymbol{v}_n^H \boldsymbol{R} \boldsymbol{v}_n , \tag{7-10}$$

where $\boldsymbol{v}_n$ denotes the structural normal vibration velocity, n is the total number of discrete elements of the structure, H means the conjugate transpose, $\boldsymbol{R}$ is the radiated power resistance matrix, which can be expressed via the eigenvalue decomposition as

$$\boldsymbol{R} = \Phi^{\boldsymbol{H}} \Lambda \Phi \ , \tag{7-11}$$

where $\boldsymbol{\Lambda}$ is a diagonal matrix of λ_i (eigenvalues of $\boldsymbol{R}$) in descending order, Φ is a $n \times n$ matrix with volume vector $\varphi_{\boldsymbol{i}}$ (called as acoustic radiation mode), which is eigenvectors corresponding to eigenvalues λ_i. On the other hand, based on the orthogonality, $\boldsymbol{v}_n$ can be expanded as

$$\boldsymbol{v}_n = \sum_{i=1}^{n} c_i \varphi_{\boldsymbol{i}} = \Phi \boldsymbol{c} \ , \tag{7-12}$$

where c_i is the expansion coefficient of acoustic radiation mode.

Finally, using the wave superposition method, the far-field radiated sound pressure $\boldsymbol{P}$ can be obtained as

$$\boldsymbol{P} = -j\rho_0 c_0 k \boldsymbol{G} \boldsymbol{\Phi} \boldsymbol{c} \ , \tag{7-13}$$

where $\boldsymbol{P} = [P(r_1') \quad \cdots \quad P(r_k') \quad \cdots \quad P(r_n')]$, r_k' is the position vector of field space of sound; $\boldsymbol{G} = \boldsymbol{G}\left(r_i \middle| r_k'\right) = e^{-jk|r_k' - r_i|} \big/ \left(4\pi \left|r_k' - r_i\right|\right)$ is a function of the free space Green, $k = \omega / c_0$ is the wavenumber, r_i represents the position vector of equivalent acoustic source of the laminated plate, $j = \sqrt{-1}$ is imaginary. Then, based on eqn. (7-1), (7-2), (7-3), (7-9), and (7-13), the relationship between bolt preload and the radiated sound pressure can be developed.

Furthermore, as shown in Fig. 7-2, a numerical model is constructed to partially verify the proposed analytical modeling of the percussion-based method for bolt looseness detection. A 3D model of the bolted joint (4×M10, tightened plate: 150 mm×150 mm×5 mm) is placed on an infinite rigid baffle. The material properties of steel plate and air are given in Table 7-1. Particularly, the interfacial roughness of the bolted joint is taken into consideration, and the detailed procedure has been introduced and discussed in subchapter 3.3.

Table 7-1 Material properties

Material	Properties	Value
Steel	Elasticity modulus	209 GPa
	Poisson ratio	0.3
	Density	7860 kg m-3
	Yield stress	355 MPa
Air	Density	1.19 kg m-3
	Sound speed	343 m s-1

Then, this numerical simulation is implemented via the COMSOL, which is a widely used commercial FEM software. To simulate the properties of the percussion-induced sound signals, two embedded modules in the COMSOL (solid mechanics and the acoustic) are employed. Particularly, the default acoustic-solid interaction (frequency domain Multiphysics coupling) in COMSOL is used to define the boundary coupling features between the air and structure. The tapping point is on the steel plate, and the mimic of tapping is implemented via a sine pulse, as shown in Fig. 7-2. It is worth noting that the amplitude and duration time of the tapping. Furthermore, a hemispheric-shaped air domain (i.e., perfectly matched layer, PML [287]) is used to extrapolate the far field of sound with thickness of 0.1m. The radius of PML is 0.5 m. Finally, the sound pressure level at the interface between air domain and PML domain is simulated via a reference of 20 μPa. All elements in the proposed simulation model are meshed by tetrahedral mesh, and the maximum size is set to one-sixth of acoustic wavelength to ensure accuracy.

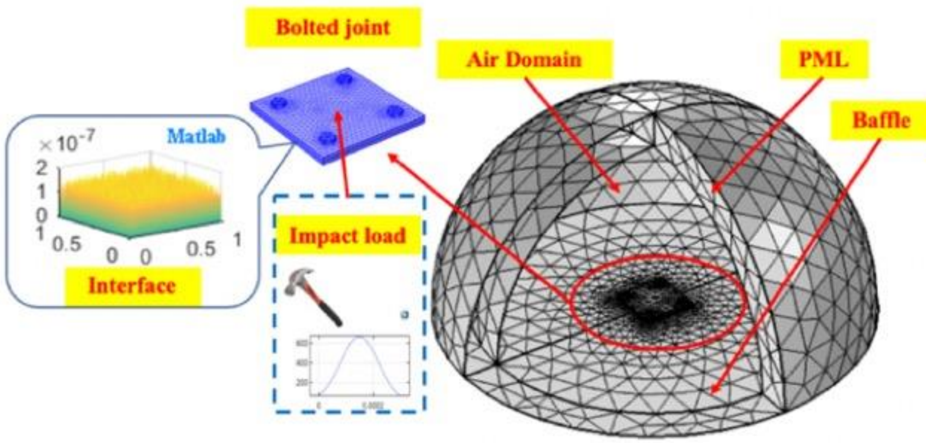

Fig. 7-2 Finite element modeling of percussion-based method for bolt looseness detection

Finally, to verify the effectiveness of the proposed analytical model (also the numerical model), the author performs an experiment, whose apparatus is depicted in Fig. 7-3 [288]. Four different degrees of bolt preload (0 Nm, 20 Nm, 40 Nm, and 60 Nm) are selected. All setup is the same as the numerical simulation, and a microphone (CAD 179-type, frequency response: 100 Hz-20 kHz) is placed at 0.5 m from the impact point (steel plate) to record the percussion-induced sound signals with sampling frequency of 48 kHz. Then, an impact hammer (PCB 086C03) with NI DAQ system (NI type USB-6366) is utilized to implement the percussion; particularly, the NI DAQ system is used to obtain the amplitude and duration time of the impact force. For the experimental signals, the background noise is extracted, and a high-pass filter was used to eliminate other noise signals. Moreover, for all analytical, numerical, and experimental sound signals, an A-weight acoustic filter is applied, and the Fast Fourier Transform (FFT, nfft points: 32, 768) is employed to process and identify the frequency response of sound signals.

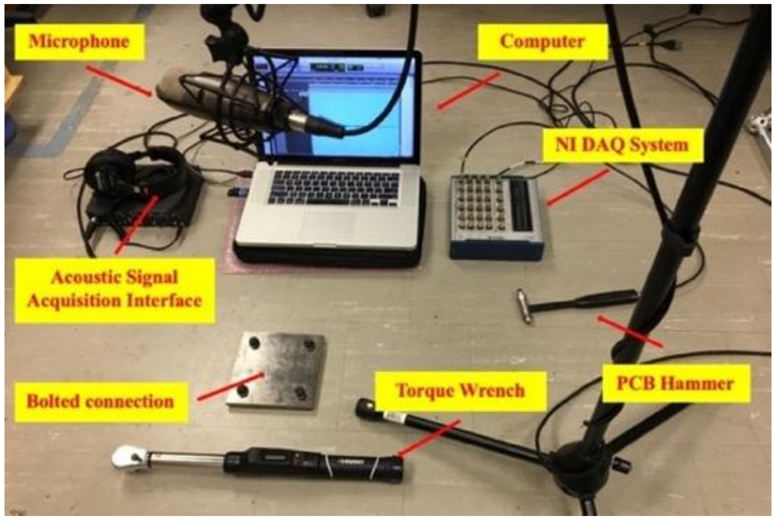

Fig. 7-3 Experimental setup

On the other hand, the surface roughness of the bolted joint is measured by a three-dimensional (3D) surface roughness profiler (Zygo, ZeGage, USA), as shown in Fig. 7-4. The fractal dimension and the fractal roughness parameter are calculated as $D = 1.26$, $G = 2.15\times10^{-12}$ m (more detailed computation procedure has been given in subchapter 3.1).

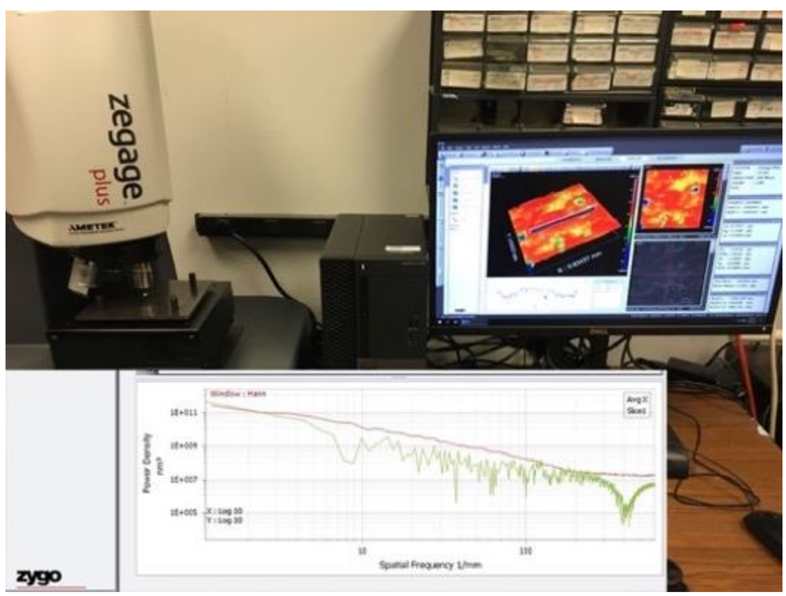

Fig. 7-4 Surface profiler with measured topography

According to the calculated fractal dimension and the fractal roughness parameter, the properties of the virtual material under different preloads can be obtained, and the results are given in Table 7-2.

Table 7-2 Properties of virtual material under different bolt preloads

Material	Preload			
	0 Nm	20 Nm	40 Nm	60 Nm
Elasticity modulus/ GPa	0	0.41	0.66	0.74
shear modulus/ GPa	0	0.15	0.31	0.42
Density/ kg m-3	7860	7860	7860	7860
Poisson ratio	0	0.20	0.22	0.24
Thickness/ mm	0	0.16	0.21	0.24

Subsequently, the analytical solutions, simulation results, and experimental values (in decibels, dB) under different preloads are compared in Fig. 7-5, which indicates that the tendency of the analytical solutions, simulation results, and experimental values has common (not good) consistency. This phenomenon is similar to the previous investigations [289], and it may be explained due to the simplifications and assumptions of analytical and numerical modeling. Moreover, the peak values can be used as an index to indicate the bolt looseness, and it increases with larger preload. Then, it is noticed that the differences of spectrum (particularly the peak value) between 40 Nm and 60 Nm is smaller than other cases. This phenomenon can be attributed to the saturation of the true contact area under overlarge preload, which has been discussed in subchapter 3.2. Finally, the comparison of the analytical solutions, simulation results, and experimental values (peak value) are given in Table 7-3, which can demonstrate the effectiveness of the proposed analytical and numerical modeling. Moreover, as shown in Table 7-4, the correlation coefficients between the analytical solutions and the experimental values under different preloads are within the range of 0.6-0.8 (which means the strong correlation), and the simulation results under different preloads has the moderate correlation with the experimental values, since the correlation coefficients are between 0.4 and 0.6. Overall, the results in Table 7-3 and 7-4 can confirm the effectiveness of the proposed analytical and numerical model, i.e., the working mechanism of the percussion-based method for bolt looseness detection.

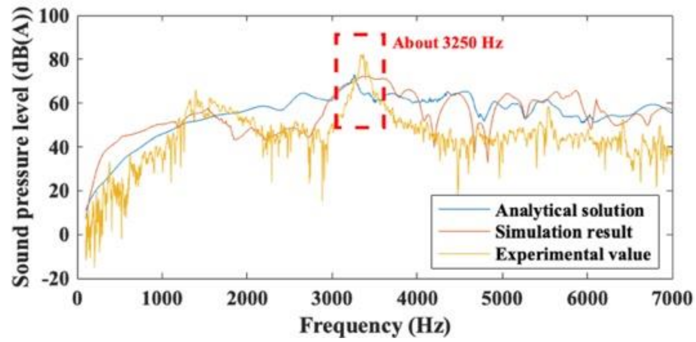

(a) 0 Nm

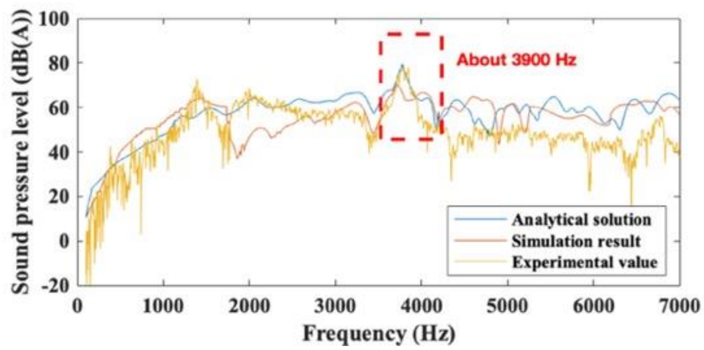

(b) 20 Nm

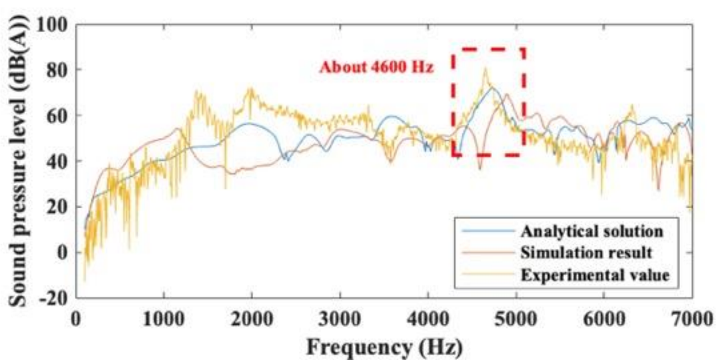

(c) 40 Nm

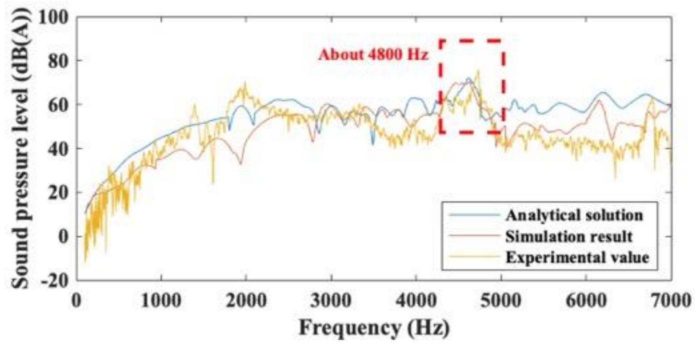

(d) 60 Nm

Fig. 7-5 Comparison of three kinds of results (in spectrum) under different preloads

Table 7-3 Comparison results among three results under different preloads

Preload	Experimental value (Hz)	Analytical solution (Hz)	Error	Simulation result (Hz)	Error
0 Nm	3350	3260	2.7%	3390	1.2%
20 Nm	3900	3780	3.1%	3820	2.1%
40 Nm	4654	4730	1.6%	4890	5.1%
60 Nm	4800	4660	2.9%	4700	2.1%

Table 7-4 Similarity analysis between analytical solutions/simulation results and experimental values under different preloads

Preload	Analytical solution	Simulation result
0 Nm	0.7534	0.6081
20 Nm	0.6276	0.5312
40 Nm	0.6505	0.4087
60 Nm	0.6338	0.5203

7.2 Practical robotic-assisted percussion-based method for bolt looseness detection

The last subchapter researches the working mechanism of the percussion-based method. However, it is noticed that the frequency domain features may be not suitable for industrial application (since the sensitive may be incapable of detecting multi-bolt looseness). Moreover, the current percussion-based method is implemented manually, which is hard to achieve for some complex cases (e.g., high-rise truss/space structures). As illustrated in Fig. 7-6 [290], a climbing robot that equips with a robotic arm, a hammer, and a microphone can address the problem of the bolt looseness detection of the space structure. Therefore, in this subchapter, a more practical percussion-based method is developed. First, the robotic arm and hammer is used to implement the tapping, i.e., no manual percussion is required. Then, rather than frequency domain features, the proposed practical percussion-based method employs the Mel-frequency cepstrum (MFCC) [291] and memory-augmented neural network (MANN) [292] to achieve the extraction and classification of percussion-induced sound signals to detect multi-bolt looseness.

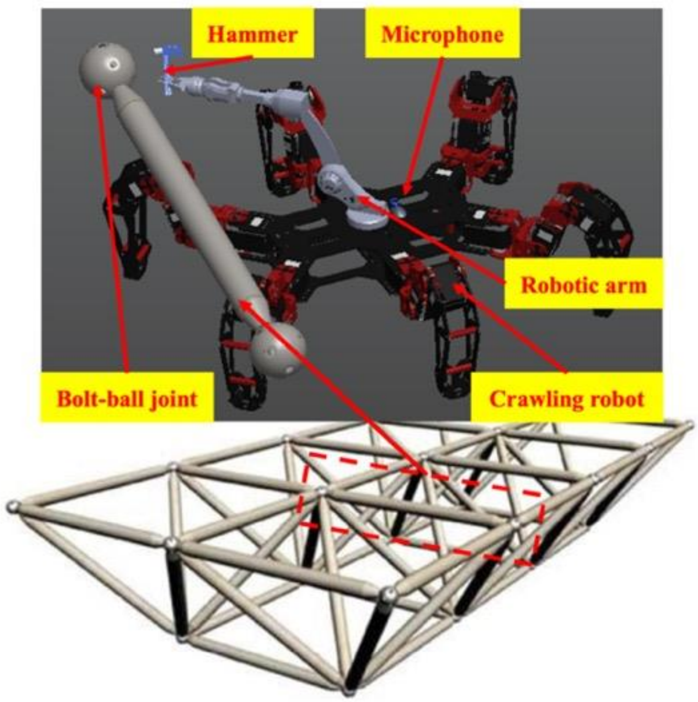

Fig. 7-6 Schematic of robotic-assisted detection of spatial bolt-ball joint looseness

The overall flowchart of the proposed practical percussion-based method is illustrated in Fig. 7-7 [290]. After the pre-processing, the time-frequency representation of the percussion-induced sound signals (under different cases of bolt integrities) via MFCC is obtained. Then, by normalizing and graying the MFCC matrices, the training and testing datasets are generated. The training dataset is imported into MANN to train the classifier, and the testing dataset is used to verify the performance of the classifier.

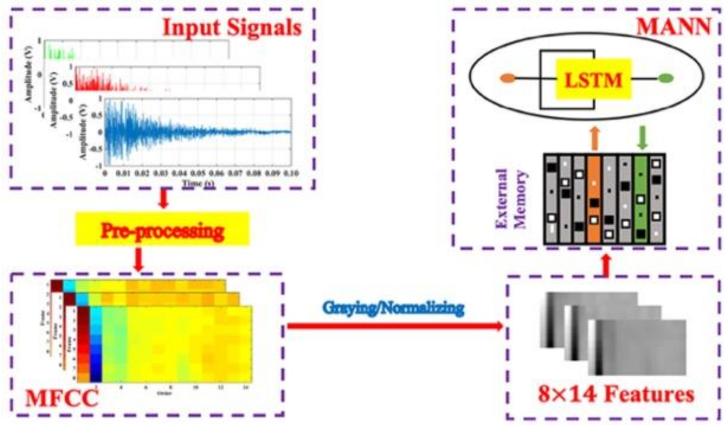

Fig. 7-7 Flowchart of the proposed practical percussion-based method

The reason to use MFCC to process the percussion-induced sound signals is that the input for MANN is 2D instead of 1D. In other words, MFCC can extend 1D sound signals to 2D matrices (time-frequency domain features). Moreover, this extension reduces the dimensionality, which dramatically improves the training efficiency. The procedure of MFCC is depicted in Fig 7-8.

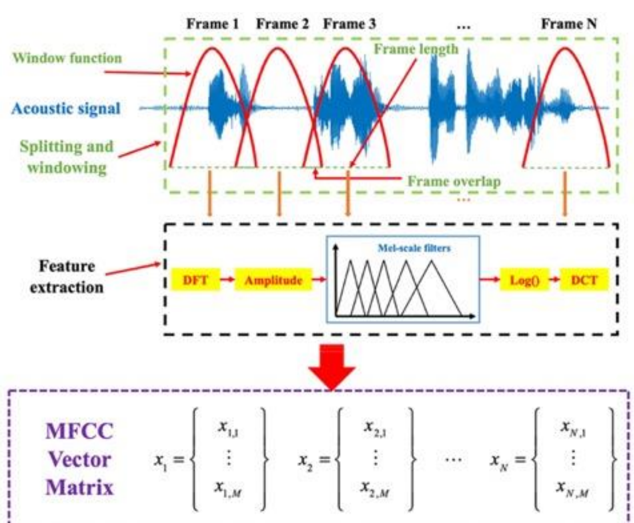

Fig. 7-8 Flowchart of the MFCC feature extraction and computation process

The detailed steps for MFCC are given as follows:

(1) First employ a Hamming window to segment the sound signal $x(n)$.

(2) Then, the discrete Fourier transform (DFT) is used to compute the power spectrum of sound signals as

$$x(k)=\sum_{n=0}^{M_s-1} x(n)e^{-j2\pi nm/M_s}\ , \tag{7-14}$$

where $0 \le k \le M_s$, and M_s is the total points for the DFT, k is the parameter for M_s.

(3) Subsequently, the frequency in Hertz scale is converted to Mel scale by using a filter bank that includes some triangular filters, and the response $H_i(k)$ of *ith* filter can be expressed as

$$H_i(k)=\begin{cases} 0 & k<k_{b_i-1} \\ \dfrac{k-k_{b_i-1}}{k_{b_i}-k_{b_i-1}} & k_{b_i-1}\le k\le k_{b_i} \\ \dfrac{k_{b_i+1}-k}{k_{b_i+1}-k_{b_i}} & k_{b_i}\le k\le k_{b_i+1} \\ 0 & k>k_{b_i+1} \end{cases}\ , \tag{7-15}$$

$$k_{b_i}=\left(M_s/F_s\right) f_{mel}^{-1}\left[f_{mel}(f_{\min})+i\left\{ f_{mel}(f_{\max})-f_{mel}(f_{\min})\right\}/(Q+1)\right]$$

where k_{b_i} is the value of filter's boundary, Q is the total number of filters, $f_{\max}$ and $f_{\min}$ are the maximum and minimum of the frequency range.

(4) According to O'Shaughnessy's theory, one can compute the frequency in Mel scale f_{mel} and its inverse f_{mel}^{-1} as

$$\begin{cases} f_{mel}=2595\times\log_{10}\left(1+\dfrac{f}{700}\right) \\ f_{mel}^{-1}=700\left(10^{f_{mel}/2595}-1\right) \end{cases}. \tag{7-16}$$

(5) Finally, the MFCC coefficients $c(n)$ can be obtained by calculating the energy spectrum $s(i)$ of the filter bank through the discrete cosine transform (DCT) as

$$
\begin{cases}
c(n) = \sum_{i=0}^{Q-1} s(i) \cos\left(\frac{n(i-0.5)}{Q} \pi \right) \\
s(i) = \ln\left[\sum_{k=0}^{Q-1} \left| x(k) \right|^2 H_i(k) \right]
\end{cases} . \tag{7-17}
$$

In fact, MFCC has been widely used in automatic speech recognition (ASR), i.e., sound signal processing. Particularly, with the rapid development of deep learning technique, the convolutional neural network (CNN) has been applied to extract features from MFCC and implement classification. Compared to the current methods for ASR such as the hidden Markov models (HMMs), the Gaussian mixture models (GMMs), and their combination (i.e., the GMM-HMMs), the MFCC+CNN can achieve better performance and attract a lot of attention. For instance, a CNN-MFCC hybrid model [293] and a Label-Tree Embeddings (LTE) algorithm [294] was proposed to employ CNN to capture MFCC features and achieve audio scene classification, and many similar investigations have also demonstrated the capacity of MFCC+CNN. However, it is noticed that an issue limits the further application of CNN+MFCC, i.e., CNN requires extensive data to train the classifier and it needs to relearn the inherent parameters for classification when new data is encountered. In other words, the classifier can assimilate the small quantity of input rapidly and generate a promise classification based on the inference from a new scrap of information. Thus, in this subchapter, the author employs MANN, which is derived from Neural Turing Machines (NTMs) and memory networks, to replace CNN for the extraction and classification of MFCC features. Moreover, the advantages pf MANN have been demonstrated in the previous investigation.

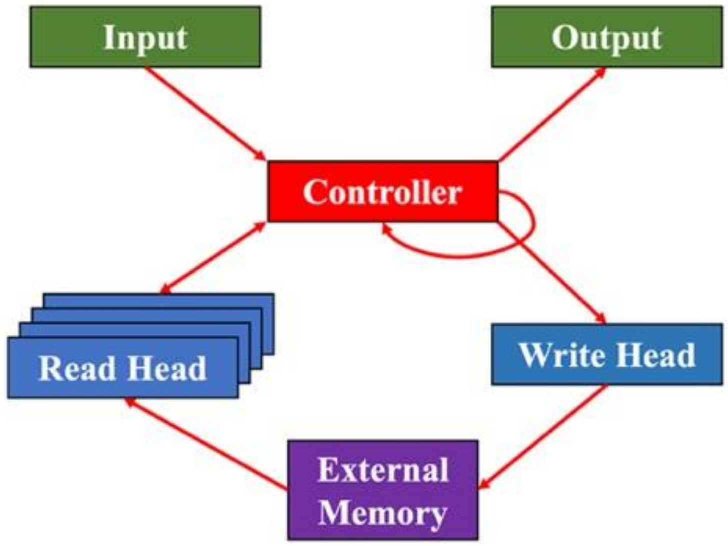

Fig. 7-9 The architecture of the MANN

As shown in Fig. 7-9, MANN has a controller that is long short-term memory (LSTM) network, an external memory, and several read/write heads. The working mechanism of MANN is described as follows.

(1) With the input data (x_t, y_{t-1}), the LSTM controller can update the state as

$$\hat{g}^f, \hat{g}^i, \hat{g}^o, \hat{\mathbf{u}} = \mathbf{W}^{xh}(x_t, y_{t-1}) + \mathbf{W}^{hh}\mathbf{h}_{t-1} + \mathbf{b}^h, \tag{7-18}$$

where $\hat{g}^f, \hat{g}^i, \hat{g}^o$ are the forget gate, input gate, and output gate, respectively; $\mathbf{W}^{xh}(x_t, y_{t-1})$ denotes the weight transformation from the input (x_t, y_{t-1}) to the hidden state, $\mathbf{W}^{hh}$ represents the weight transformation between two different hidden states, $\mathbf{h}_{t-1}$ is the hidden state with label y_{t-1}, $\mathbf{b}^h$ is the bias of the hidden state.

(2) Then, the concatenated output of the controller can be expressed as

$$\mathbf{o}_t = (\mathbf{h}_t, \mathbf{r}_t), \tag{7-19}$$

where $\mathbf{h}_t = \sigma(\hat{g}^o) \odot \tanh(\mathbf{c}_t)$ is the hidden state with label y_t, $\mathbf{c}_t = \sigma(\hat{g}^f) \odot \mathbf{c}_{t-1} + \sigma(\hat{g}^i) \odot \tanh(\hat{\mathbf{u}})$ is the cell state, $\mathbf{r}_t$ is the read vector under the external memory $\mathbf{M}_t$, σ() represents the sigmoid function.

(3) Particularly, the read vector $\mathbf{r}_t$ can be retrieved by using the read weight vector as

$$\begin{gathered}\mathbf{r}_t \leftarrow \sum_i w_t^r(i)\mathbf{M}_t(i) \\ w_t^r(i) \leftarrow \frac{\exp(K(k_t, \mathbf{M}_t(i)))}{\sum_j \exp(K(k_t, \mathbf{M}_t(j)))}\end{gathered}, \tag{7-20}$$

where $K(k_t, \mathbf{M}_t(i)) = \mathbf{k}_t \cdot \mathbf{M}_t(i) / \|\mathbf{k}_t\| \|\mathbf{M}_t(i)\|$ is the cosine distance between the query key vector and each row of $\mathbf{M}_t$. Similarly, Least Recently Used Access (LRUA) [292] is employed to implement memory write function.

(4) Finally, one can compute the output distribution, i.e., the classification probability $\mathbf{p}_t$ as

$$p_t(i) \leftarrow \frac{\exp(\mathbf{W}^{op}(i)\mathbf{o}_t)}{\sum_j \exp(\mathbf{W}^{op}(i)\mathbf{o}_t)}, \tag{7-21}$$

where $\mathbf{W}^{op}$ is the output weight, and the episode loss $\mathcal{L}(\theta)$ can be obtained through

$$\mathcal{L}(\theta) = -\sum_t y_t^T \log \mathbf{p}_t \ . \tag{7-22}$$

After introducing the MFCC and MANN, the author performs an experiment to verify the effectiveness of the proposed practical percussion-based method. A 6-bay, 83-member spatial truss structure connected by bolt-ball joint (size: 0.35 m of length, 0.35 m of width, and 2.1 m of height) is used to provide different scenarios of bolt looseness. The experimental apparatus includes a robotic arm with control handle (OWI-535, OWI Robotic), which can be used to implement the robotic-assisted percussion. Particularly, a special hammer, which consists of a copper ball and a steel spring, is designed to simulate the “tapping”. It is worth noting that the tapping point is on the ball joint, while no accurate position can be ensured (due to spring). This design is preferred since the same tapping position cannot always be ensured in the real implementation. Moreover, as shown in Fig. 7-10, a microphone (Ambeo VR, Sennheiser) and an acoustic signal acquisition interface (Scarlett 18i8, Focusrite) are used to capture and save the percussion-induced sound signals. The distance between the microphone and the tapping position is about 0.2 m, and the sampling rate and time are set to 48 kHz and 0.1 second, respectively.

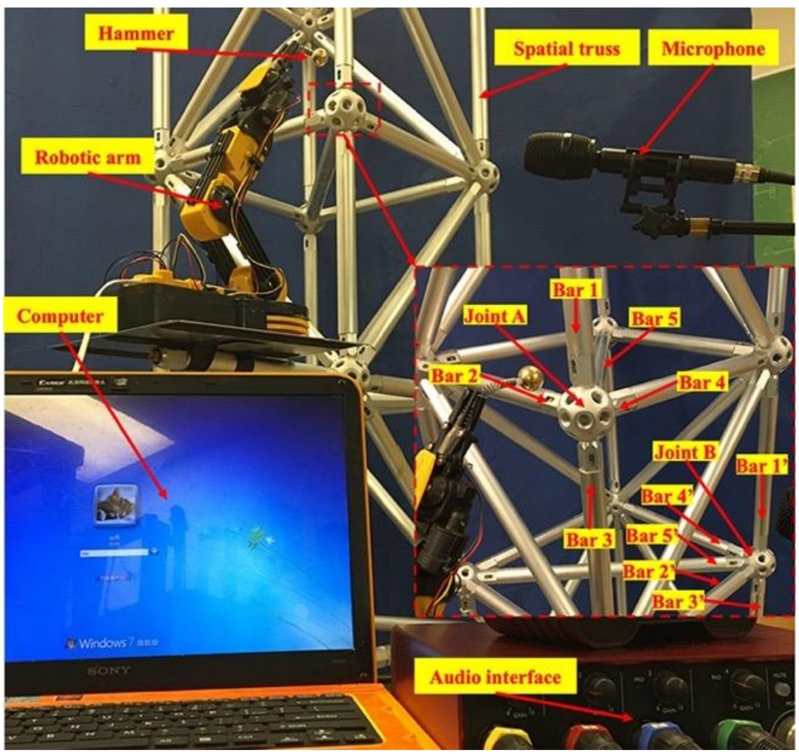

Fig. 7-10 Experimental setup

The details of different scenarios of bolt looseness are given in Table 7-5. It is worth noting that both single-bolt and multi-bolt looseness are investigated. Particularly, two joints are used (Joint B in Case 7) to demonstrate the capacity of MANN. For Case

1 to 6, the percussion is repeated 100 times to construct dataset, which can be divided into two parts: 80% for training and 20% for testing (i.e., 480 training samples and 120 testing samples). Then, in terms of Case 7, the testing dataset has 20 samples, and the numbers of training dataset are set to 2, 4, 6, 8, and 10, respectively.

Table 7-5 Details of different experimental scenarios

Case	Joint	Looseness	Tightened (20 Nm)
1	A	N/A	Bar 1, 2, 3, 4, and 5
2		Bar 1 (10 Nm)	Bar 2, 3, 4, and 5
3		Bar 1 (0 Nm)	Bar 2, 3, 4, and 5
4		Bar 1 and 2 (0 Nm)	Bar 3, 4, and 5
5		Bar 1, 2 and 3 (0 Nm)	Bar 4 and 5
6		Bar 1, 2, 3 and 4 (0 Nm)	Bar 5
7	B	Corresponding to cases 1-6	

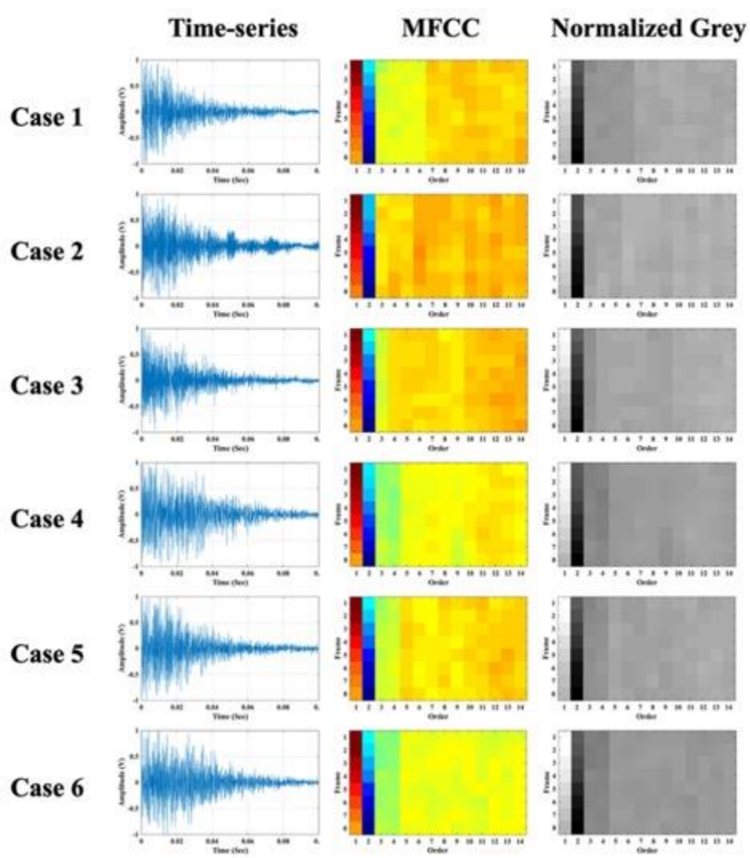

Fig. 7-11 Samples of sound signal and MFCC features under different cases

The received percussion-induced sound signals, corresponding MFCC matrices (size: 8×14) and normalized/grey matrices are depicted in Fig. 7-11. Then, the normalized/grey matrices are fed into MANN model, which is constructed and achieved on the TensorFlow framework. Based on random translation and rotation of inputs (i.e., normalized/grey MFCC matrices), the data augmentation was achieved, and the ADAM (adaptive moment estimation) optimizer was employed to train the MANN. In this paper, a grid search was implemented to figure out the best values of parameters as external memory size: 128×40; LSTM controller size: 200; the learning rate: 1e-4, the number of reads from memory is 4 (with write decay of 0.99); feedback instance: 10, and the batch size: 32. Moreover, a GPU (graphics processing unit, Nvidia GTX 960) was used to improve efficiency. Subsequently, to verify the effectiveness of the MANN, its classification accuracies were computed with maximum episodes of 100, 000, as depicted in Fig. 7-12.

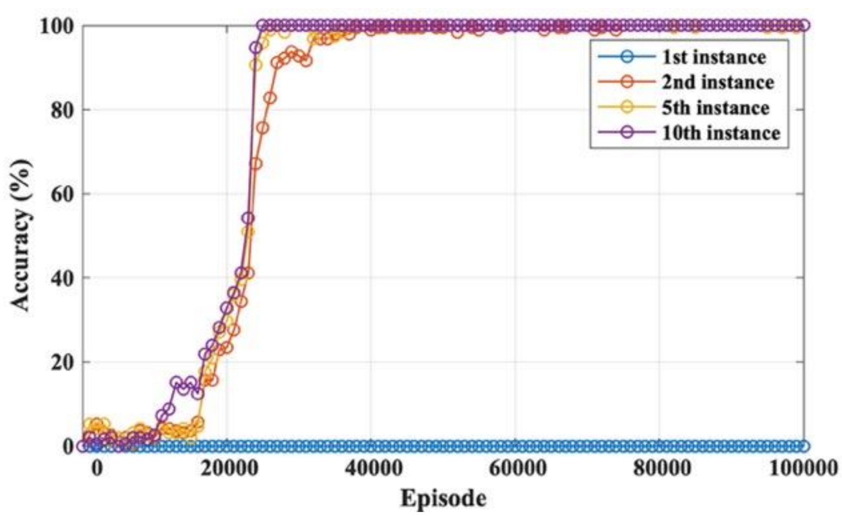

Fig. 7-12 Testing accuracies under different Cases (1-6) using the MANN

It is observed that the testing accuracy can achieve 100% after 25,000 episodes under the tenth feedback, and the performance of the proposed percussion-based method is compared with several methods, including current percussion-based methods [295, 296, 297] and CNN+MFCC. The results are given in Table 7-6. It can be seen that the MFCC+MANN achieve the best performance, which preliminarily demonstrates the effectiveness of the proposed practical percussion-based method.

Table 7-6 Comparison of testing classification accuracies between the proposed method and current methods

Model	Instance (% Accuracy)
PSD+DT [295]	66.67
MFCC+SVM [296]	92.17
IME+BPNN [297]	81.33
MFCC+CNN	99.17
MFCC+MANN	**100.00**

Then, the anti-nosing performance of the proposed percussion-based method is tested by adding white Gaussian noise into input. To quantify the influence of noise, an index, i.e., signal-to-noise (SNR) ratio is used and is expressed as

$$\mathrm{SNR}_{dB} = 10\log_{10}\left(\frac{A_{\text{signal}}^2}{A_{\text{noise}}^2}\right), \tag{7-23}$$

where A_{signal} and A_{noise} are the amplitude of the signal and noise, respectively.

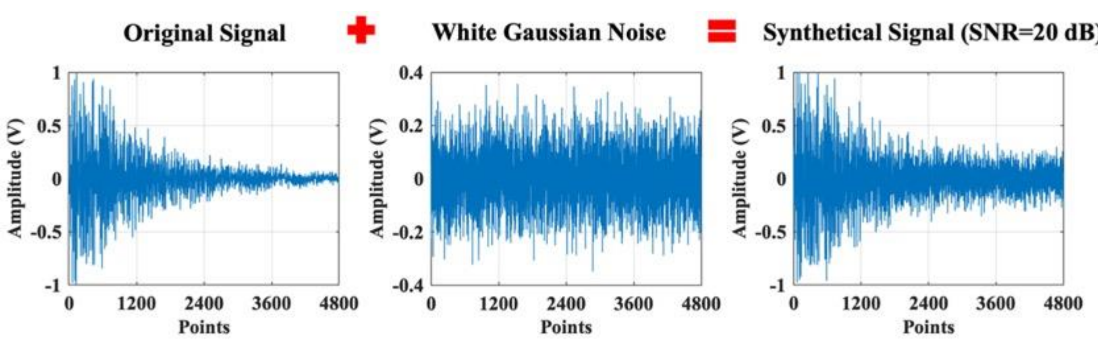

Fig. 7-13 Illustration of the adding noise process (under the case of SNR= 20dB)

The illustration of adding noise into sound signal is given in Fig. 7-13. In this subchapter, four different levels of noise (20 dB, 40 dB, 60 dB, and 80 dB) are selected. Then, the results of the proposed percussion-based method and other four baseline methods are compared in Fig. 7-14, which depicts that the proposed percussion-based method still achieve the best performance. Thus, the anti-nosing capacity of the proposed percussion-based method is verified.

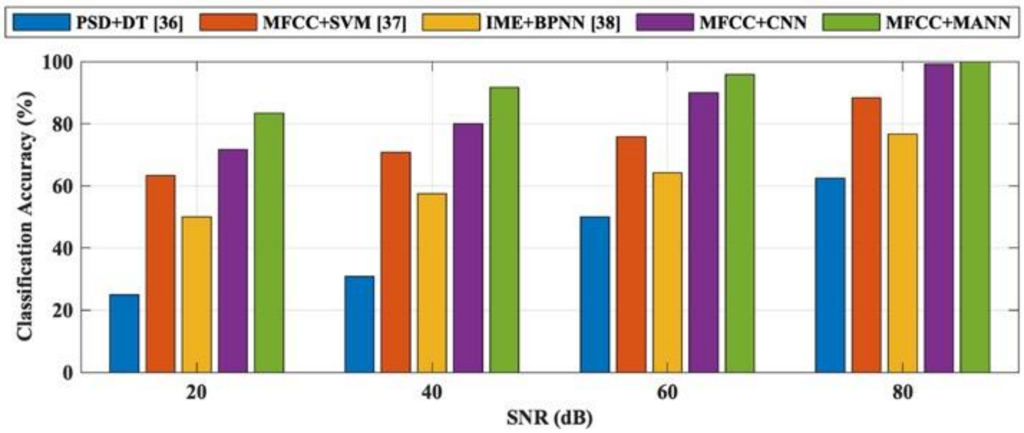

Fig. 7-14 Classification accuracy among different methods

Finally, to demonstrate the effectiveness of MANN, the experiment under Case 7 is conducted. In other words, scenarios of Case 1-6 are repeated at Joint B to construct new training dataset and testing dataset. It is worth noting that the new training dataset is just used to amend the well-trained model (via Joint A) to achieve promising classification accuracy. For instance, after conducting the experiment of Case 7, the trained MANN and CNN classifiers via Joint A are used to assimilate several (2, 4, 6, 8, and 10) training samples form Joint B for adaptation. Then, the classifiers are tested by the testing data (total number: 120) from Joint B, and the results are given in Fig. 7-15, which confirms that MANN outperforms CNN, indicating that MANN may have more potential for the future applications. Overall, according to the above three comparisons, it is clear that the proposed practical percussion-based method shows promising performance, and its application in the real industries can be expected.

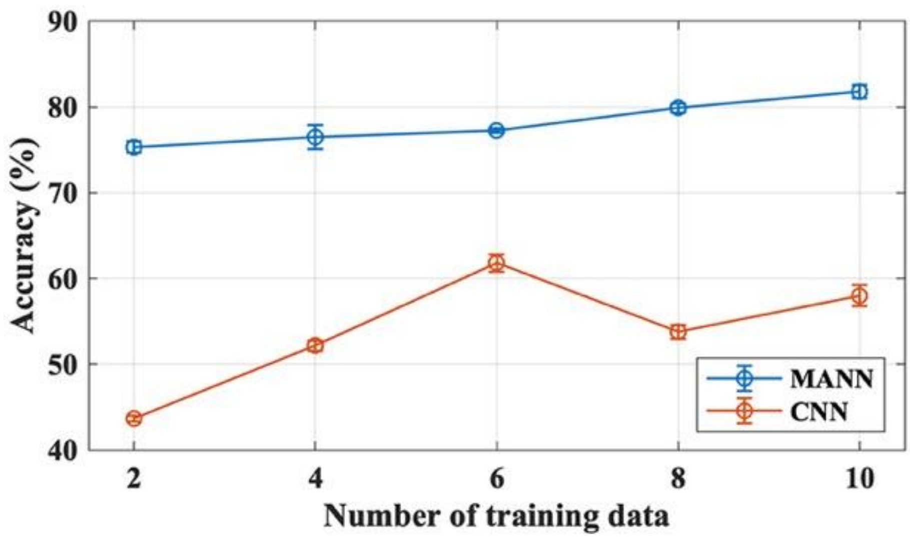

Fig. 7-15 Testing accuracies under case 7 using the MANN and the CNN

7.3 Percussion-based method for bolt looseness detection via one-dimensional memory-augmented convolutional neural network

The last subchapter employed the voice recognition technique (MFCC) and DL-based techniuqe to achieve bolt looseness detection practically. However, it is presupposed that MFCC is a promising feature for bolt looseness. Such a hand-crafted feature (e.g., MFCC) may miss some discriminative characteristics of the percussion-induced sound signals, leading to unsatisfactory classification performance in some cases. Therefore, in this subchapter, the author further employs the capacity of DL, which can fuse the feature extraction and recognition (a.k.a., classification) into one frame. In other words, instead of any extracted features such as MFCC, the percussion-induced sound signals are fed into a DL-based classifier to avoid the hand-crafted features and inefficient postprocessing, thus achieving better classification accuracy. Particularly, based on CNN and MANN (which has been introduced in the last subchapter), a new DL-based classifier, i.e., one-dimensional memory-augmented convolutional neural network (1D-MACNN) is proposed.

The schematic of the proposed 1D-MACNN and the detailed architecture [298] are given in Fig. 7-16 and Table 7-7, respectively. The 1D-MACNN consists of one 1D convolutional (Conv) layer, one max-pooling (M-p) layer, one MANN layer, one fully-connected (FC) layer with activation function of softmax. Since MANN has been introduced in the last subchapter, the mechanism of convolutional layer and max-pooling layer is only briefly descriped in this subchapter.

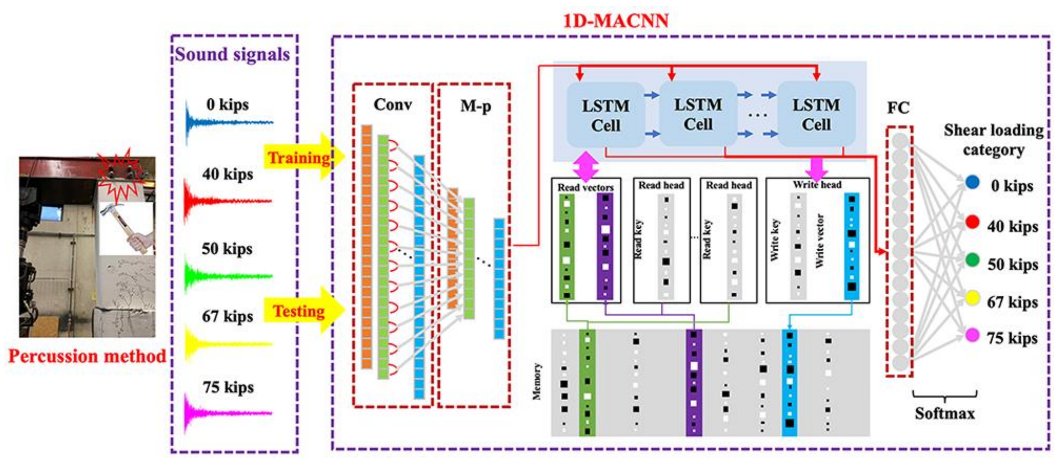

Fig. 7-16 Schematic of the proposed 1D-MACNN

Table 7-7 Architecture of the proposed 1D-MACNN

Layer	Name	Details
1	Conv	filters=32, kernel size=64×1, strides=16, activation='ReLU', padding='same'
2	M-p	kernel size=2×1, strides=1, padding='valid'
3	MANN	LSTM units=100, memory size=40×20, read heads=4, write heads=1
4	Fully-Connected	units=5, activation='softmax'

Overall, spatially local connectivity and weight-sharing are two essential properties of the convolutional layer, since they can enable the function of learning kernels. In other words, the convolutional layer can be regarded as a local feature extractor that can produce a feature map between input and kernel, and the procedure of this extraction can be described as

$$
\boldsymbol{y}_k^{l+1} = \sum_i \boldsymbol{K}_{ik}^l \otimes \boldsymbol{x}_i^l + \boldsymbol{b}_k^l, \tag{7-24}
$$

where $\boldsymbol{y}_k^{l+1}$ is denoted as the input of k^{th} neuron at layer $l+1$, $\boldsymbol{K}_{ik}^l$ is defined as the kernel from i^{th} neuron at layer l to the k^{th} neuron at layer $l+1$, $\boldsymbol{x}_i^l$ is the output of i^{th} neuron at layer l, $\otimes$ represents the convolution computation, $\boldsymbol{b}_k^l$ is the bias of the k^{th} neuron at layer $l+1$.

The Rectified Linear Unit (ReLU) is employed as the activation layer after the convolutional layer, to improve the divisibility of extracted features and accelerate the convergence. The implementation of ReLU can be expressed as

$$
\boldsymbol{a}_k^{l+1} = f(\boldsymbol{y}_k^{l+1}) = \max\{0, \boldsymbol{y}_k^{l+1}\}, \tag{7-25}
$$

where $\boldsymbol{a}_k^{l+1}$ is the activation of $\boldsymbol{y}_k^{l+1}$.

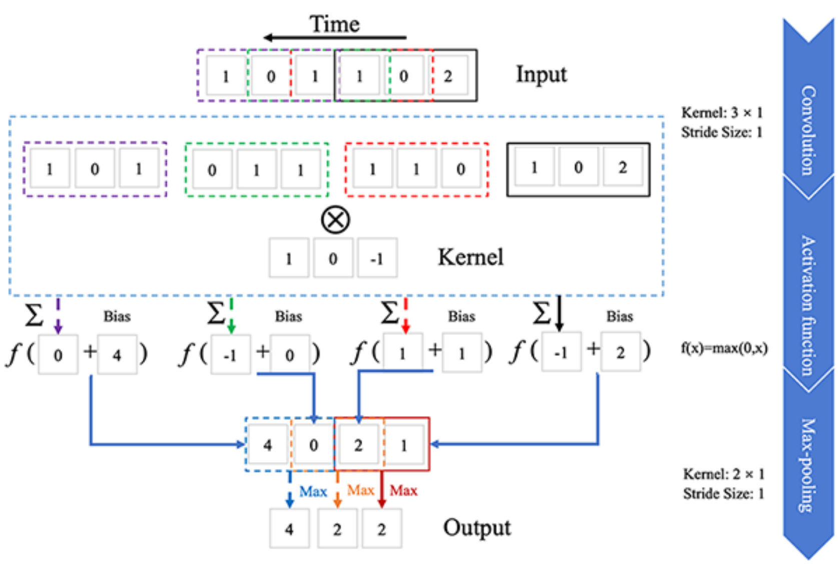

Fig. 7-17 Demonstration of the 1D convolution, ReLU, and max pooling

The max-pooling layer (the most common pooling layer) is used to condense features and improve computational efficiency. Generally, its working mechanism is to only output the maximum number in each sub-region. The author illustrates the implementation of the 1D convolution, ReLU, and max pooling in Fig. 7-17. Moreover, the batch normalization (BN) layer was used between convolutional layer and max-pooling layer to normalize the features extracted through the convolutional layer, thus improving the performance and stability of networks.

Subsequently, the training process of the proposed 1D-MACNN, which is similar to MANN model, can be described as follows: (1) a $t(t=1,2,\cdots,T)$ time sequence $\boldsymbol{x}_i$ with one-hot time off-set labels $\boldsymbol{y}_{t-1}$ (i.e., the input has the form as $(x_1, null),(x_2, y_1),\cdots,(x_T, y_{T-1})$) works as the input of 1D-MACNN, (2) Under each time step, the 1D-CNN layer and 1D max-pooling layer are used to extract features from input to construct new input $\mathbf{X}_t$, which will be ded into the MANN layer, (3) Then, using the new input and label, the MANN layer can output $\boldsymbol{o}_t$, (4) $\boldsymbol{o}_t$ is then passed to the FC layer to produce a vector of class probabilities $\boldsymbol{p}_t$, (5) finally, 1D-MACNN model will minimize the following loss function to implement the training process as

$$L(\theta) = -\sum_t \boldsymbol{y}_t \log \mathbf{p}_t, \tag{7-26}$$

where $\boldsymbol{y}_t$ is the target label at time t.

To verify the proposed 1D-MACNN, the author conducted an experiment under laboratory conditions on a reinforced concrete (RC) column, whose top was connected to the loading device via a steel box beam, as depicted in Fig. 7-18. Moreover, the drawing of specimen is given in Fig. 7-19. Four M28 through-bolts are used to hold the connection between the steel box beam and the RC column, which are denoted as TL, TR, BL, and BR, respectively. Five different shear loading (0 kips, 40 kips, 50 kips, 67 kips, and 75 kips) are applied to these bolts by driving the device. For each bolt, a hammer is used to tap it 150 times under five levels of shear loading. In other words, there is a total of 3000 (150×4×5) samples, and a smartphone (iPhone 6s), which is about 300 mm from the nut, records these percussion-induced sound signals with a sampling frequency of 48,000 Hz. Finally, these audio signals would be utilized as training and testing datasets for the proposed 1D-MACNN to achieve the shear loading detection of through-bolts.

Fig. 7-18 Experimental apparatus

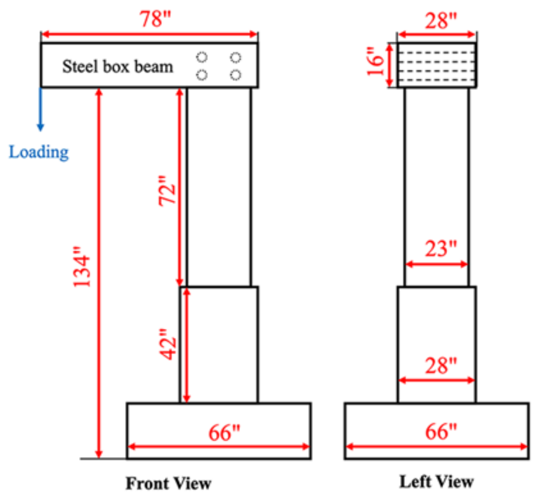

Fig. 7-19 Drawing of specimen (unit: inch)

In terms of recorded percussion-induced audio signals, the signals are first preprocessed by normalization and down-sampling (frequency: 10, 240 Hz), and then the signals are clipped with a duration of 0.4 second (i.e., each sample has 10240×0.4= 4, 096 points). Fig. 7-20 illustrates the signals under different shear loading when tapping the TL through-bolt.

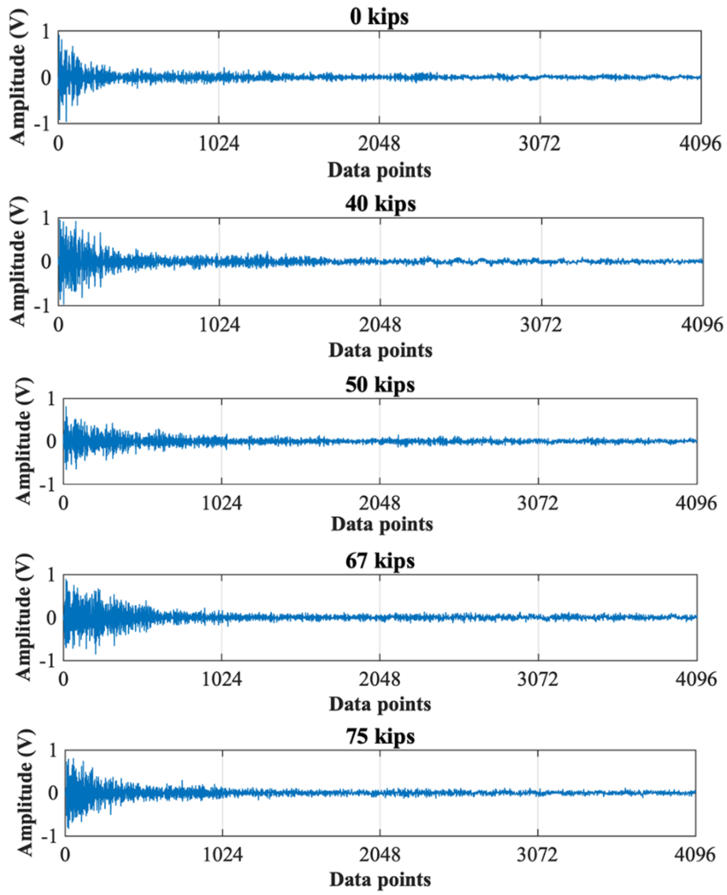

Fig. 7-20 Percussion-induced sound signals under different shear loading (through-bolt: TL)

For each through-bolt (i.e., TL, TR, BL, and BR), 120 from 150 signals under each shear loading (i.e., class/category) are randomly selected to construct the training dataset (120×5×4 = 2400), and the remaining data (30×5×4 = 600) worked as the testing set. The training procedure is the same as the implementation in subchapter 7.2, and the training and testing processes of the 1D-MACNN is presented in Fig. 7-21.

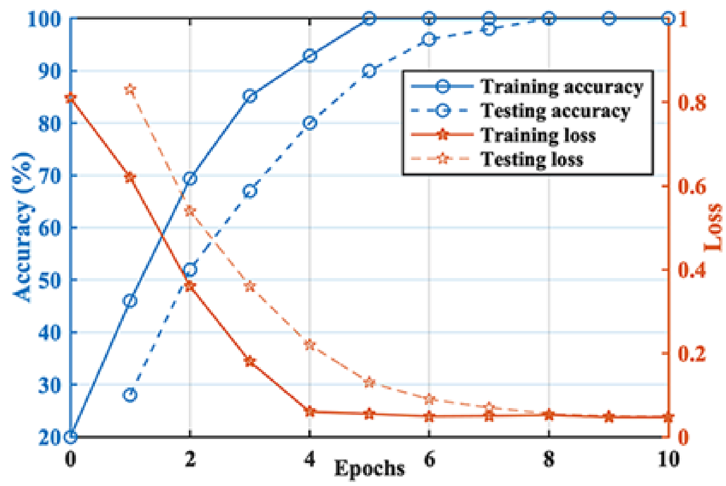

Fig. 7-21 Training and testing process of 1D-MACNN

Several estimating factors including accuracy, positive predictive value (Precision), true positive rate (Recall), false positive rate (FPR), and F1-score are used in this subchapter. Accuracy can be obtained as the ratio of number of correct predictions to the total number of testing samples, and other factors' definitions are given as

$$\begin{aligned} \text{Precision} &= \frac{1}{k}\sum_{i=1}^{k}\frac{TP_i}{TP_i+FP_i} \\ \text{Recall} &= \frac{1}{k}\sum_{i=1}^{k}\frac{TP_i}{TP_i+FN_i} \\ \text{FPR} &= \frac{1}{k}\sum_{i=1}^{k}\frac{FP_i}{TN_i+FP_i} \\ \text{F1-score} &= \frac{2*\text{Precision}*\text{Recall}}{\text{Precision}+\text{Recall}} \end{aligned}, \tag{7-27}$$

where k is the total number of classes (here $k=5$), TP is True Positive, which means both true label and correctly predicted label are "positive", FP is False Positive, which means true label is "negative", while incorrectly predicted label are "positive", TN is True Negative, which means both true label and correctly predicted label are "negative", FN is False Negative, which means true label is “positive”, while incorrectly predicted label are “negative”.

The comparison results among the proposed method and several previous investigations are given in Table 7-8, which shows that the proposed 1D-MACNN achieves the best performance, demonstrating the effectiveness of the 1D-MACNN.

Table 7-8 Comparison of classification performance among different methods

Method	[296]	[295]	[297]	1D-MACNN
Accuracy	0.88	0.62	0.77	**1**
Precision	0.88	0.63	0.77	**1**
Recall	0.88	0.62	0.77	**1**
FPR	0.03	0.09	0.06	**0**
F1-score	0.88	0.62	0.77	**1**

CHAPTER 8. CONCLUSIONS AND FUTURE WORK

This dissertation presents several investigations on bolt looseness detection via structural health monitoring (SHM) methods and the percussion-based approach. After a detailed literature review, three widely used SHM methods including the active sensing method, electromechanical impedance (EMI) method, and vibro-acoustic modulation (VAM) method are selected. In terms of these three methods, several new concepts were proposed to improve their performance.

For the active sensing method, three new models (numerical modeling, semi-analytical modeling, and analytical modeling) were developed to enable us to have a better understanding of working mechanism, based on the fractal contact theory. Then, considering the deficiencies of current damage index (DI) of the active sensing (i.e., the signal energy/amplitude), the author proposed several entropy-based DIs to improve the performance of the active sensing method, particularly for the detection of bolt early loosening and multi-bolt looseness. Several experiments were conducted to verify the effectiveness of these models and the proposed entropy-enhanced active sensing method.

Regarding the EMI method, the author developed an analytical modeling based on the fractal contact theory. By equivalenting the bolt joint to a mass-spring-damper system, the proposed analytical model describes the relationship between bolt preload and impedance signal (both real part and imaginary part). An experiment was conducted to verify this model.

Subsequently, the author proposed a new entropy-enhanced VAM method to solve several deficiencies of the current VAM method. For instance, current VAM method only employs single frequency signal as input (both high-frequency input and low-frequency input), which may be improper for industrial applications. Therefore, in the proposed entropy-enhanced VAM method, swept sine waves are used to replace the single-frequency input. Moreover, due to the swept sine waves, an entropy-based DI is developed to indicate the bolt early looseness. Then, with the help of the machine learning (ML) technique, the multi-bolt looseness detection via the VAM-based method was developed. Corresponding experiments were implemented to confirm the efficacy.

Then, the author proposed a new percussion-based approach, which required no constant contact between transducers and bolted connection. In other words, compared to the active sensing method, EMI method, and VAM method, the percussion-based approach has better potential for future industrial applications. An analytical model was developed to introduce the mechanism of the percussion-based approach. Then, with the help of the audio signal recognition (ASR) technology and deep learning (DL) technique, the author proposed two practical robotic-assisted percussion-based approaches and conducted a lab-level experiment to verify the feasibility of the proposed approaches.

Finally, the author provides a comparison among the above four methods (active sensing, EMI method, VAM method, and percussion-based approach) for bolt looseness detection, as given in Table 8-1, which reveals that these four methods have different advantages and disadvantages, thus leading to different potential for different industrial applications. For instance, the active sensing, EMI method, and VAM method are suitable for real-time monitoring of bolt looseness, while the percussion-based approach can give a fast estimation of bolted integrity. Compared to the active sensing, the VAM method is more sensitive to bolt looseness, but it requires two inputs, which can cause more complexity of the implementation. The EMI method has the best sensitivity among these four methods; however, ambient temperature has significant influence on its detection performance. In other words, proper methods should be selected for different cases in real industrial applications.

Table 8-1 Comparison among different methods for bolt looseness detection

Method	Advantage	Disadvantage
Active sensing	Easy to implement Real-time monitoring	Low sensitivity
EMI	High sensitivity Real-time monitoring	Vulnerable to ambient temperature
VAM	High sensitivity Real-time monitoring	Complex to implement
Percussion approach	Easy to implement Low cost Fast estimation	Vulnerable to ambient noise

In future work, the author will research the feasibility of the active sensing method, EMI method, and VAM method for bolt looseness recognition in a multi-bolt connection. Moreover, the author will attempt to solve several issues of the percussion-based approach, including the denoising performance and the adaptability. Particularly, some deficiencies of investigations in this dissertation will be solved in future work as follows:

(1) More repetitions of experiments will be conducted to ensure the repeatability,

(2) The Aliasing effect will be taken into consideration and the anti-aliasing filter will be used,

(3) The effect of ambient temperature on performance of EMI for bolt looseness will be investigated, and the author will attempt to provide a solution (e.g., compensation algorithm),

(4) The influence of input amplitude on performance of the active sensing will be researched,

(5) The author will attempt to develop baseline-free strategies for the active sensing, EMI method, and VAM method,

(6) Finally, the real industrial application of the proposed methods (e.g., bolt looseness detection in steel high-rise building) will be investigated, particularly several important issues (e.g., self-powering and wireless network).

REFERENCES

[1] Sakai, T. (1978). “Investigations of Bolt Loosening Mechanisms: 1st Report, On the Bolts of Transversely Loaded Joints.” *Bulletin of JSME*, 21(159), 1385–1390.

[2] Sakai, T. (1978). “Investigations of Bolt Loosening Mechanisms: 2nd Report, On the Center Bolts of Twisted Joints.” *Bulletin of JSME*, 21(159), 1391–1394.

[3] Shull, P. J. (2002). <u>Nondestructive Evaluation: Theory, Techniques, and Applications (Mechanical Engineering) (1st ed.)</u>. CRC Press.

[4] Samuel, P. D., & Pines, D. J. (2005). “A review of vibration-based techniques for helicopter transmission diagnostics.” *Journal of Sound and Vibration*, 282(1-2), 475–508.

[5] Montgomery, D. C. (2012). <u>Statistical Quality Control (7th ed.)</u>. Wiley.

[6] Worden, K., & Dulieu-Barton, J. M. (2004). “An Overview of Intelligent Fault Detection in Systems and Structures.” *Structural Health Monitoring: An International Journal*, 3(1), 85–98.

[7] Farrar, C. R., & Lieven, N. A. J. (2007). “Damage prognosis: the future of structural health monitoring.” *Philosophical Transactions of the Royal Society A: Mathematical, Physical and Engineering Sciences*, 365, 623-632.

[8] Annamdas, V. G. M., & Soh, C. K. (2009). “Application of Electromechanical Impedance Technique for Engineering Structures: Review and Future Issues.” *Journal of Intelligent Material Systems and Structures*, 21(1), 41–59.

[9] Janapati, V., Kopsaftopoulos, F., Li, F., Lee, S. J., & Chang, F.-K. (2016). “Damage detection sensitivity characterization of acousto-ultrasound-based structural health

monitoring techniques." *Structural Health Monitoring: An International Journal*, 15(2), 143–161.

[10] Guo, H., Xiao, G., Mrad, N., & Yao, J. (2011). "Fiber Optic Sensors for Structural Health Monitoring of Air Platforms." *Sensors*, 11(4), 3687–3705.

[11] Farrar, C. R., Park, G., Allen, D. W., & Todd, M. D. (2006). "Sensor network paradigms for structural health monitoring." *Structural Control and Health Monitoring*, 13(1), 210–225.

[12] Nair, A., & Cai, C. (2010). "Acoustic emission monitoring of bridges: Review and case studies." *Engineering Structures*, 32(6), 1704–1714.

[13] Ihn, J.-B., & Chang, F.-K. (2008). "Pitch-catch Active Sensing Methods in Structural Health Monitoring for Aircraft Structures." *Structural Health Monitoring: An International Journal*, 7(1), 5–19.

[14] Nikravesh, S. M. Y., & Goudarzi, M. (2017). "A Review Paper on Looseness Detection Methods in Bolted Structures." *Latin American Journal of Solids and Structures*, 14(12), 2153–2176.

[15] Kim, N., & Hong, M. (2009). "Measurement of axial stress using mode-converted ultrasound." *NDT & E International*, 42(3), 164–169.

[16] Bickford, J. H. (2007). Introduction to the Design and Behavior of Bolted Joints, Fourth Edition. Amsterdam University Press.

[17] Bickford, J. (1995). An Introduction to the Design and Behavior of Bolted Joints (Mechanical Engineering, Volume 97) (3rd ed.). Marcel Dekker.

[18] Temitop, S.J. (2015). Condition monitoring of bolt joints (Ph.D. Thesis). The University of Sheffield.

[19] Liang, C., Sun, F., & Rogers, C. (1994). "Coupled Electro-Mechanical Analysis of Adaptive Material Systems — Determination of the Actuator Power Consumption and System Energy Transfer." *Journal of Intelligent Material Systems and Structures*, 5(1), 12–20.

[20] Zhou, S., Liang, C., & Rogers, C. (1995). "Integration and Design of Piezoceramic Elements in Intelligent Structures." *Journal of Intelligent Material Systems and Structures*, 6(6), 733–743.

[21] Bhalla, S., & Soh, C. K. (2004). "Structural Health Monitoring by Piezo-Impedance Transducers. I: Modeling." *Journal of Aerospace Engineering*, 17(4), 154–165.

[22] Annamdas, V. G. M., & Soh, C. K. (2007). "Three-Dimensional Electromechanical Impedance Model. I: Formulation of Directional Sum Impedance." *Journal of Aerospace Engineering*, 20(1), 53–62.

[23] Overly, T.G., Park, G. & Farrar, C.R. (2007) Compact Hardware Development for SHM and Sensor Diagnostics using Admittance Measurements. Proceedings of IMAC-XXV: A Conference & Exposition on Structural Dynamics, Orlando, FL, Feb. 19-22.

[24] Park, G., Cudney, H. H., & Inman, D. J. (2001). "Feasibility of using impedance-based damage assessment for pipeline structures." *Earthquake Engineering & Structural Dynamics*, 30(10), 1463–1474.

[25] An, Y.-K., & Sohn, H. (2012). "Integrated impedance and guided wave based damage detection." *Mechanical Systems and Signal Processing*, 28, 50–62.

[26] Wait, J. R., Park, G., & Farrar, C. R. (2005). “Integrated Structural Health Assessment Using Piezoelectric Active Sensors.” *Shock and Vibration*, 12(6), 389–405.

[27] Mascarenas, D. L., Park, G., Farinholt, K. M., Todd, M. D., & Farrar, C. R. (2009). “A low-power wireless sensing device for remote inspection of bolted joints.” *Proceedings of the Institution of Mechanical Engineers, Part G: Journal of Aerospace Engineering*, 223(5), 565–575.

[28] Huynh, T.-C., Lee, K.-S., & Kim, J.-T. (2015). “Local dynamic characteristics of PZT impedance interface on tendon anchorage under prestress force variation.” *Smart Structures and Systems*, 15(2), 375–393.

[29] Krishnamurthy, K., Lalande, F., & Rogers, C. A. (1996). Effects of temperature on the electrical impedance of piezoelectric sensors. Smart Structures and Materials 1996: Smart Structures and Integrated Systems.

[30] Pavelko, I., Pavelko, V., Kuznetsov, S., & Ozolinsh, I. (2014). “Bolt-joint structural health monitoring by the method of electromechanical impedance.” *Aircraft Engineering and Aerospace Technology*, 86(3), 207–214.

[31] Ritdumrongkul, S., Abe, M., Fujino, Y., & Miyashita, T. (2003). “Quantitative health monitoring of bolted joints using a piezoceramic actuator–sensor.” *Smart Materials and Structures*, 13(1), 20–29.

[32] Tanner, N., Wait, J., Farrar, C. & Sohn, H. (2003). “Structural health monitoring using modular wireless sensors.” *Journal of Intelligent materials systems and structures*, 14(4), 43-56.

[33] Milanese, A., Marzocca, P., Nichols, J., Seaver, M., & Trickey, S. (2008). "Modeling and Detection of Joint Loosening using Output-Only Broad-Band Vibration Data." *Structural Health Monitoring: An International Journal*, 7(4), 309–328.

[34] He, K., & Zhu, W. D. (2014). "Detecting Loosening of Bolted Connections in a Pipeline Using Changes in Natural Frequencies." *Journal of Vibration and Acoustics*, 136(3).

[35] Huda, F., Kajiwara, I., Hosoya, N., & Kawamura, S. (2013). "Bolt loosening analysis and diagnosis by non-contact laser excitation vibration tests." *Mechanical Systems and Signal Processing*, 40(2), 589–604.

[36] Sohn, H. (2004). A review of structural health monitoring literature: 1996-2001. Los Alamos, NM: Los Alamos National Laboratory.

[37] Amerini, F., Barbieri, E., Meo, M., & Polimeno, U. (2010). "Detecting loosening/tightening of clamped structures using nonlinear vibration techniques." *Smart Materials and Structures*, 19(8), 085013.

[38] Nichols, J. M., Trickey, S. T., Seaver, M., Motley, S. R., & Eisner, E. D. (2006). "Using Ambient Vibrations to Detect Loosening of a Composite-to-Metal Bolted Joint in the Presence of Strong Temperature Fluctuations." *Journal of Vibration and Acoustics*, 129(6), 710–717.

[39] Esmaeel, R. A., Briand, J., & Taheri, F. (2011). "Computational simulation and experimental verification of a new vibration-based structural health monitoring approach using piezoelectric sensors." *Structural Health Monitoring: An International Journal*, 11(2), 237–250.

[40] Razi, P., Esmaeel, R. A., & Taheri, F. (2013). "Improvement of a vibration-based damage detection approach for health monitoring of bolted flange joints in pipelines." *Structural Health Monitoring: An International Journal*, 12(3), 207–224.

[41] Caccese, V., Mewer, R., & Vel, S. S. (2004). "Detection of bolt load loss in hybrid composite/metal bolted connections." *Engineering Structures*, 26(7), 895–906.

[42] Ungar, E. (1973). "The status of engineering knowledge concerning the damping of built-up structures." *Journal of Sound and Vibration*, 26(1), 141–154.

[43] Adams, D. E., & Farrar, C. R. (2002). "Classifying Linear and Nonlinear Structural Damage Using Frequency Domain ARX Models." *Structural Health Monitoring: An International Journal*, 1(2), 185–201.

[44] Trendafilova, I., & Brussel, H. V. (2001). "Non-Linear Dynamics Tools For The Motion Analysis And Condition Monitoring Of Robot Joints." *Mechanical Systems and Signal Processing*, 15(6), 1141–1164.

[45] Tjahjowidodo, T., Al-Bender, F., & Brussel, H. V. (2007). "Experimental dynamic identification of backlash using skeleton methods." *Mechanical Systems and Signal Processing*, 21(2), 959–972.

[46] Wang, T., Song, G., Wang, Z., & Li, Y. (2013). "Proof-of-concept study of monitoring bolt connection status using a piezoelectric based active sensing method." *Smart Materials and Structures*, 22(8), 087001.

[47] Yang, J., & Chang, F.-K. (2006). "Detection of bolt loosening in C–C composite thermal protection panels: II. Experimental verification." *Smart Materials and Structures*, 15(2), 591–599.

[48] Doyle, D., Zagrai, A., Arritt, B., & Çakan, H. (2009). "Damage Detection in Bolted Space Structures." *Journal of Intelligent Material Systems and Structures*, 21(3), 251–264.

[49] Wolfenden, A., Johnson, G., Holt, A., & Cunningham, B. (1986). "An Ultrasonic Method for Determining Axial Stress in Bolts." *Journal of Testing and Evaluation*, 14(5), 253.

[50] Chaki, S., Corneloup, G., Lillamand, I., & Walaszek, H. (2006). "Nondestructive control of bolt tightening: absolute and differential evaluation." *Materials Evaluation*, 64(6), 629-633.

[51] Chaki, S., Corneloup, G., Lillamand, I., & Walaszek, H. (2006). "Combination of Longitudinal and Transverse Ultrasonic Waves for In Situ Control of the Tightening of Bolts." *Journal of Pressure Vessel Technology*, 129(3), 383–390.

[52] Horstman, R., Peters, K., Meltzer, R., Vieth, M. B., Heyman, J., & Chern, E. (1982). "Ultrasonic Measurement of Axial Stress." *Journal of Testing and Evaluation*, 10(5), 202.

[53] Nikitina, N., & Ostrovsky, L. (1998). "An ultrasonic method for measuring stresses in engineering materials." *Ultrasonics*, 35(8), 605–610.

[54] Jhang, K.-Y., Quan, H.-H., Ha, J., & Kim, N.-Y. (2006). "Estimation of clamping force in high-tension bolts through ultrasonic velocity measurement." *Ultrasonics*, 44, 1339-1342.

[55] Nguyen, K.-D., Park, J.-H., & Kim, J.-T. (2011). Imote2-based multi-channel wireless impedance sensor nodes for local SHM of structural connections. Sensors

and Smart Structures Technologies for Civil, Mechanical, and Aerospace Systems 2011.

[56] Jhang, K.-Y. (2000). “Applications of nonlinear ultrasonics to the NDE of material degradation.” *IEEE Transactions on Ultrasonics, Ferroelectrics and Frequency Control*, 47(3), 540–548.

[57] Barbieri, E., Meo, M., & Polimeno, U. (2009). “Nonlinear wave propagation in damaged hysteretic materials using a frequency domain-based PM space formulation.” *International Journal of Solids and Structures*, 46(1), 165–180.

[58] Zhang, Z., Liu, M., Su, Z. & Xiao, Y. (2016). Evaluation of Bolt Loosening Using A Hybrid Approach Based on Contact Acoustic Nonlinearity. In proceedings of 19th World Conference on Non-Destructive Testing 2016, 1-8.

[59] Kim, J.-Y., Jacobs, L. J., Qu, J., & Littles, J. W. (2006). “Experimental characterization of fatigue damage in a nickel-base superalloy using nonlinear ultrasonic waves.” *The Journal of the Acoustical Society of America*, 120(3), 1266–1273.

[60] Cantrell, J. H., & Yost, W. T. (2001). “Nonlinear ultrasonic characterization of fatigue microstructures.” *International Journal of Fatigue*, 23, 487–490.

[61] Amerini, F., & Meo, M. (2011). “Structural health monitoring of bolted joints using linear and nonlinear acoustic/ultrasound methods.” *Structural Health Monitoring: An International Journal*, 10(6), 659–672.

[62] Vary, A., & Bowles, K. J. (1979). “An ultrasonic-acoustic technique for nondestructive evaluation of fiber composite quality.” *Polymer Engineering and Science*, 19(5), 373–376.

[63] Kong, X., & Li, J. (2018). An image-based feature tracking approach for bolt loosening detection in steel connections. Sensors and Smart Structures Technologies for Civil, Mechanical, and Aerospace Systems 2018.

[64] Wu, J., Cui, X., & Xu, Y. (2016). “A Novel RFID-Based Sensing Method for Low-Cost Bolt Loosening Monitoring.” *Sensors*, 16(2), 168.

[65] Yang, J., & Chang, F.-K. (2006). “Detection of bolt loosening in C–C composite thermal protection panels: I. Diagnostic principle.” *Smart Materials and Structures*, 15(2), 581–590.

[66] Esteban, J., & Rogers, C. A. (2000). “Energy dissipation through joints: theory and experiments.” *Computers & Structures*, 75(4), 347–359.

[67] Greenwood, J.A., & Williamson, J.B.P. (1966). “Contact of nominally flat surfaces.” *Proceedings of the Royal Society A-Mathematical, Physical and Engineering Sciences*, 295(1442), 300-319.

[68] Whitehouse, D.J., & Archard, J.F. (1970). “The properties of random surfaces of significance in their contact.” *Proceedings of the Royal Society of London. A. Mathematical and Physical Sciences*, 316(1524), 97–121.

[69] Chang, W.R., Etsion, I., & Bogy, D.B. (1987). “An Elastic-Plastic Model for the Contact of Rough Surfaces.” *Journal of Tribology*, 109(2), 257-263.

[70] Zhao, Y., Maietta, D. M., & Chang, L. (1999). “An Asperity Microcontact Model Incorporating the Transition From Elastic Deformation to Fully Plastic Flow.” *Journal of Tribology*, 122(1), 86–93.

[71] Evseev, D., Medvedev, B., & Grigoriyan, G. (1991). “Modification of the elastic-plastic model for the contact of rough surfaces.” *Wear*, 150(1-2), 79–88.

[72] Chang, W.-R. (1997). "An elastic-plastic contact model for a rough surface with an ion-plated soft metallic coating." *Wear*, 212(2), 229–237.

[73] Jeng, Y.-R., & Wang, P.-Y. (2003). "An Elliptical Microcontact Model Considering Elastic, Elastoplastic, and Plastic Deformation." *Journal of Tribology*, 125(2), 232–240.

[74] Jeng, Y.-R., & Peng, S.-R. (2005). "Elastic-Plastic Contact Behavior Considering Asperity Interactions for Surfaces With Various Height Distributions." *Journal of Tribology*, 128(2), 245–251.

[75] Kucharski, S., Klimczak, T., Polijaniuk, A., & Kaczmarek, J. (1994). "Finite-elements model for the contact of rough surfaces." *Wear*, 177(1), 1–13.

[76] Liu, G., Zhu, J., Yu, L., & Wang, Q. J. (2001). "Elasto-Plastic Contact of Rough Surfaces." *Tribology Transactions*, 44(3), 437–443.

[77] Kogut, L., & Etsion, I. (2003). "Adhesion in elastic–plastic spherical microcontact." *Journal of Colloid and Interface Science*, 261(2), 372–378.

[78] Kogut, L., & Etsion, I. (2002). "Elastic-Plastic Contact Analysis of a Sphere and a Rigid Flat." *Journal of Applied Mechanics*, 69(5), 657–662.

[79] Sahoo, P., & Ali, S. M. (2008). "Elastic-plastic adhesive contact of non-Gaussian rough surfaces." *Sadhana*, 33(4), 367–384.

[80] Mandelbrot, B. (1967). "How Long Is the Coast of Britain? Statistical Self-Similarity and Fractional Dimension." *Science*, 156(3775), 636–638.

[81] Majumdar, A., & Bhushan, B. (1990). "Role of Fractal Geometry in Roughness Characterization and Contact Mechanics of Surfaces." *Journal of Tribology*, 112(2), 205–216.

[82] Majumdar, A., & Bhushan, B. (1991). “Fractal Model of Elastic-Plastic Contact Between Rough Surfaces.” *Journal of Tribology*, 113(1), 1–11.

[83] Majumdar, A., & Tien, C. (1990). “Fractal characterization and simulation of rough surfaces.” *Wear*, 136(2), 313–327.

[84] Ganti, S., & Bhushan, B. (1995). “Generalised fractal analysis and its application to engineering surfaces.” *Wear*, 180(1-2), 17–34.

[85] Wang, S., & Komvopoulos, K. (1994). “A Fractal Theory of the Interfacial Temperature Distribution in the Slow Sliding Regime: Part I—Elastic Contact and Heat Transfer Analysis.” *Journal of Tribology*, 116(4), 812–822.

[86] Wang, S., & Komvopoulos, K. (1994). “A Fractal Theory of the Interfacial Temperature Distribution in the Slow Sliding Regime: Part II—Multiple Domains, Elastoplastic Contacts and Applications.” *Journal of Tribology*, 116(4), 824–832.

[87] Jackson, R. L. (2010). “An Analytical Solution to an Archard-Type Fractal Rough Surface Contact Model.” *Tribology Transactions*, 53(4), 543–553.

[88] Yin, X., & Komvopoulos, K. (2010). “An adhesive wear model of fractal surfaces in normal contact.” *International Journal of Solids and Structures*, 47(7-8), 912–921.

[89] Zou, M., Yu, B., Cai, J., & Xu, P. (2008). “Fractal Model for Thermal Contact Conductance.” *Journal of Heat Transfer*, 130(10), 101301.

[90] Morag, Y., & Etsion, I. (2007). “Resolving the contradiction of asperities plastic to elastic mode transition in current contact models of fractal rough surfaces.” *Wear*, 262(5-6), 624–629.

[91] Komvopoulos, K., & Gong, Z.-Q. (2007). “Stress analysis of a layered elastic solid in contact with a rough surface exhibiting fractal behavior.” *International Journal of Solids and Structures*, 44(7-8), 2109–2129.

[92] Kogut, L., & Jackson, R. L. (2005). “A Comparison of Contact Modeling Utilizing Statistical and Fractal Approaches.” *Journal of Tribology*, 128(1), 213–217.

[93] Sahoo, P., & Chowdhury, S. K. R. (2000). “A fractal analysis of adhesive friction between rough solids in gentle sliding.” *Proceedings of the Institution of Mechanical Engineers, Part J: Journal of Engineering Tribology*, 214(6), 583–595.

[94] Sahoo, P., & Chowdhury, S. R. (2002). “A fractal analysis of adhesive wear at the contact between rough solids.” *Wear*, 253(9-10), 924–934.

[95] Buzio, R., Boragno, C., & Valbusa, U. (2003). “Contact mechanics and friction of fractal surfaces probed by atomic force microscopy.” *Wear*, 254(9), 917–923.

[96] Komvopoulos, K., & Yan, W. (1997). “A Fractal Analysis of Stiction in Microelectromechanical Systems.” *Journal of Tribology*, 119(3), 391-400.

[97] Yan, W., & Komvopoulos, K. (1998). “Contact analysis of elastic-plastic fractal surfaces.” *Journal of Applied Physics*, 84(7), 3617-3624.

[98] Li, N., Wang, F., & Song, G. (2020). “Monitoring of bolt looseness using piezoelectric transducers: Three-dimensional numerical modeling with experimental verification.” *Journal of Intelligent Material Systems and Structures*, 31(6), 911-918.

[99] Parvasi, S. M., Ho, S. C., Kong, Q., Mousavi, R., & Song, G. (2016). “Real time bolt preload monitoring using piezoceramic transducers and time reversal

technique—a numerical study with experimental verification.” *Smart Materials and Structures*, 25(8), 085015.

[100] Pullen, J. & Williamson, J.B.P. (1972). “On the plastic contact of rough surfaces.” *Proceedings of the Royal Society of London. A. Mathematical and Physical Sciences*, 327(1569), 159-173.

[101] Johnson, K. L. (2008). <u>Contact Mechanics (Reprint ed.)</u>. Cambridge University Press.

[102] Huo, L., Wang, F., Li, H., & Song, G. (2017). “A fractal contact theory based model for bolted connection looseness monitoring using piezoceramic transducers.” *Smart Materials and Structures*, 26(10), 104010.

[103] Fink, M. (1999). “Time-Reversed Acoustics.” *Scientific American*, 281(5), 91-97.

[104] Fink, M., Montaldo, G., & Tanter, M. (2003). “Time-Reversal Acoustics in Biomedical Engineering.” *Annual Review of Biomedical Engineering*, 5(1), 465-497.

[105] Wang, F., Huo, L., & Song, G. (2017). “A piezoelectric active sensing method for quantitative monitoring of bolt loosening using energy dissipation caused by tangential damping based on the fractal contact theory.” *Smart Materials and Structures*, 27(1), 015023.

[106] Roundy, S., & Wright, P. K. (2004). “A piezoelectric vibration based generator for wireless electronics.” *Smart Materials and Structures*, 13(5), 1131-1142.

[107] Jiang, S., Zheng, Y., & Zhu, H. (2009). “A Contact Stiffness Model of Machined Plane Joint Based on Fractal Theory.” *Journal of Tribology*, 132(1).

[108] Britton, R. D., Elcoate, C. D., Alanou, M. P., Evans, H. P., & Snidle, R. W. (1999). “Effect of Surface Finish on Gear Tooth Friction.” *Journal of Tribology*, 122(1), 354-360.

[109] Xiao, L., Rosen, B., Amini, N., & Nilsson, P. H. (2003). “A study on the effect of surface topography on rough friction in roller contact.” *Wear*, 254(11), 1162-1169.

[110] Lin, T.-K., & Liang, J.-C. (2015). “Application of multi-scale (cross-) sample entropy for structural health monitoring.” *Smart Materials and Structures*, 24(8), 085003.

[111] Rojas, E., Baltazar, A., & Loh, K. J. (2015). “Damage detection using the signal entropy of an ultrasonic sensor network.” *Smart Materials and Structures*, 24(7), 075008.

[112] Wimarshana, B., Wu, N., & Wu, C. (2017). “Crack identification with parametric optimization of entropy & wavelet transformation.” *Structural Monitoring and Maintenance*, 4(1), 33–52.

[113] Zhang, X., Yan, Q., Yang, J., Zhao, J., & Shen, Y. (2019). “An assembly tightness detection method for bolt-jointed rotor with wavelet energy entropy.” *Measurement*, 136, 212–224.

[114] Lee, S. G., Yun, G. J., & Shang, S. (2014). “Reference-free damage detection for truss bridge structures by continuous relative wavelet entropy method.” *Structural Health Monitoring: An International Journal*, 13(3), 307–320.

[115] Shannon, C. E. (1948). “A mathematical theory of communication.” *Bell System Technical Journal*, 27(3), 379-423.

[116] Grassberger, P., & Procaccia, I. (1983). "Estimation of the Kolmogorov entropy from a chaotic signal." *Physical Review A*, 28(4), 2591–2593.

[117] Eckmann, J.-P., & Ruelle, D. (1985). "Ergodic theory of chaos and strange attractors." *The Theory of Chaotic Attractors*, 273–312.

[118] Baumert, M., Baier, V., Haueisen, J., Wessel, N., Meyerfeldt, U., Schirdewan, A., & Voss, A. (2004). "Forecasting of Life Threatening Arrhythmias Using the Compression Entropy of Heart Rate." *Methods of Information in Medicine*, 43(02), 202–206.

[119] Pincus, S. M. (1991). "Approximate entropy as a measure of system complexity." *Proceedings of the National Academy of Sciences*, 88(6), 2297–2301.

[120] Richman, J. S., & Moorman, J. R. (2000). "Physiological time-series analysis using approximate entropy and sample entropy." *American Journal of Physiology-Heart and Circulatory Physiology*, 278(6), H2039-H2049.

[121] Bandt, C., & Pompe, B. (2002). "Permutation Entropy: A Natural Complexity Measure for Time Series." *Physical Review Letters*, 88(17), 174102.

[122] Chen, W., Wang, Z., Xie, H., & Yu, W. (2007). "Characterization of Surface EMG Signal Based on Fuzzy Entropy." *IEEE Transactions on Neural Systems and Rehabilitation Engineering*, 15(2), 266–272.

[123] Nichols, J. M., Seaver, M., Trickey, S. T., Todd, M. D., Olson, C., & Overbey, L. (2005). "Detecting nonlinearity in structural systems using the transfer entropy." *Physical Review E*, 72(4), 046217.

[124] Nichols, J., Seaver, M., & Trickey, S. (2006). "A method for detecting damage-induced nonlinearities in structures using information theory." *Journal of Sound and Vibration*, 297(1-2), 1–16.

[125] Overbey, L., & Todd, M. (2009). "Effects of noise on transfer entropy estimation for damage detection." *Mechanical Systems and Signal Processing*, 23(7), 2178–2191.

[126] Nichols, J., Bucholtz, F., & Michalowicz, J. (2013). "Linearized Transfer Entropy for Continuous Second Order Systems." *Entropy*, 15(12), 3186–3204.

[127] Overbey, L., & Todd, M. (2009). "Dynamic system change detection using a modification of the transfer entropy." *Journal of Sound and Vibration*, 322(1-2), 438–453.

[128] Wu, S.-D., Wu, P.-H., Wu, C.-W., Ding, J.-J., & Wang, C.-C. (2012). "Bearing Fault Diagnosis Based on Multiscale Permutation Entropy and Support Vector Machine." *Entropy*, 14(8), 1343–1356.

[129] Costa, M., Goldberger, A. L., & Peng, C.-K. (2002). "Multiscale Entropy Analysis of Complex Physiologic Time Series." *Physical Review Letters*, 89(6), 0621021.

[130] Wu, S.-D., Wu, C.-W., Lin, S.-G., Wang, C.-C., & Lee, K.-Y. (2013). "Time Series Analysis Using Composite Multiscale Entropy." *Entropy*, 15(3), 1069–1084.

[131] Wu, S.-D., Wu, C.-W., Lin, S.-G., Lee, K.-Y., & Peng, C.-K. (2014). "Analysis of complex time series using refined composite multiscale entropy." *Physics Letters A*, 378(20), 1369–1374.

[132] Chang, Y.-C., Wu, H.-T., Chen, H.-R., Liu, A.-B., Yeh, J.-J., Lo, M.-T., Sun, C.-K. (2014). “Application of a Modified Entropy Computational Method in Assessing the Complexity of Pulse Wave Velocity Signals in Healthy and Diabetic Subjects.” *Entropy*, 16(7), 4032–4043.

[133] Wu, S.-D., Wu, C.-W., Lee, K.-Y., & Lin, S.-G. (2013). “Modified multiscale entropy for short-term time series analysis.” *Physica A: Statistical Mechanics and Its Applications*, 392(23), 5865–5873.

[134] Valencia, J. F., Porta, A., Vallverdu, M., Claria, F., Baranowski, R., Orlowska-Baranowska, E., & Caminal, P. (2009). “Refined Multiscale Entropy: Application to 24-h Holter Recordings of Heart Period Variability in Healthy and Aortic Stenosis Subjects.” *IEEE Transactions on Biomedical Engineering*, 56(9), 2202–2213.

[135] Costa, M., & Goldberger, A. (2015). “Generalized Multiscale Entropy Analysis: Application to Quantifying the Complex Volatility of Human Heartbeat Time Series.” *Entropy*, 17(3), 1197–1203.

[136] Amoud, H., Snoussi, H., Hewson, D., Doussot, M., & Duchene, J. (2007). “Intrinsic Mode Entropy for Nonlinear Discriminant Analysis.” *IEEE Signal Processing Letters*, 14(5), 297–300.

[137] Hu, M., & Liang, H. (2012). “Adaptive Multiscale Entropy Analysis of Multivariate Neural Data.” *IEEE Transactions on Biomedical Engineering*, 59(1), 12–15.

[138] Lo, M.-T., Chang, Y.-C., Lin, C., Young, H.-W. V., Lin, Y.-H., Ho, Y.-L., Hu, K. (2015). “Outlier-resilient complexity analysis of heartbeat dynamics.” *Scientific Reports*, 5(1), 8836.

[139] Humeau-Heurtier, A., Baumert, M., Mahé, G., & Abraham, P. (2014). “Multiscale Compression Entropy of Microvascular Blood FlowSignals: Comparison of Results from Laser Speckle Contrastand Laser Doppler Flowmetry Data in Healthy Subjects.” *Entropy*, 16(11), 5777–5795.

[140] Zhang, L., Xiong, G., Liu, H., Zou, H., & Guo, W. (2010). “Applying improved multi-scale entropy and support vector machines for bearing health condition identification.” *Proceedings of the Institution of Mechanical Engineers, Part C: Journal of Mechanical Engineering Science*, 224(6), 1315–1325.

[141] Costa, M., Goldberger, A. L., & Peng, C.-K. (2005). “Multiscale entropy analysis of biological signals.” *Physical Review E*, 71(2), 021906.

[142] Liu, Q., Chen, Y.-F., Fan, S.-Z., Abbod, M. F., & Shieh, J.-S. (2016). “EEG artifacts reduction by multivariate empirical mode decomposition and multiscale entropy for monitoring depth of anesthesia during surgery.” *Medical & Biological Engineering & Computing*, 55(8), 1435–1450.

[143] Shi, W., Shang, P., Ma, Y., Sun, S., & Yeh, C.-H. (2017). “A comparison study on stages of sleep: Quantifying multiscale complexity using higher moments on coarse-graining.” *Communications in Nonlinear Science and Numerical Simulation*, 44, 292–303.

[144] Humeau-Heurtier, A., Wu, C.-W., Wu, S.-D., Mahe, G., & Abraham, P. (2016). “Refined Multiscale Hilbert–Huang Spectral Entropy and Its Application to Central

and Peripheral Cardiovascular Data.” *IEEE Transactions on Biomedical Engineering*, 63(11), 2405–2415.

[145] Silva, L. E. V., Lataro, R. M., Castania, J. A., Silva, C. A. A. D., Valencia, J. F., Murta, L. O., Salgado, H. C., Fazan R., Porta, A. (2016). “Multiscale entropy analysis of heart rate variability in heart failure, hypertensive, and sinoaortic-denervated rats: classical and refined approaches.” *American Journal of Physiology-Regulatory, Integrative and Comparative Physiology*, 311(1), R150-R156.

[146] Liu, T., Yao, W., Wu, M., Shi, Z., Wang, J., & Ning, X. (2017). “Multiscale permutation entropy analysis of electrocardiogram.” *Physica A*, 471, 492–498.

[147] Grandy, T. H., Garrett, D. D., Schmiedek, F., & Werkle-Bergner, M. (2016). “On the estimation of brain signal entropy from sparse neuroimaging data.” *Scientific Reports*, 6(1), 23073.

[148] Kuo, P.-C., Chen, Y.-T., Chen, Y.-S., & Chen, L.-F. (2017). “Decoding the perception of endogenous pain from resting-state MEG.” *NeuroImage*, 144, 1–11.

[149] Costa, M., Peng, C.-K., Goldberger, A. L., & Hausdorff, J. M. (2003). “Multiscale entropy analysis of human gait dynamics.” *Physica A: Statistical Mechanics and Its Applications*, 330(1-2), 53–60.

[150] Rizal, A., Hidayat, R., & Nugroho, H. A. (2016). Multiscale Hjorth descriptor for lung sound classification. International Conference on Science and Technology, 160008–1.

[151] Aouabdi, S., Taibi, M., Bouras, S., & Boutasseta, N. (2017). “Using multi-scale entropy and principal component analysis to monitor gears degradation via the

motor current signature analysis." *Mechanical Systems and Signal Processing*, 90, 298–316.

[152] Xia, J., Shang, P., Wang, J., & Shi, W. (2014). "Classifying of financial time series based on multiscale entropy and multiscale time irreversibility." *Physica A: Statistical Mechanics and Its Applications*, 400, 151–158.

[153] Xu, K., & Wang, J. (2016). "Nonlinear multiscale coupling analysis of financial time series based on composite complexity synchronization." *Nonlinear Dynamics*, 86(1), 441–458.

[154] Lu, Y., & Wang, J. (2016). "Nonlinear dynamical complexity of agent-based stochastic financial interacting epidemic system." *Nonlinear Dynamics*, 86(3), 1823–1840.

[155] Hemakom, A., Chanwimalueang, T., Carrion, A., Aufegger, L., Constantinides, A. G., & Mandic, D. P. (2016). "Financial Stress Through Complexity Science." *IEEE Journal of Selected Topics in Signal Processing*, 10(6), 1112–1126.

[156] Yin, J., Su, C., Zhang, Y., & Fan, X. (2018). "Complexity Analysis of Carbon Market Using the Modified Multi-Scale Entropy." *Entropy*, 20(6), 434.

[157] Wang, J., Shang, P., Zhao, X., & Xia, J. (2013). "Multiscale Entropy Analysis of Traffic Time Series." *International Journal of Modern Physics C*, 24(02), 1350006.

[158] Yin, Y., & Shang, P. (2016). "Multivariate multiscale sample entropy of traffic time series." *Nonlinear Dynamics*, 86(1), 479–488.

[159] Guzmán-Vargas, L., Ramírez-Rojas, A., & Angulo-Brown, F. (2008). “Multiscale entropy analysis of electroseismic time series.” *Natural Hazards and Earth System Sciences*, 8(4), 855–860.

[160] Zeng, M., Zhang, S., Wang, E., & Meng, Q. (2016). Multiscale entropy analysis of the 3D near-surface wind field. 2016 12th World Congress on Intelligent Control and Automation (WCICA), 2797-2801.

[161] Gopinath, S., & P.r., P. (2016). “Multiscale and cross entropy analysis of auroral and polar cap indices during geomagnetic storms.” *Advances in Space Research*, 57(1), 289–301.

[162] Tang, Y., Zhao, A., Ren, Y.-Y., Dou, F.-X., & Jin, N.-D. (2016). “Gas–liquid two-phase flow structure in the multi-scale weighted complexity entropy causality plane.” *Physica A: Statistical Mechanics and Its Applications*, 449, 324–335.

[163] Gao, Z.-K., Yang, Y.-X., Zhai, L.-S., Ding, M.-S., & Jin, N.-D. (2016). “Characterizing slug to churn flow transition by using multivariate pseudo Wigner distribution and multivariate multiscale entropy.” *Chemical Engineering Journal*, 291, 74–81.

[164] Wang, F., Ho, S. C. M., & Song, G. (2019). “Monitoring of early looseness of multi-bolt connection: a new entropy-based active sensing method without saturation.” *Smart Materials and Structures*, 28(10), 10LT01.

[165] Ritdumrongkul, S., & Fujino, Y. (2006). “Identification of the Location and Level of Damage in Multiple-Bolted-Joint Structures by PZT Actuator-Sensors.” *Journal of Structural Engineering*, 132(2), 304–311.

[166] Min, J., Park, S., Yun, C.-B., Lee, C.-G., & Lee, C. (2012). "Impedance-based structural health monitoring incorporating neural network technique for identification of damage type and severity." *Engineering Structures*, 39, 210–220.

[167] Zhang, Y., Zhang, X., Chen, J., & Yang, J. (2018). "Electro-Mechanical Impedance Based Position Identification of Bolt Loosening Using LibSVM." *Intelligent Automation and Soft Computing*, 24(1), 81–88.

[168] Nichols, J. M., Todd, M. D., & Wait, J. R. (2003). "Using state space predictive modeling with chaotic interrogation in detecting joint preload loss in a frame structure experiment." *Smart Materials and Structures*, 12(4), 580–601.

[169] He, K., & Zhu, W. D. (2011). "A vibration-based structural damage detection method and its applications to engineering structures." *International Journal of Smart and Nano Materials*, 2(3), 194–218.

[170] Liang, D., & Yuan, S.-F. (2015). "Decision Fusion System for Bolted Joint Monitoring." *Shock and Vibration*, 2015, 1–11.

[171] Fierro, G. P. M., & Meo, M. (2017). "Identification of the Location and Level of Loosening in a Multi-bolt Structure using Nonlinear Ultrasound." *Structural Health Monitoring*, 17, 1349-1364.

[172] Meyer, J. J., & Adams, D. E. (2019). "Using impact modulation to quantify nonlinearities associated with bolt loosening with applications to satellite structures." *Mechanical Systems and Signal Processing*, 116, 787–795.

[173] Ahmed, M., Chanwimalueang, T., Thayyil, S., & Mandic, D. (2016). "A Multivariate Multiscale Fuzzy Entropy Algorithm with Application to Uterine EMG Complexity Analysis." *Entropy*, 19(1), 2.

[174] Peng, H., Long, F., & Ding, C. (2005). "Feature selection based on mutual information criteria of max-dependency, max-relevance, and min-redundancy." *IEEE Transactions on Pattern Analysis and Machine Intelligence*, 27(8), 1226–1238.

[175] Zendehboudi, A. (2016). "Implementation of GA-LSSVM modelling approach for estimating the performance of solid desiccant wheels." *Energy Conversion and Management*, 127, 245–255.

[176] Ahmed, M. U., & Mandic, D. P. (2011). "Multivariate multiscale entropy: A tool for complexity analysis of multichannel data." *Physical Review E*, 84(6), 061918.

[177] Iannarilli, F., & Rubin, P. (2003). "Feature selection for multiclass discrimination via mixed-integer linear programming." *IEEE Transactions on Pattern Analysis and Machine Intelligence*, 25(6), 779–783.

[178] Kwak, N., & Choi, C.-H. (2002). "Input feature selection by mutual information based on Parzen window." *IEEE Transactions on Pattern Analysis and Machine Intelligence*, 24(12), 1667–1671.

[179] Vapnik, V. N. (2000). "Direct Methods in Statistical Learning Theory." *The Nature of Statistical Learning Theory*, 225–265.

[180] Wang, F., Chen, Z., & Song, G. (2020). "Monitoring of multi-bolt connection looseness using entropy-based active sensing and genetic algorithm-based least square support vector machine." *Mechanical Systems and Signal Processing*, 136, 106507.

[181] Suykens, J. A. K., Gestel, T. van., Brabanter, J. de., Moor, B. D., & Vandewalle, J. (2002). Least squares support vector machines. World Scientific.

[182] Mohammadi, K., Shamshirband, S., Tong, C. W., Arif, M., Petković, D., & Ch, S. (2015). "A new hybrid support vector machine–wavelet transform approach for estimation of horizontal global solar radiation." *Energy Conversion and Management*, 92, 162–171.

[183] Holland, J. H. (1992). Adaptation in Natural and Artificial Systems: An Introductory Analysis with Applications to Biology, Control, and Artificial Intelligence (Reprint ed.). Bradford Books.

[184] Lu, X., Wang, F., Wang, X., & Si, L. (2018). "Modelling and optimisation of cutting parameters on surface roughness in micro-milling Inconel 718 using response surface methodology and genetic algorithm." *International Journal of Nanomanufacturing*, 14(1), 34-50.

[185] Mitchell, M. (1998). An Introduction to Genetic Algorithms (Complex Adaptive Systems) (Reprint ed.). MIT Press.

[186] Shukla, A., & Karki, H. (2016). "Application of robotics in offshore oil and gas industry— A review Part II." *Robotics and Autonomous Systems*, 75, 508-524.

[187] Mai, C., Pedersen, S., Hansen, L., Jepsen, K. L., & Yang, Z. (2016). Subsea infrastructure inspection: A review study. 2016 IEEE International Conference on Underwater System Technology: Theory and Applications (USYS), 71-76.

[188] Manley, J. E., Halpin, S., Radford, N., & Ondler, M. (2018). Aquanaut: A New Tool for Subsea Inspection and Intervention. OCEANS 2018 MTS/IEEE Charleston.

[189] Manjunatha, M., Selvakumar, A. A., Godeswar, V. P., & Manimaran, R. (2018). "A Low Cost Underwater Robot with Grippers for Visual Inspection of External Pipeline Surface." *Procedia Computer Science*, 133, 108-115.

[190] Aggarwal, A., Kampmann, P., Lemburg, J., & Kirchner, F. (2014). "Haptic Object Recognition in Underwater and Deep-sea Environments." *Journal of Field Robotics*, 32(1), 167-185.

[191] Omidvarnia, A., Mesbah, M., Pedersen, M., & Jackson, G. (2018). "Range Entropy: A Bridge between Signal Complexity and Self-Similarity." *Entropy*, 20(12), 962.

[192] Manis G., Aktaruzzaman, M., & Sassi, R. (2017) "Bubble Entropy: An Entropy Almost Free of Parameters." *IEEE Transactions on Biomedical Engineering*, 64(11), 2711-2718.

[193] Bearing Data Center: Seeded Fault Test Data, Case Western Reserve University, http://csegroups.case.edu/bearingdatacenter/pages/download-data-file.

[194] Zhang, C., & Ma, Y. (2014). Ensemble machine learning: Methods and applications. Springer.

[195] Cristianini, N., & Taylor, J. S. (2000). An introduction to support vector machines and other kernel-based learning methods. Cambridge University Press.

[196] Hosmer, D. W., Lemeshow, S., & Sturdivant, R. X. (2013). Applied logistic regression. Wiley.

[197] Hattori, K., & Takahashi, M. (1999). "A new nearest-neighbor rule in the pattern classification problem." *Pattern Recognition*, 32(3), 425-432.

[198] Maron, M. E. (1961). “Automatic Indexing: An Experimental Inquiry.” *Journal of the ACM*, 8(3), 404-417.

[199] Wang, Z., Lu, C., & Zhou, B. (2018). “Fault diagnosis for rotary machinery with selective ensemble neural networks.” *Mechanical Systems and Signal Processing*, 113, 112-130.

[200] Zhong, J. H., Wong, P. K., & Yang Z. X. (2018). “Fault diagnosis of rotating machinery based on multiple probabilistic classifiers.” *Mechanical Systems and Signal Processing*, 108, 99-114.

[201] Zheng, J., Pan, H., & Cheng, J. (2017). “Rolling bearing fault detection and diagnosis based on composite multiscale fuzzy entropy and ensemble support vector machines.” *Mechanical Systems and Signal Processing*, 85, 746-759.

[202] Lei, Y., Yang, B., Jiang, X., Jia, F., Li, N., & Nandi, A. K. (2020). “Applications of machine learning to machine fault diagnosis: A review and roadmap.” *Mechanical Systems and Signal Processing*, 138, 106587.

[203] Zhou, Z. (2012). Ensemble Methods: Foundations and Algorithms (Chapman & Hall/CRC Data Mining and Knowledge Discovery Serie) (1st ed.). Chapman and Hall/CRC.

[204] Breiman, L. (2001). “Random forests.” *Machine Learning*, 45 5-32.

[205] Aggarwal, C. C. (2014). Data Classification: Algorithms and Applications (Chapman & Hall/CRC Data Mining and Knowledge Discovery Series) (1st ed.). Chapman and Hall/CRC.

[206] Wong, Y., Du, H., & Pang, X. (2015). "Real-time electrical impedance resonance shift of piezoelectric sensor for detection of damage in honeycomb core sandwich structures." *NDT &E International*, 76, 61-65.

[207] Lim, Y. Y., Bhalla, S., & Soh, C. K. (2006). "Structural identification and damage diagnosis using self-sensing piezo-impedance transducers." *Smart Materials and Structures*, 15(4), 987-995.

[208] Peairs, D. M., Park, G., & Inman, D. J. (2004). "Improving Accessibility of the Impedance-Based Structural Health Monitoring Method." *Journal of Intelligent Material Systems and Structures*, 15(2), 129-139.

[209] Lim, Y. Y., & Soh, C. K. (2011). "Fatigue life estimation of a 1D aluminum beam under mode-I loading using the electromechanical impedance technique." *Smart Materials and Structures*, 20(12), 125001.

[210] Liang, Y., Li, D., Parvasi, S. M., & Song, G. (2016). "Load monitoring of pin-connected structures using piezoelectric impedance measurement." *Smart Materials and Structures*, 25(10), 105011.

[211] Liu, X., & Jiang, Z. (2009). "Design of a PZT patch for measuring longitudinal mode impedance in the assessment of truss structure damage." *Smart Materials and Structures*, 18(12), 125017.

[212] Soh, C. K., Tseng, K. K., Bhalla, S., & Gupta, A. (2000). "Performance of smart piezoceramic patches in health monitoring of a RC bridge." *Smart Materials and Structures*, 9(4), 533-542.

[213] Mascarenas, D. L., Todd, M. D., Park, G., & Farrar, C. R. (2007). "Development of an impedance-based wireless sensor node for structural health monitoring." *Smart Materials and Structures*, 16(6), 2137-2145.

[214] Park, S., Ahmad, S., Yun, C., & Roh, Y. (2006). "Multiple Crack Detection of Concrete Structures Using Impedance-based Structural Health Monitoring Techniques." *Experimental Mechanics*, 46(5), 609-618.

[215] Park, G., & Inman, D. J. (2005). "Impedance-Based Structural Health Monitoring." *Damage Prognosis*, 275-292.

[216] Liang, C., Sun, F. P., & Rogers, C. A. (1994). "An Impedance Method for Dynamic Analysis of Active Material Systems." *Journal of Vibration and Acoustics*, 116(1), 120-128.

[217] Liang, C., Sun, F., & Rogers, C. A. (1996). "Electro-mechanical impedance modeling of active material systems." *Smart Materials and Structures*, 5(2), 171-186.

[218] Giurgiutiu, V., & Zagrai, A. N. (2001). "Embedded Self-Sensing Piezoelectric Active Sensors for On-Line Structural Identification." *Journal of Vibration and Acoustics*, 124(1), 116-125.

[219] Zhou, S., Liang, C., & Rogers, C. A. (1996). "An Impedance-Based System Modeling Approach for Induced Strain Actuator-Driven Structures." *Journal of Vibration and Acoustics*, 118(3), 323-331.

[220] Yang, Y., Xu, J., & Soh, C. K. (2005). "Generic Impedance-Based Model for Structure-Piezoceramic Interacting System." *Journal of Aerospace Engineering*, 18(2), 93-101.

[221] Bhalla, S., & Soh, C. K. (2004). "Structural Health Monitoring by Piezo–Impedance Transducers. II: Applications." *Journal of Aerospace Engineering*, 17(4), 166-175.

[222] Annamdas, V. G., & Soh, C. K. (2008). "Three-Dimensional Electromechanical Impedance Model for Multiple Piezoceramic Transducers—Structure Interaction." *Journal of Aerospace Engineering*, 21(1), 35-44.

[223] Annamdas, V. G., & Soh, C. K. (2006). "Embedded piezoelectric ceramic transducers in sandwiched beams." *Smart Materials and Structures*, 15(2), 538-549.

[224] Yan, W., Lim, C. W., Cai, J. B., & Chen, W. Q. (2007). "An electromechanical impedance approach for quantitative damage detection in Timoshenko beams with piezoelectric patches." *Smart Materials and Structures*, 16(4), 1390-1400.

[225] Zagrai, A. N., & Giurgiutiu, V. (2001). "Electro-Mechanical Impedance Method for Crack Detection in Thin Plates." *Journal of Intelligent Material Systems and Structures*, 12(10), 709-718.

[226] Zhou, S., Liang, C., & Rogers, C. A. (1994). "Modeling of distributed piezoelectric actuators integrated with thin cylindrical shells." *The Journal of the Acoustical Society of America*, 96(3), 1605-1612.

[227] Yang, Y., & Hu, Y. (2007). "Electromechanical impedance modeling of PZT transducers for health monitoring of cylindrical shell structures." *Smart Materials and Structures*, 17(1), 015005.

[228] Jiang, S., Zheng, Y., & Zhu, H. (2009). "A Contact Stiffness Model of Machined Plane Joint Based on Fractal Theory." *Journal of Tribology*, 132(1), 011401.

[229] Zhao, Y., Maietta, D. M., & Chang, L. (1999). "An Asperity Microcontact Model Incorporating the Transition From Elastic Deformation to Fully Plastic Flow." *Journal of Tribology*, 122(1), 86-93.

[230] Sirohi, J., & Chopra, I. (2000). "Fundamental Understanding of Piezoelectric Strain Sensors." *Journal of Intelligent Material Systems and Structures*, 11(4), 246-257.

[231] Plunkett, R. (1958). Mechanical Impedance. Ft. Belvoir: Defense Technical Information Center.

[232] Tabor, D. (2007). The hardness of metals. Clarendon Press.

[233] Zhu, H., Ge, S., Huang, X., Zhang, D., & Liu, J. (2003). "Experimental study on the characterization of worn surface topography with characteristic roughness parameter." *Wear*, 255(1-6), 309-314.

[234] Sauerbrey, G. (1959). "Verwendung von Schwingquarzen zur Wagung dunner Schichten und zur Mikrowagung." *Zeitschrift Fur Physik*, 155(2), 206-222.

[235] Park, G., Sohn, H., Farrar, C. R., & Inman, D. J. (2003). "Overview of Piezoelectric Impedance-Based Health Monitoring and Path Forward." *The Shock and Vibration Digest*, 35(6), 451-463.

[236] Fu, W. P., Huang, Y. M., Zhang, X. L., & Guo, Q. (2000). "Experimental Investigation of Dynamic Normal Characteristics of Machined Joint Surfaces." *Journal of Vibration and Acoustics*, 122(4), 393-398.

[237] He, C., Yang, S., Liu, Z., & Wu, B. (2014). "Damage Localization and Quantification of Truss Structure Based on Electromechanical Impedance Technique and Neural Network." *Shock and Vibration*, 2014, 1-9.

[238] Park, S., Shin, H., & Yun, C. (2009). “Wireless impedance sensor nodes for functions of structural damage identification and sensor self-diagnosis.” *Smart Materials and Structures*, 18(5), 055001.

[239] Wang, F., Ho, S. C., Huo, L., & Song, G. (2018). “A Novel Fractal Contact-Electromechanical Impedance Model for Quantitative Monitoring of Bolted Joint Looseness.” *IEEE Access*, 6, 40212-40220.

[240] Deng, M., & Pei, J. (2007). “Assessment of accumulated fatigue damage in solid plates using nonlinear Lamb wave approach.” *Applied Physics Letters*, 90(12), 121902.

[241] Hu, H. F., Staszewski, W. J., Hu, N. Q., Jenal, R. B., & Qin, G. J. (2010). “Crack detection using nonlinear acoustics and piezoceramic transducers—instantaneous amplitude and frequency analysis.” *Smart Materials and Structures*, 19(6), 065017.

[242] Klepka, A., Pieczonka, L., Staszewski, W., & Aymerich, F. (2014). “Impact damage detection in laminated composites by non-linear vibro-acoustic wave modulations.” *Composites Part B: Engineering*, 65, 99-108.

[243] Ooijevaar, T., Rogge, M. D., Loendersloot, R., Warnet, L., Akkerman, R., & Tinga, T. (2016). “Vibro-acoustic modulation–based damage identification in a composite skin–stiffener structure.” *Structural Health Monitoring: An International Journal*, 15(4), 458-472.

[244] Zhang, Y., Tournat, V., Abraham, O., Durand, O., Letourneur, S., Duff, A. L., & Lascoup, B. (2013). “Nonlinear mixing of ultrasonic coda waves with lower frequency-swept pump waves for a global detection of defects in multiple scattering media.” *Journal of Applied Physics*, 113(6), 064905.

[245] Lim, H. J., Sohn, H., Desimio, M. P., & Brown, K. (2014). "Reference-free fatigue crack detection using nonlinear ultrasonic modulation under various temperature and loading conditions." *Mechanical Systems and Signal Processing*, 45(2), 468-478.

[246] Sohn, H., Lim, H. J., Desimio, M. P., Brown, K., & Derriso, M. (2014). "Nonlinear ultrasonic wave modulation for online fatigue crack detection." *Journal of Sound and Vibration*, 333(5), 1473-1484.

[247] Courtney, C. R., Drinkwater, B. W., Neild, S. A., & Wilcox, P. D. (2008). "Factors affecting the ultrasonic intermodulation crack detection technique using bispectral analysis." *NDT & E International*, 41(3), 223-234.

[248] Singh, A. K., Tan, V. B., Tay, T. E., & Lee, H. P. (2018). "Experimental Investigations Into Nonlinear Vibro-Acoustics for Detection of Delaminations in a Composite Laminate." *Journal of Nondestructive Evaluation, Diagnostics and Prognostics of Engineering Systems*, 2(1). 011002.

[249] Rehman, N. U., & Mandic, D. P. (2011). "Filter Bank Property of Multivariate Empirical Mode Decomposition." *IEEE Transactions on Signal Processing*, 59(5), 2421-2426.

[250] Looney, D., Hemakom, A., & Mandic, D. P. (2015). "Intrinsic multi-scale analysis: A multi-variate empirical mode decomposition framework." *Proceedings of the Royal Society A: Mathematical, Physical and Engineering Sciences*, 471(2173), 20140709.

[251] Ahmed, M. U., & Mandic, D. P. (2011). “Multivariate multiscale entropy: A tool for complexity analysis of multichannel data.” *Physical Review E*, 84(6), 061918.

[252] Yoder, N. C., & Adams, D. E. (2010). “Vibro-Acoustic Modulation Utilizing a Swept Probing Signal for Robust Crack Detection.” *Structural Health Monitoring: An International Journal*, 9(3), 257-267.

[253] Donskoy, D., Sutin, A., & Ekimov, A. (2001). “Nonlinear acoustic interaction on contact interfaces and its use for nondestructive testing.” *NDT & E International*, 34(4), 231-238.

[254] Dziedziech, K., Pieczonka, L., Adamczyk, M., Klepka, A., & Staszewski, W. J. (2017). “Efficient swept sine chirp excitation in the non-linear vibro-acoustic wave modulation technique used for damage detection.” *Structural Health Monitoring: An International Journal*, 17(3), 565-576.

[255] Rehman, N., & Mandic, D. P. (2009). “Multivariate empirical mode decomposition.” *Proceedings of the Royal Society A: Mathematical, Physical and Engineering Sciences*, 466(2117), 1291-1302.

[256] Huang, N. E., Shen, Z., Long, S. R., Wu, M. C., Shih, H. H., Zheng, Q., Yen, N. C., Tung, C.C. & Liu, H. H. (1998). “The empirical mode decomposition and the Hilbert spectrum for nonlinear and non-stationary time series analysis.” *Proceedings of the Royal Society of London. Series A: Mathematical, Physical and Engineering Sciences*, 454(1971), 903-995.

[257] Faure, H., & Pillichshammer, F. (2008). “Lp discrepancy of generalized two-dimensional Hammersley point sets.” *Monatshefte Für Mathematik*, 158(1), 31-61.

[258] Delechelle, E., Lemoine, J., & Niang, O. (2005). “Empirical mode decomposition: An analytical approach for sifting process.” *IEEE Signal Processing Letters*, 12(11), 764-767.

[259] Wang, F., & Song, G. (2019). “Bolt early looseness monitoring using modified vibro-acoustic modulation by time-reversal.” *Mechanical Systems and Signal Processing*, 130, 349-360.

[260] Zhang, Z., Xu, Y., Yang, J., Li, X., & Zhang, D. (2015). “A Survey of Sparse Representation: Algorithms and Applications.” *IEEE Access*, 3, 490-530.

[261] Wang, F., & Song, G. (2020). “Monitoring of multi-bolt connection looseness using a novel vibro-acoustic method.” *Nonlinear Dynamics*, 100(1), 243-254.

[262] Liaw, A., & Wiener, M. (2002) “Classification and regression by randomForest.” *R News*, 2, 18-22.

[263] Liang, Z., Wang, Y., Sun, X., Li, D., Voss, L. J., Sleigh, J. W., Hagihira, S., Li, X. (2015). “EEG entropy measures in anesthesia.” *Frontiers in Computational Neuroscience*, 9.

[264] Sahoo, S. K., & Makur, A. (2015). “Signal Recovery from Random Measurements via Extended Orthogonal Matching Pursuit.” *IEEE Transactions on Signal Processing*, 63(10), 2572-2581.

[265] Donoho, D. L., & Elad, M. (2003). “Optimally sparse representation in general (nonorthogonal) dictionaries via 1 minimization.” *Proceedings of the National Academy of Sciences*, 100(5), 2197-2202.

[266] Adams, R. D., Cawley, P., Pye, C. J., & Stone, B. J. (1978). “A Vibration Technique for Non-Destructively Assessing the Integrity of Structures.” *Journal of Mechanical Engineering Science*, 20(2), 93-100.

[267] Wu, H., & Siegel, M. (2000). “Correlation of accelerometer and microphone data in the "coin tap test".” *IEEE Transactions on Instrumentation and Measurement*, 49(3), 493-497.

[268] Baglio, S., & Savalli, N. (2006). ““Fuzzy Tap-Testing” Sensors for Material Health-State Characterization.” *IEEE Transactions on Instrumentation and Measurement*, 55(3), 761-770.

[269] Yella, S., Gupta, N. K., & Dougherty, M. S. (2007). “Comparison of pattern recognition techniques for the classification of impact acoustic emissions.” *Transportation Research Part C: Emerging Technologies*, 15(6), 345-360.

[270] Tong, F., Xu, X., Luk, B., & Liu, K. (2008). “Evaluation of tile–wall bonding integrity based on impact acoustics and support vector machine.” *Sensors and Actuators A: Physical*, 144(1), 97-104.

[271] Delgado-Arredondo, P. A., Morinigo-Sotelo, D., Osornio-Rios, R. A., Avina-Cervantes, J. G., Rostro-Gonzalez, H., & Romero-Troncoso, R. D. (2017). “Methodology for fault detection in induction motors via sound and vibration signals.” *Mechanical Systems and Signal Processing*, 83, 568-589.

[272] Glowacz, A. (2019). “Fault diagnosis of single-phase induction motor based on acoustic signals.” *Mechanical Systems and Signal Processing*, 117, 65-80.

[273] Li, C., Sanchez, R., Zurita, G., Cerrada, M., Cabrera, D., & Vásquez, R. E. (2016). “Gearbox fault diagnosis based on deep random forest fusion of acoustic and vibratory signals.” *Mechanical Systems and Signal Processing*, 76-77, 283-293.

[274] Dayong, N., Changle, S., Yongjun, G., Zengmeng, Z., & Jiaoyi, H. (2016). “Extraction of fault component from abnormal sound in diesel engines using acoustic signals.” *Mechanical Systems and Signal Processing*, 75, 544-555.

[275] Zhang, H., Lu, S., He, Q., & Kong, F. (2016). “Multi-bearing defect detection with trackside acoustic signal based on a pseudo time–frequency analysis and Dopplerlet filter.” *Mechanical Systems and Signal Processing*, 70-71, 176-200.

[276] Park, K., Motai, Y., & Yoon, J. R. (2017). “Acoustic Fault Detection Technique for High-Power Insulators.” *IEEE Transactions on Industrial Electronics*, 64(12), 9699-9708.

[277] Zuo, S., Lin, F., & Wu, X. (2015). “Noise Analysis, Calculation, and Reduction of External Rotor Permanent-Magnet Synchronous Motor.” *IEEE Transactions on Industrial Electronics*, 62(10), 6204-6212.

[278] Deng, W., & Zuo, S. (2018). “Axial Force and Vibroacoustic Analysis of External-Rotor Axial-Flux Motors.” *IEEE Transactions on Industrial Electronics*, 65(3), 2018-2030.

[279] Iwan, W. D. (1966). “A Distributed-Element Model for Hysteresis and Its Steady-State Dynamic Response.” *Journal of Applied Mechanics*, 33(4), 893-900.

[280] Tian, H., Li, B., Liu, H., Mao, K., Peng, F., & Huang, X. (2011). “A new method of virtual material hypothesis-based dynamic modeling on fixed joint interface in

machine tools." *International Journal of Machine Tools and Manufacture*, 51(3), 239-249.

[281] Srinivas, S., Rao, C. J., & Rao, A. (1970). "An exact analysis for vibration of simply-supported homogeneous and laminated thick rectangular plates." *Journal of Sound and Vibration*, 12(2), 187-199.

[282] Hu, Y., & Huang, S. (2000). "The frequency response and damping effect of three-layer thin shell with viscoelastic core." *Computers & Structures*, 76(5), 577-591.

[283] Reddy, J. N., & Robbins, D. H. (1994). "Theories and Computational Models for Composite Laminates." *Applied Mechanics Reviews*, 47(6), 147-169.

[284] Mitzner, K. M. (1967). "Numerical Solution for Transient Scattering from a Hard Surface of Arbitrary Shape—Retarded Potential Technique." *The Journal of the Acoustical Society of America*, 42(2), 391-397.

[285] Schenck, H. A. (1968). "Improved Integral Formulation for Acoustic Radiation Problems." *The Journal of the Acoustical Society of America*, 44(1), 41-58.

[286] Elliott, S. J., & Johnson, M. E. (1993). "Radiation modes and the active control of sound power." *The Journal of the Acoustical Society of America*, 94(4), 2194-2204.

[287] Berenger, J. (1994). "A perfectly matched layer for the absorption of electromagnetic waves." *Journal of Computational Physics*, 114(2), 185-200.

[288] Wang, F., Ho, S. C., & Song, G. (2019). "Modeling and analysis of an impact-acoustic method for bolt looseness identification." *Mechanical Systems and Signal Processing*, 133, 106249.

[289] Weilharter, B., Biro, O., Lang, H., Ofner, G., & Rainer, S. (2012). “Validation of a Comprehensive Analytic Noise Computation Method for Induction Machines.” *IEEE Transactions on Industrial Electronics*, 59(5), 2248-2257.

[290] Wang, F., Mobiny, A., Van Nguyen, H., & Song, G. (2020). “If structure can exclaim: a novel robotic-assisted percussion method for spatial bolt-ball joint looseness detection.” *Structural Health Monitoring: An International Journal*, 147592172092314.

[291] Yu, Y., Tang, S., Raposo, F., & Chen, L. (2019). “Deep Cross-Modal Correlation Learning for Audio and Lyrics in Music Retrieval.” *ACM Transactions on Multimedia Computing, Communications, and Applications*, 15(1), 1–16.

[292] Santoro, A., Bartunov, S., Botvinick, M., Wierstra, D., & Lillicrap, T. (2016). “Meta-Learning with Memory-Augmented Neural Networks.” http://proceedings.mlr.press/v48/santoro16.html。

[293] Liu, Z., Wu, Z., Li, T., Li, J., & Shen, C. (2018). “GMM and CNN Hybrid Method for Short Utterance Speaker Recognition.” *IEEE Transactions on Industrial Informatics*, 14(7), 3244–3252.

[294] Phan, H., Hertel, L., Maass, M., Koch, P., Mazur, R., & Mertins, A. (2017). “Improved Audio Scene Classification Based on Label-Tree Embeddings and Convolutional Neural Networks.” *IEEE/ACM Transactions on Audio, Speech, and Language Processing*, 25(6), 1278–1290.

[295] Kong, Q., Zhu, J., Ho, S. C. M., & Song, G. (2018). “Tapping and listening: a new approach to bolt looseness monitoring.” *Smart Materials and Structures*, 27(7), 07LT02.

[296] Zhang, Y., Zhao, X., Sun, X., Su, W., & Xue, Z. (2019). "Bolt loosening detection based on audio classification." *Advances in Structural Engineering*, 22(13), 2882–2891.

[297] Yuan, R., Lv, Y., Kong, Q., & Song, G. (2019). "Percussion-based bolt looseness monitoring using intrinsic multiscale entropy analysis and BP neural network." *Smart Materials and Structures*, 28(12), 125001.

[298] Wang, F., Song, G., & Mo, Y. (2020). "Shear loading detection of through bolts in bridge structures using a percussion-based one-dimensional memory-augmented convolutional neural network." *Computer-Aided Civil and Infrastructure Engineering*, (Online).